ENHANCING MAGNETOSOME BIOMANUFACTURING: UNDERSTANDING BIOMINERALIZATION AND PROCESS DEVELOPMENT

MARTA MASÓ MARTÍNEZ

Doctor of Philosophy

ASTON UNIVERSITY

September 2024

Aston University

Enhancing magnetosome biomanufacturing: understanding biomineralization and process development

Marta Masó Martínez

Doctor of Philosophy

September 2024

Thesis Abstract

Magnetosomes, membrane-bound magnetic nanocrystals produced by magnetotactic bacteria, offer a promising alternative to chemically synthesized magnetic nanoparticles due to their unique properties, enabling great potential in nanobiotechnology and biomedicine. However, several challenges hinder their large-scale production, including limited understanding of the biomineralization processes, cell physiology, batch-to-batch reproducibility, and lack of rapid and efficient characterization techniques. This thesis addresses these challenges by exploring ironuptake and its role in biomineralization, assessing the impact of oxidative stress on magnetosome formation, and evaluating cell disruption techniques on magnetosome chain integrity.

Correlative microscopy, combined with a range of analytical methods, was employed to elucidate magnetosome biomineralization and the associated physiological changes of *Magnetospirillum gryphiswaldense* MSR-1 under various stress conditions. The research revealed a direct correlation between the labile Fe^{2+} pool size and magnetosome content, as higher intracellular iron concentrations were associated with increased magnetosome production. An intracellular iron pool, distinct from magnetite, was identified, being present throughout all stages of biomineralization. The potential role of magnetosomes in mitigating oxidative stress is further evidenced as magnetosome-producing cells maintained high levels of intracellular iron with minimal oxidative stress, while non-producing cells exhibited reduced magnetosome and iron content alongside elevated reactive oxygen species levels.

The observed changes in MSR-1 cell morphology and viability under external stress conditions highlight the importance of monitoring physiological changes to enhance bioprocess efficiency and robustness, crucial for the production of high-quality magnetosomes. Furthermore, downstream processing technologies were shown to compromise magnetosome chain integrity, essential for certain applications. Among the tested disruption techniques, high-pressure homogenization was found to be the most effective in preserving magnetosome chain length, while nano-flow cytometry emerged as a promising technique for rapid quality assessment of single-magnetosome preparations. The findings contribute to a broader understanding of magnetosome production, emphasizing the importance of optimizing culture conditions and developing reliable characterization methods.

Keywords: magnetic nanoparticles, magnetotactic bacteria, magnetosomes, biomineralization, bioprocessing, correlative microscopy, oxidative stress, cell disruption, iron transport dynamics.

Als meus avis Fernando, Margarita i Rosa, i la meva família

Acknowledgments

I would like to begin by expressing my deepest gratitude to my supervisor, Dr. Alfred Fernandez-Castañé. Your trust, support, and guidance over these past four years have been invaluable to me. I am truly grateful for your encouragement throughout all the highs and lows of this project. Moltes gràcies per tot! I would also like to extend my gratitude to my associate supervisor, Professor Paul Topham, whose knowledge and experience have been very valuable and have provided a different perspective throughout this project.

During my PhD, I had the opportunity to use several external facilities, and I am deeply grateful to everyone who collaborated with me. First, I would like to acknowledge our collaborators from nanoFCM, especially Rebecca Lees and Dr. Ben Peacock, for their assistance with the nFCM experiments. Secondly, I would like to thank all the staff from ALBA and Diamond synchrotron facilities. While all the synchrotron experiments included in this thesis were conducted at Diamond, I also want to express my gratitude to Dr. Eva Pereiro and Dr. Lucia Aballe from the MISTRAL beamline at ALBA Synchrotron. Our first correlative microscopy experiments there, didn't yield the expected results, but they provided us with valuable preliminary insights that significantly contributed to the success of our subsequent experiments at Diamond. To everyone at beamline B24 at Diamond, especially to Dr. Maria Harkiolaki, Dr. Chidinma Okolo, and Dr. Archana Jadhav, thank you for all the support during our numerous beamtimes, and for experimenting with our samples so that we could use the iron edge even before it was officially commissioned. I would also like to give special mention to Georgia and Helena, who provided remote support during data collection at ALBA during COVID-19 times, and to my Bio Lab colleague, Josh, for his assistance with data acquisition at Diamond. I am also thankful to Dr. Julika Radecke from eBIC for her help with the cryoEM acquisition. Finally, I would like to acknowledge the funding provided by ALBA (proposals: 2020024149, PID 13843) and Diamond (proposals: BI26789, BI30471, BI33090, BI31371), which made our beamtime sessions possible and contributed to the success of this research.

Many thanks to all the staff at EBRI; it was great meeting you and sharing the past four years with you. A special mention is reserved to Dr. Jinesh Cherukkattu Manayil and Dr. Daniel Jozef Nowakowski for their training and assistance every time lab issues arose. Clara, también quiero darte las gracias por ofrecer siempre tu ayuda y apoyo, se te echa de menos por EBRI.

To all the past and present PhD students and PDRA in EBRI thank you so much for being part of my journey, without you it wouldn’t have been the same. We have shared a lot of hours in the office, labs,

kitchen, so thanks to all of you for making my stay here more enjoyable. I could mention a lot of people like Emad, Michael, Muhammad, Alberto, Zeinab, Maria, just to mention a few, but I wanted to especially mention Mpho and Jiaojiao for always being there and offering their support throughout all these years.

Thank you to all of the past and present members of the Bio Lab, from Benjamin, one of the first lab colleagues, to Longinus and Zeinab, the latest additions. To Cornelius that always broad so much joy to the lab. To Lewis that has always been so generous listening to all my complains and offering his help. To all the masters and undergraduate students, especially to Bakhtawar, Marcia, Ricarda and Emma, it was a pleasure to have you around the lab. Y finalmente quiero darle las gracias a Carmen, uno de mis primeros apoyos en Birmingham y la mejor compañera de lab! Sin ti, las noches de fermentation y todas las locuras del lab hubiesen sido más aburridas. Muchas gracias por tu constante apoyo dentro y fuera del lab!

To all my friends in Birmingham – Carmen, Lierni, Dani, Nelson, Victor, Sasi, Alberto – thank you so much for making this journey much more easier and for all your encouragement. A tots els meus amics i amigues de Barcelona, moltes gràcies per donar-me suport des de la distància i per fer-me sentir com si res no hagués canviat quan vinc a Barcelona.

I finalment, moltes gràcies a la meva família. Sense el vostre suport incondicional i confiança durant aquests quatre anys, no hauria estat possible arribar fins aquí.

List of publications

"Magnetotactic bacteria-based biorefinery: potential for generating multiple products from a single fermentation". C. Hierro-Iglesias, M. Masó-Martínez, J. Dulai, K.J. Chong, P. Blanco-Sanchez, A. Fernández-Castané. ACS Sustainable Chemistry & Engineering Vol 9, 2021. DOI: 10.1021/acssuschemeng.1c02435

"Magnetosomes: biological synthesis of magnetic nanostructures". M. Masó-Martínez, P. D. Topham, and A. Fernández-Castané, in Fundamentals of Low Dimensional Magnets, R. K. Gupta, S. R. Mishra, and T. A. Nguyen, Eds. CRC Press, 2022. DOI: 10.1201/9781003197492-16

"Evaluation of cell disruption technologies on magnetosome chain length and aggregation behaviour from *Magnetospirillum gryphiswaldense* MSR-1". M. Masó-Martínez, B. Fryer, D. Aubert, B. Peacock, R. Lees, G. A. Rance, M. W. Fay, P. D. Topham, A. Fernández-Castané. Front. Bioeng. Biotechnol., vol. 11, 2023. DOI: 10.3389/fbioe.2023.1172457

"An integrated approach to elucidate the interplay between iron uptake dynamics and magnetosome formation at the single-cell level in *Magnetospirillum gryphiswaldense*". M. Masó-Martínez, J. Bond, C. A. Okolo, A. C. Jadhav, M. Harkiolaki, P. D. Topham, A. Fernández-Castané. ACS Appl. Mater. Interfaces, vol. 16, 2024. DOI: 10.1021/acsami.4c15975

"Impact of oxidative stress on *Magnetospirillum gryphiswaldense* MSR-1 physiology and magnetosome biomineralization at the single-cell level". M. Masó-Martínez, J. Radecke, C. MacGregor-Chatwin, P. D. Topham, A. Fernández-Castané. Submitted to Materials Today Advances.

List of conference presentations

Poster Presentations:

"Evaluation of cell disruption technologies on magnetosome chain length and aggregation behaviour from *Magnetospirillum gryphiswaldense* MSR-1", 7th International Meeting on Magnetotactic Bacteria, 4 – 8 September 2022, Bayreuth (Germany).

Oral Presentations:

"Determination of the accumulation of intracellular reactive oxygen species in magnetotactic bacteria by flow cytometry", Midlands Innovation Flow Cytometry Meeting 2023, 26th April 2023, University of Nottingham (United Kingdom).

"The role of magnetosomes in the protection against accumulation of intracellular reactive oxygen species in magnetotactic bacteria", 6th meeting on Microbial Responses to Stress, 19 – 21 September 2023, Vienna (Austria).

"An integrated approach to elucidate the relationship between intracellular iron and magnetosome formation in magnetotactic bacteria", 8th International Meeting on Magnetotactic Bacteria, June 30 – July 4 2024, Bilbao (Spain).

List of Contents

List of Abbreviations

AAS Atomic absorption spectroscopy

AFM Atomic force microscopy

ANOVA Analyses of variance

AU Arbitrary units

BOX Bis-(1,3-dibutylbarbituric Acid) trimethine oxonol

CDF Cation diffusion facilitator

CET Cryo-electron tomography

CLEM Correlative light and electron microscopy

Cmag Cellular magnetic response

CRDR CellROX^{TM} Deep Red

CryoEM Cryo-electron microscopy

CryoSIM Cryo-structured illumination microscopy

CryoSXT Cryo-soft X-ray tomography

CV Coefficient of variation

DCW Dry cell weight

DLS Diamond Light Source

DLS Dynamic light scattering

DNA Desoxyribonucleic acid

dO_2 dissolved oxygen

Dps DNA-binding proteins from starved cells

EDTA Ethylenediaminetetraacetic acid

EDX Energy-dispersive X-ray spectroscopy

eBIC Electron Bio-Imaging Centre

EELS Electron energy-loss spectroscopy

EM Electron microscopy

EZ Enzymatic disruption

FCM Flow cytometer

FIB Focused ion beam

FLIM-FRET Fluorescence lifetime imaging microscopy-Förster resonance energy transfer

FSC Forward scatter

FSM Flask Standard Medium

HPH High-pressure homogenization

ICP-OES Inductively coupled plasma optical emission spectrometry

Mam Magnetosome-associated membrane proteins

MAI Magnetosome genomic island

MGM Minimal growth medium

Mms Magnetic particle membrane-specific proteins

MNPs Magnetic nanoparticles

MRI Magnetic resonance imaging

MS Mass spectroscopy

MS Magnetosomes

MTB Magnetotactic bacteria

nFCM Nano-flow cytometry

NP Nanoparticle

NTA Nanoparticle Tracking Analysis

OD Optical density

OFM Optimized flask medium

OGM Optimized growth medium

PBS Phosphate-buffered saline solution

PHA Polyhydroxyalkanoate

PI Propidium iodide

PdI Polydispersity index

PG-SK Phen Green™ SK

P1 Population 1

P2 Population 2

PCR Polymerase chain reaction

pO_2 Partial pressure of oxygen (Dissolved oxygen)

Pyr-546 Pyrromethene-546

q_{Fe} iron uptake rate

ROI Region of interest

ROS Reactive oxygen species

ROS^+ CRDR-stained cells

SDS Sodium dodecyl sulfate

SEM Scanning electron microscopy

SP Sonic probe disruption

SSC Side scatter

STED Stimulated emission depletion microscopy

STXM Scanning transmission X-ray microscopy

TEM Transmission electron microscopy

TES Trace elements solution

WCW Wet cell weight

XANES X-ray absorption near-edge structure analysis

XRD X-ray diffraction

List of Figures

List of Tables

Chapter 1. Introduction

1.1. Background and motivation

In recent years, nanomaterials, especially nanoparticles, have gained attention in many disciplines because of their physicochemical properties different from those seen in bulk materials [1]. Particularly, iron oxide magnetic nanoparticles have gathered significant attention due to their susceptibility to magnetic fields, their unique properties and diverse applications in nanobiotechnology and nanomedicine [2]. The magnetic properties of these particles combined with their small size, enable precise control and targeting which is crucial for applications such as drug delivery, magnetic resonance imaging (MRI), and hyperthermia treatment for cancer. The widespread adoption of chemically synthesized magnetic nanoparticles has been somewhat limited by issues related to biocompatibility, size uniformity, and the environmental impact of their synthesis [3].

In contrast, magnetosomes, which are produced by magnetotactic bacteria (MTB), present a promising alternative to chemically synthesized magnetic nanoparticles. These intracellular, membrane-enveloped, magnetic nanocrystals are typically composed of magnetite (Fe_3O_4) or greigite (Fe_3S_4) [4]. Unlike synthetic magnetic nanoparticles, magnetosomes offer a range of superior properties, including narrow size distribution, uniform morphology, high purity, and intrinsic biocompatibility [5]. The lipid membrane surrounding magnetosomes facilitates surface functionalization, making them particularly attractive for biomedical applications where biocompatibility and stability are crucial [6], [7]. Among MTB, *Magnetospirillum gryphiswaldense* MSR-1 has emerged as one of the most widely used model strains, largely due to its relative ease of cultivation compared to other strains, as well as the availability of already developed bioprocessing methods and genetic tools.

Despite the promising potential of magnetosomes and significant efforts to develop high-yield production platforms, scaling up their production to an industrial level remains challenging [8]–[11]. MTB are difficult to culture due to their specific growth requirements and their sensitivity to environmental conditions (e.g. some species require microaerophilic or anoxic conditions) [12]. **Figure 1.1** shows a schematic representation of the key steps in magnetosome bioprocessing using MTB. Enhancing overall magnetosome yields require optimization at multiple stages, not only through improvements in upstream processes—such as the development of new culture strategies and genetic engineering enabling bacterial and magnetosome high-yields [11], [13], [14]—but also, through advancements in downstream processes, including cell disruption and magnetosome purification, which are crucial for producing high-quality magnetosome preparations [10], [15], [16].

Overall, the future widespread application of magnetosomes in industry is currently hindered by several critical factors. Firstly, there is a limited understanding of the biomineralization process in MTB, which restricts our ability to manipulate and enhance magnetosome formation. Secondly, identification of growth and physiological bottlenecks in MTB cultures makes it challenging to achieve high biomass and magnetosome yields [17]. Thirdly, producing magnetosome batches with consistent structure, chain length, and functionality (batch-to-batch reproducibility) remains a significant hurdle [16]. Finally, the development of rapid and reliable characterization techniques for assessing magnetosome preparations is still at an early stage, further complicating the standardization and quality control needed for industrial production.

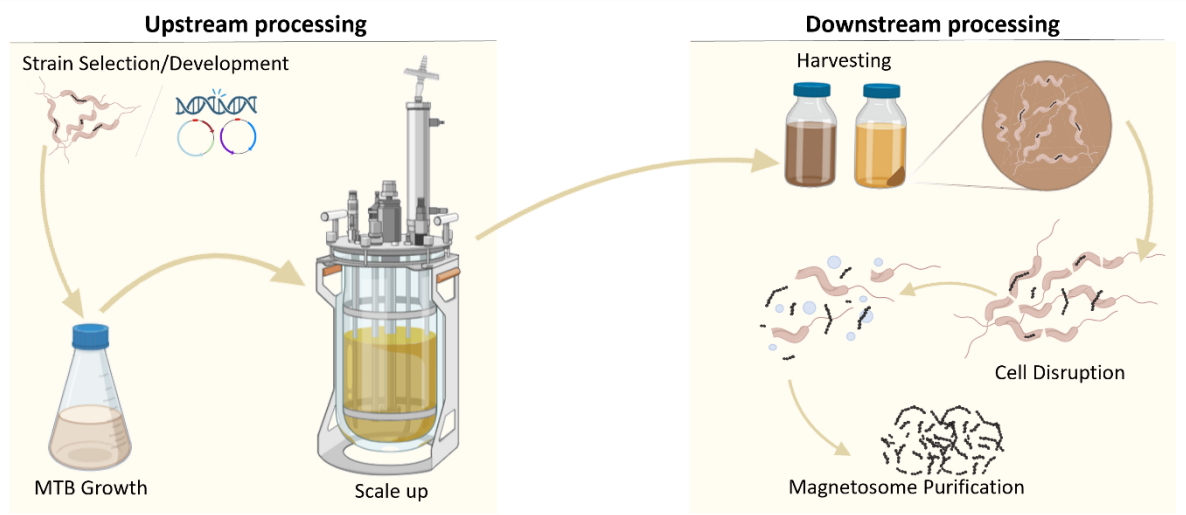

Figure 1.1. Schematic representation of magnetosome bioprocessing steps, including upstream and downstream processes.

1.2. Context of the thesis

This PhD project builds on the foundation of prior research conducted within our research group, which has focused on advancing industrially relevant bioprocesses for the production of magnetosomes. Significant efforts have been devoted to understanding the physiology and metabolism of MTB to optimize magnetosome production through enhanced bioprocessing strategies.

In previous work, MSR-1 was employed as a model microorganism to study key physiological processes in MTB, with flow cytometry (FCM) being established as a pivotal analytical technique [18]. FCM enabled the rapid assessment of critical parameters, including cell concentration, cell size distribution, intracellular iron content, and the accumulation of polyhydroxyalkanoate (PHA) granules. This led to the development of novel FCM methods tailored to MSR-1, but broadly applicable to other MTB

species, facilitating the monitoring of cellular health and physiology under various environmental conditions. This thesis extends these FCM methods by incorporating the detection of reactive oxygen species (ROS) into the array of physiological parameters, further enhancing the capability to analyse and optimize MTB cultures for magnetosome production.

A notable achievement was the development of a pH-stat fermentation approach that optimized the growth conditions for MSR-1, resulting in enhanced biomass yield, magnetosome formation, and intracellular iron accumulation [11]. By fine-tuning the concentrations of key substrates, such as lactic acid and sodium nitrate, a significant increase in both cellular magnetism and iron content was achieved, thus advancing the scalability of magnetosome production. This work demonstrated the importance of monitoring bacterial physiology during bioprocess development, which remains a fundamental element of subsequent research in this area.

In addition to fermentation process optimization, the group has also pioneered an integrated bioprocessing platform that includes downstream processing innovations. This includes the development of high-efficiency magnetosome recovery methods using high-gradient magnetic separation and an aqueous micellar two-phase system, providing a low-cost alternative to more traditional techniques, such as sucrose gradient ultracentrifugation [16]. These efforts not only improved the purity of magnetosome preparations but also enabled a continuous production platform, which is vital for future industrial applications.

Beyond magnetosome production, the group's research also explored the valorisation of microbial biomass waste generated during MSR-1 cultivation [19]. This microbial biomass waste, which is rich in proteins and PHA, presents an opportunity for further biotechnological applications, including biodegradable bioplastics and biofuels. The integration of these approaches into a magnetosome-based biorefinery concept has opened new avenues for sustainable magnetosome production, emphasizing the versatility and industrial potential of MTB-derived products.

This PhD project is designed to build on this body of work, particularly focusing on advancing our understanding of MTB physiology and bioprocess optimization. While some of the methodologies employed in this study differ from those previously used, including the introduction of new analytical techniques and process parameters, the overall aim remains aligned with the group’s core research interests. Specifically, this project seeks to further explore key steps in magnetosome biomanufacturing by generating insights that can be used in future work to develop improved strategies for more efficient and robust production processes.

1.3. Aims and objectives

Key factors limiting the industrial-scale production and application of magnetosomes are:

- A limited understanding of the biomineralization process.
- Identification of growth and physiological bottlenecks in MTB cultures.
- Inconsistencies in batch-to-batch reproducibility of magnetosome preparations.
- The lack of quick and reliable characterization techniques for assessing magnetosome preparations quality.

This thesis aims to address some of these challenges by exploring iron dynamics and the effects of oxidative stress on magnetosome biomineralization and bacterial growth, as well as assessing the impact of cell disruption on the integrity of magnetosome chains.

The specific research objectives of this PhD study are:

- To analyse the impact of varying extracellular iron concentrations on MSR-1 growth and magnetosome biomineralization.
- To investigate intracellular iron dynamics, focusing on the correlation between the intracellular iron pool and magnetosome content at the single-cell level.
- To assess the effects of different external stress factors, such as excess iron and exposure to hydrogen peroxide, on MSR-1 physiology and biomineralization processes.
- To examine the relationship between ROS and magnetosome biomineralization.
- To evaluate the efficiency and impact of various cell disruption techniques on magnetosome chain integrity.
- To evaluate the feasibility of nano-flow cytometry (nFCM) as a rapid quality assurance method for magnetosome preparations.

1.4. Thesis structure

This thesis is organized into six chapters, with each of the three experimental chapters addressing specific challenges that limit magnetosome production, as outlined in **1.3. section**. The experimental chapters follow a "journal paper" format and structure, each including an introduction, materials and methods, results and discussion, and conclusions sections.

- Chapter 1: This introductory chapter provides the context and background that motivates the research presented in this thesis. It includes an overview of the main aims and objectives of the project and outlines the structure of the thesis.
- Chapter 2: This chapter provides a comprehensive literature review that establishes the foundation for the research. It covers essential concepts related to MTB and magnetosome biomineralization, discusses the key limiting factors in magnetosome production, and provides background on the structural microscopy techniques employed in the experimental chapters.
- Chapter 3: This chapter explores the critical role of iron in magnetosome biogenesis, focusing on the study of the different intracellular iron pools and their relationship with magnetosome formation at the single-cell level. By utilizing a multi-scale approach that combines advanced imaging techniques with analytical methods, this chapter contributes to the understanding of the magnetosome biomineralization process.
- Chapter 4: This chapter examines the physiological responses of MTB to oxidative stress and its impact on magnetosome biomineralization. It also explores the potential role of magnetosomes as ROS scavenging agents, contributing to a deeper understanding of the physiological and growth dynamics of these bacteria.
- Chapter 5: This chapter evaluates the efficiency and impact of various cell disruption techniques on magnetosome chain length and integrity. It also explores the potential of nFCM as a quality assurance method for magnetosome preparations. The findings provide valuable insights into batch-to-batch reproducibility of magnetosomes preparations and propose nFCM as a promising characterization technique to facilitate quality check-points in magnetosome production platforms.
- Chapter 6: The final chapter presents the overall conclusions of this research and suggests potential directions for future studies.

Chapter 2. Literature review

Part of the content of this chapter has been adapted from the following publication:

Marta Masó-Martínez, Paul D Topham, and Alfred Fernández-Castané, "Magnetosomes: Biological Synthesis of Magnetic Nanostructures," in Fundamentals of Low Dimensional Magnets, R. K. Gupta, S. R. Mishra, and T. A. Nguyen, Eds. CRC Press, 2022.

2.1. Magnetotactic bacteria

MTB are a group of Gram-negative bacteria that possess the distinctive ability to orient themselves in a magnetic field. This behaviour is attributed to the presence of a type of intracellular magnetic nanoparticles called magnetosomes. Magnetosomes consist of nanosized magnetic crystals of greigite (Fe_3S_4) or magnetite (Fe_3O_4), arranged in a needle-like chain, and are naturally synthesized by these bacteria through a process called biomineralization.

MTB were independently discovered by Salvatore Bellini in 1963 and Richard Blakemore in 1974. In freshwater sites around Pavia, Bellini observed that certain microorganisms exhibited magnetic sensitivity, persistently swimming towards the magnetic North Pole. Bellini proposed the term "Magnetosensitive Bacteria" and hypothesized the existence of a biomagnetic compass within each cell [20]. This discovery initially did not receive much attention until Blakemore observed the presence of magnetosomes chains using electron microscopy [21]. Since then, MTB species have been used as a model organism to study biomineralization.

MTB species exhibit a wide range of diversity in terms of morphology, physiology, and phylogeny. Cell morphologies include rods, vibrios, spirilla, cocci, and ovoid bacteria, as well as giant and magnetotactic multicellular bacteria (**Table 2.1**). Usually, bacteria swim in run-and-tumbling movements in all directions. However, MTB are able to passively orient themselves in the Earth's magnetic field, which results in their movements being described by a run-and-reverse mechanism. It is hypothesized that orientation within a magnetic field provides an advantage over non-magnetic bacteria by helping them locate the optimal position within a vertical concentration gradient.

Table 2.1. Examples of morphological characteristics of magnetotactic bacteria and magnetosomes crystals.

Magnetotactic bacteria strain	Cell morphology	Magnetosome morphology	Crystal size (nm)	Ref
Magnetopirillum gryphiswaldense MSR-1	Spirillum	Cuboctahedral crystals	30-50	[22]
Magnetospirillum magneticum AMB-1	Spirillum	Cuboctahedral crystals	30-50	[23]
Magnetovibrio blakemorei MV-1	Vibrioid	Elongated pseudohexagonal prismatic crystals	60	[24]
Magnetococcus marinus MC-1	Cocci	Elongated pseudohexagonal prismatic crystals	30–110	[25]
Desulfovibrio magneticus RS-1	Rod	Bullet-shaped crystals	40-70	[26]
Candidatus Magnetobacterium bavaricum	Giant-rod	Tooth-shaped	110–150	[27]
Magnetococcus massalia MO-1	Cocci	Elongated cubo-octahedral	64	[28]

MTB are ubiquitous and globally distributed in nearly all aquatic habitats [12], [29]. These prokaryotes are found in both the Northern and Southern Hemispheres, in fresh and saline waters [30], [31]. Geographic location does not appear to be a conditional factor for MTB, but the chemical composition of the environment typically shares common characteristics [32]. All known MTB are microaerophiles, anaerobes or facultative anaerobes, and are predominantly found in sediments or chemically stratified water columns, specifically around the oxic-anoxic interface [4]. MTB have the capacity to swim in either direction along the magnetic field and maintain their position at their preferred oxygen concentration, due to a unique tactic response known as magneto-aerotaxis [5].

MTB are a phylogenetically diverse group of microorganisms affiliated to various groups within *Proteobacteria* phylum (including *Alphaproteobacteria, Deltaproteobacteria* and *Gammaproteobacteria), Nitrospirae* phylum and candidate division OP3 [12]. Only a few MTB strains, mainly found in the *Alphaproteobacteria* class such as *Magnetospirillum griphiswaldense* MSR-1 and *Magnetospirillum magneticum* AMB-1, have been successfully isolated and cultivated. *Magnetospirillum* genus is one of the most studied MTB groups, and both MSR-1 and AMB-1 are considered model strains for studying magnetosome biomineralization due to the availability of genetic engineering tools and laboratory cultivation protocols [33]–[35].

2.2. Magnetosomes

Magnetosomes can be found in all MTB species and are essential for their magnetotactic lifestyle. Whilst the use of magnetosomes as a navigational system seems to be the main function, there are studies that suggest other roles. For instance, the protective role of magnetosomes against metal stress [36], ROS [37], [38] and UV-B radiation has been studied [39], [40].

2.2.1. Structure and composition

Magnetosomes consist of an inorganic core (either magnetite or greigite) enveloped in a lipidic membrane (**Figure 2.1**). The chemical composition of the crystal core is species-specific and remains consistent, even when greigite-producing conditions are provided to a magnetite-producing MTB strain, and *vice versa*. [24]. Electron microscopy studies have revealed the wide diversity in magnetosome crystal shapes, including hexagonal, elongated prismatic, tooth-shaped, arrowhead-shaped, rectangular, and bullet-shaped morphologies [41]. In addition to morphology, crystal size is also a species-specific feature, ranging from 35 to 120 nm (**Table 2.1**). Cubo-octahedral shaped magnetosomes from *Magnetospirrillum* species are the most common and well-studied crystals among MTB. Magnetite is a mixed-valence iron oxide mineral that contains both ferrous (Fe^{2+}) and ferric (Fe^{3+}) iron in a 1 to 2 ratio, respectively [$Fe(II)Fe(III)_2O_4$].

The lipidic bilayer sorrounding the crystal is called magnetosome membrane and it is composed of various types of phospholipids and proteins, with a thickness of 5 to 6 nm [42], [43]. The lipid distribution within the magnetosome membrane closely resembles that observed in the cytoplasmic

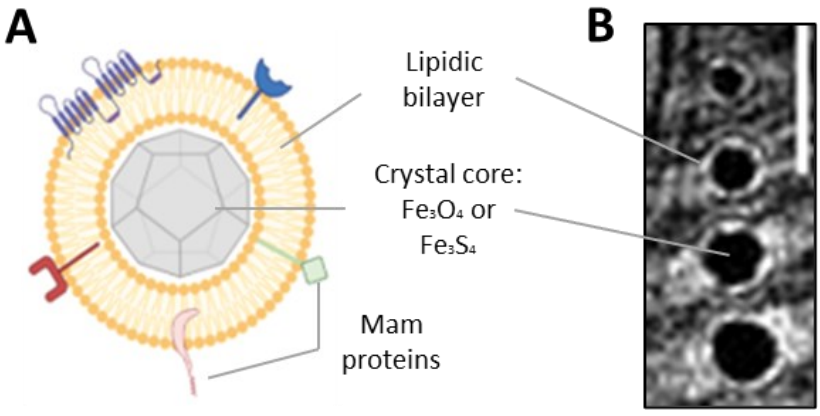

Figure 2.1. (A) Schematic structure of a single magnetosome. It is composed by a magnetic mineral crystal core encapsulated by a lipidic bilayer. Magnetosome membrane contains magnetosome-associated membrane proteins (Mam). Variation of shape and colour denote the variability of the Mam proteins. (B) Cryo-electron microscopy image of a magnetosome chain. Scale bar = 100 nm.

membrane. However, the protein content is distinct from that typically found in the cytoplasmic membrane, with over 25 magnetosome-associated membrane (Mam) proteins identified [44]–[46].

2.2.2. Genetics of magnetosome biogenesis

The genes involved in magnetosome formation are localized in a specific region of the bacterial chromosome called the genomic magnetosome island (MAI). It is estimated that around 30 *mam* and magnetic particle membrane-specific (*mms*) genes are involved in magnetosome biogenesis [44], [45], [47]–[49]. In *Magnetospirillum* species, MAI constitutes approximately 2% of their genomes. This region presents many features associated with genomic islands, such as putative insertion sites near tRNA genes, distinct levels of GC enrichment compared to the rest of the genome, and a large number of mobile genetic elements [50]. These features contribute to genetic instability, causing the MAI to undergo frequent genetic rearrangements, which can lead to various mutations and new phenotypes (including non-magnetic ones) when the bacteria are subjected to stress [51], [52].

Although gene size may vary between MTB species, the MAI is generally conserved and grouped in four different operons: mamGFDC, mms6, mamXY and mamAB [53]. While the mamAB operon is sufficient for rudimentary biomineralization, the other operons encode non-essential proteins that play crucial roles in controlling magnetosome size, morphology, and arrangement [54], [55]. **Table 2.2** lists the proteins encoded by these operons and their respective functions.

2.2.3. Magnetosome biomineralization

The mechanism underlying magnetosome formation in MTB is not yet fully understood. However, it is widely accepted that the process involves four key steps: (i) invagination of the cytoplasmic membrane; (ii) sorting of magnetosome proteins into the magnetosome membrane; (iii) iron transport into the magnetosome vesicle and subsequent mineralization into magnetite crystals and; (iv) magnetosome chain formation. These steps can occur simultaneously instead of one after the other. For instance, the sorting of magnetosome proteins and the appearance of small magnetite crystals can occur while the cytoplasmic membrane is still invaginating [56]. **Figure 2.2** provides a schematic overview of the pathways of iron uptake and biomineralization in MTB.

Table 2.2. Function of magnetosome-associated membrane (Mam) and magnetosome-specific (Mms) proteins in the process of magnetite biomineralization.

Function	Proteins	Encoding operon	Ref
Membrane invagination	MamB	*mamAB*	[54]
	MamI	*mamAB*	[45], [54], [57]
	MamL	*mamAB*	[54], [57]
	MamQ	*mamAB*	[54], [57]
	MamY	*mamXY*	[58]
Protein sorting	MamA	*mamAB*	[59]
	MamE	*mamAB*	[54], [60]
Iron transport	MamB	*mamAB*	[45], [61]
	MamH	*mamAB*	[45], [62]
	MamM	*mamAB*	[61], [63]
	MamZ	*mamXY*	[62]
Redox control	MamE	*mamAB*	[64]
	MamP	*mamAB*	[54]
	MamT	*mamAB*	[54]
	MamX	*mamXY*	[62]
	MamZ	*mamXY*	[62]
Crystal nucleation	MamO	*mamAB*	[65]
	MamE	*mamAB*	[65]
	MamM	*mamAB*	[61]
	MamI	*mamAB*	[46]
pH control	MamN	*mamAB*	[45], [54]
Crystal size and shape control	MamD	*mamGFDC*	[35]
	MamG	*mamGFDC*	[66]
	MamR	*mamAB*	[54]
	MamS	*mamAB*	[54]
	FtsZm	*mamXY*	[67]
	Mms6	*mms6*	[68]
	MmsF	*mms6*	[67]
Chain assembly	MamK	*mamAB*	[69]
	MamJ	*mamAB*	[70]

Variability in membrane invagination and detachment from the cellular membrane is observed among MTB species. For example, in *Magnetospirillum magneticum* AMB-1 the magnetosome vesicle remains connected to the cytoplasmic membrane, establishing a continuous connection between the magnetosome vesicle lumen and the periplasmic space, which may facilitate iron transport [56]. However, strains such as *Magnetospirillum gryphiswaldense* MSR-1 [43] or *Candidatus Magnetobacterium bavaricum* [71] exhibit fully detached magnetosome vesicles.

Compartmentalization of cellular processes prevents the mixing of contents between two compartments and allows the obtention of a strictly regulated chemical environment needed for some cellular mechanisms such as biomineralization. The formation of the magnetosome membrane is considered essential for magnetite biogenesis, as mutant strains incapable of forming magnetosome vesicles are unable to produce magnetite crystals [54]. Despite being indispensable, the formation of magnetosome vesicles is independent of magnetite formation, as studies have observed the presence of empty magnetosome vesicles under iron-starving conditions [56], [72], [73].

Unlike eukaryotic cells, which rely on specific proteins for membrane remodelling activities such as vesicle biogenesis, endocytosis, and cell division [74], MTB appears to employ distinct mechanisms for membrane bending. No homologous factors involved in eukaryotic membrane remodelling have been identified in MTB [43]. In species like MSR-1, membrane invagination can occur along the entire cell length without a defined initiation site [43]. Magnetosome membrane invagination is thought to involve Mam proteins, which are summarized in **Table 2.2**. These proteins may participate in membrane bending, given their structural similarities to proteins involved in membrane remodelling in other organisms [45], [54], [57], [75]. It is likely that larger protein complexes generate lateral pressure to deform the magnetosome membrane [76].

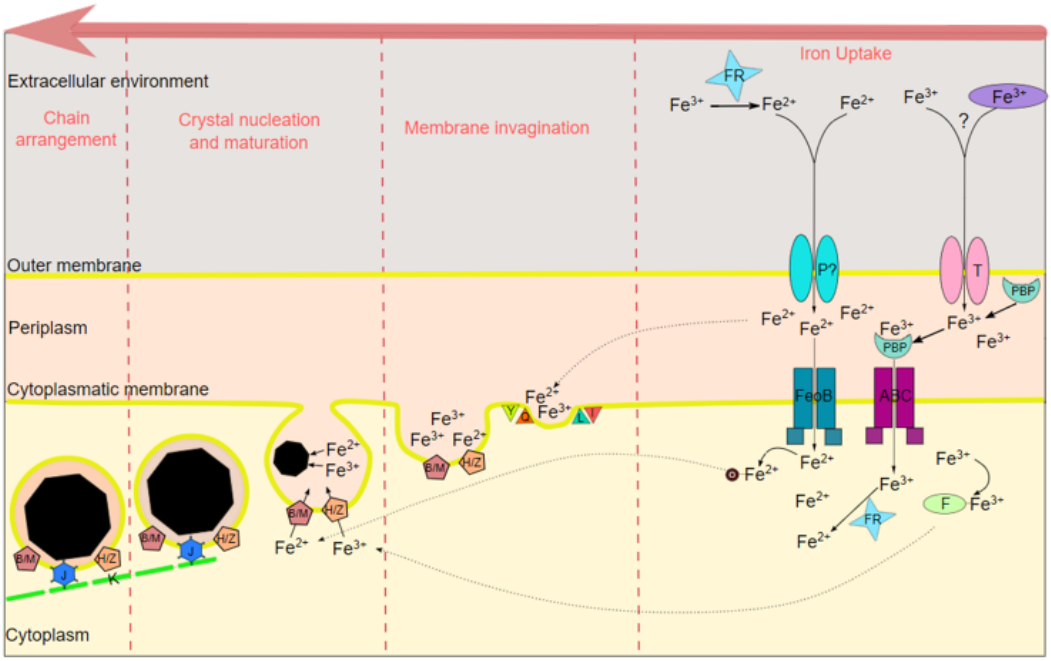

Figure 2.2. Schematic representation of cellular iron uptake and magnetosome biogenesis. Firstly, iron is taken up from the extracellular environment with the help of specific outer membrane transporters (T) or porin (P) transporters into the periplasm. In there, periplasmatic binding proteins (PBPs) sequester ferric iron and transport it to ABC transporters. In the case of ferrous iron, FeoB transporters are in charge of delivering the iron into the cytoplasm. Secondly, cytoplasmic membrane is invaginated and forms a vesicle with the help of Mam proteins. Thirdly, in the vesicle lumen iron is accumulated and crystal nucleation starts. Finally, once the crystal is formed, magnetosomes align themselves as a needle-like chain arrangement. If not specified, single capital letters denote respective Mam proteins. F, ferritin; FR, ferric reductase; O, unknown organic compound; ?, unknown mechanism.

Most of Mam proteins are localised on the magnetosome membrane or on the cytoplasmatic side of the cellular membrane [54], [77]. However, the mechanisms involved in their transport to the magnetosome membrane remain unclear. No specific localization signals have been identified, but some Mam proteins are suspected to be involved in this protein sorting process (**Table 2.2**).

An accumulation of intracellular iron is required before crystal nucleation starts. The mechanisms employed by MTB for iron uptake from the extracellular environment will be furthered discussed in **section 2.3**.

Magnetite crystal nucleation is more dependent on specific reaction conditions than other iron oxides due to the dual ferrous and ferric iron composition of magnetite. Nucleation requires an alkaline environment (pH>7), low redox potential, and a minimum iron concentration of 30 mM within the magnetosome vesicle [78]. The oxygen in magnetite originates from water rather than molecular oxygen [79].

Two models have been proposed for magnetite nucleation: one suggests direct co-precipitation of Fe^{2+} and Fe^{3+} to originate magnetite, while the other suggests the formation of intermediate precursor mineral phases prior to magnetite synthesis [80]. Regardless of the pathway, magnetite nucleation is highly regulated, with each vesicle containing only a single crystal, which nucleates preferentially near the magnetosome membrane rather than randomly within the vesicle lumen [56]. After nucleation, the crystal continues to grow until it reaches a species-specific size and shape.

During crystal maturation, MTB align magnetosomes into a linear chain with the help of a Mam actin-like protein, named MamK, that forms a filament analogous to the cytoskeleton, extending from one cell pole to the other and running close to the magnetosome chain [56]. The individual magnetic dipole moments of each magnetite crystal are insufficient to interact with magnetic fields, but the collective dipole moment of the aligned magnetosomes enables the cell to orient within a magnetic field [81].

2.2.4. Magnetosomes and magnetotactic bacteria applications

Magnetosomes exhibit properties that exceed those offered by synthetic magnetic nanoparticles [3], including narrow size distribution, high crystal purity, low aggregation tendency, facile functionalization and high biocompatibility [5]. These characteristics make magnetosomes highly attractive in a wide range of fields, particularly in nanomedicine, diagnostics, and environmental remediation.

In drug delivery, magnetosomes serve as promising carriers due to the relatively easy conjugation of drugs or other therapeutical agents to their lipidic magnetosome membrane [82]. For example, Sun *et al.* conjugated the commonly used antitumoral drug doxorubicin to the magnetosome membrane, effectively inhibiting cancer cell growth [83]; Deng *et al*. used magnetosomes to treat leukemia [84]; and Raguraman *et al.* proposed a magnetosome-based oral insulin delivery system to treat diabetes [85]. Magnetosomes have also been employed for gene delivery, offering potential in cancer treatment through the transportation of genetic material [86], [87]. Additionally, whole MTB cells have also been explored as drug carriers and showed tremendous potential due to their magneto-aerotactic behaviour that enables them to reach hypoxic tumour regions where other carriers struggle to penetrate [88].

Magnetosomes are also valuable as MRI contrast agents [89], [90]. They can enhance imaging sensitivity and target specific tissues by binding specific proteins on the magnetosome surface [91]–[93].

In biosensing, magnetosomes have been employed to detect proteins or DNA [94], as seen in the development of Magneto Immuno-PCR for Hepatitis B detection, which offers higher sensitivity than traditional methods [95]. Magnetosomes are also used in food industry applications for the detection of food-borne pathogens like *Salmonella* [96], *Staphylococcal enterotoxins* [97] or *Vibrio parahaemolyticus* [98] through immune-magnetic separation techniques that improve the accuracy of PCR-based tests.

Magnetic hyperthermia therapy consists of applying heat into tumoral cells to induce cell apoptosis [99]. The use of magnetosomes presents advantages over synthetic magnetic nanoparticles due to their capacity to functionalize the magnetosome membrane with specific proteins that will only target the cancerous tissue. The efficiency of magnetic hyperthermia using magnetosomes has been successfully demonstrated using various cell lines as well as in mice to treat several types of cancers such as breast cancer [100] and intracranial glioblastomas [101]–[103].

In bioremediation, MTB offer a sustainable approach to wastewater treatment by using magnetic separation to recover heavy metals adsorbed on their cell surfaces [104], [105], or by doping magnetosomes with some of these heavy metals [106], [107]. *Magnetospirillum* strains have also been applied to recover metals from electronic waste, indicating their potential in e-waste processing [108].

Overall, despite the wide range of potential magnetosome applications, availability of magnetosomes still remains a challenge because of low biomass and magnetosome yields, difficulty in scaling up the cultivation process and the complex purification process.

2.3. Iron uptake dynamics in magnetotactic bacteria

Iron is the fourth most abundant element on Earth's crust and is ubiquitous in all living organisms. It plays a vital role in biological systems due to its involvement in a wide array of essential biological processes, including redox reactions, due to its ability to donate and accept electrons [109]. Iron frequently functions as a cofactor in key metabolic pathways such as respiration, photosynthesis, nitrogen fixation, and methanogenesis. Its critical importance to living organisms is best exemplified by its role in DNA synthesis, where it serves as a cofactor for ribonucleotide reductase, the enzyme responsible for converting ribonucleotides to deoxyribonucleotides, the building blocks of DNA [110].

In the case of MTB, iron is particularly crucial due to the large quantities required for the synthesis of magnetosomes. Despite significant advances in understanding the biological and chemical pathways leading to magnetite biomineralization, the mechanisms by which MTB acquire iron from the environment and transport it to the magnetosome vesicles remain poorly understood.

Currently, there are three iron uptake models proposed (**Figure 2.2**). The first model suggests that iron is directly transported into magnetosome vesicles from the periplasm while the vesicle lumen remains connected to the cytoplasmic membrane, allowing direct transport or diffusion [111]. The second model proposes that once iron enters the cytosol, it binds to an unknown organic substrate and ferritin proteins for transportation, subsequently being released into the magnetosome vesicle [112]. Finally, The third model suggests that iron is transported through the cytoplasmatic membrane via general iron uptake systems and then transferred into magnetosome vesicles with the assistance of magnetosome-specific transporters [46]. The Mam proteins proposed to be involved in this transport include MamB and MamM for Fe^{2+}, and MamH and MamZ for Fe^{3+} transport [46]. MamB and MamM share a 47% sequence similarity and they both have been classified as CDF (cation diffusion facilitator) proteins, which are known for having the capacity of transporting divalent transition-metal cations using a proton motive force [49]. During magnetite formation, pH tends to drop due to the release of H^+ into the magnetosome lumen. The H^+ pumping activity of CDF proteins helps maintain optimal alkaline and redox conditions within the magnetosome compartment, which are necessary for magnetite biomineralization [113].

MamH and MamZ are also hypothesized to participate in magnetosome iron transport, as both contain major facilitator superfamily domains typical of membrane transporters found in bacteria [55]. MamH has the ability to bind to cations and transfer them into magnetosome vesicle [45], whereas MamZ presents a ferric reductase domain that suggests that it might participate in the control of redox balance.

Although evidence suggests the involvement of general iron uptake systems in intracellular iron transport, it has been proposed that an additional, magnetosome-specific iron uptake pathway exists. Moreover, general iron uptake mechanisms and homeostasis systems vary between MTB species. For instance, siderophore synthesis has been observed in species such as AMB-1, MV-1, and MS-1, but not in MSR-1 [114]–[116]. Supporting this hypothesis, deletion of the FeoB1 ferrous iron transporter in MSR-1 reduced but did not completely inhibit biomineralization, suggesting the existence of another, yet unidentified, iron uptake mechanism [117].

Moreover, earlier studies demonstrates that distinct intracellular iron pools exist: one pool supporting general biochemical reactions and the other dedicated to magnetite formation [112]. Previous assumptions proposed that 99.5% of intracellular iron was sequestered in magnetite crystals, but recent studies indicate that only 25-45% of intracellular iron corresponds to magnetite particles [118], [119]. To avoid iron toxicity, bacteria must tightly regulate iron homeostasis. In MTB, the Fur regulator plays a significant role in maintaining iron balance, as Fur-deletion mutants demonstrate reduced iron uptake and produce smaller, fewer magnetite crystals [120]. Additionally, MTB may mitigate toxic iron accumulation by storing excess iron in proteins such as ferritin or Dps. Uebe *et al*. reported the presence of ferritin-like proteins, bacterioferritins, and Dps proteins in MSR-1 [121]. Contrary to earlier suggestions that ferritin-like complexes are involved in intracellular iron transport to the magnetosome vesicle, Uebe *et al.* concluded that these proteins are not required for biomineralization but are instead involved in oxidative stress responses [121]. To further support this hypothesis, it has been observed that some bacterioferritins are regulated by the OxyR ROS regulator [38].

As seen throughout this section, significant knowledge gaps remain regarding how MTB acquire iron from their environment and transform it into magnetite crystals while keeping iron homeostasis. This thesis aims to further explore the iron dynamics and its correlation to magnetosome formation in MTB through advanced characterization techniques (**Chapter 3**).

2.4. Limitations and parameters affecting magnetosome bioprocessing systems

The bioprocessing of MTB and magnetosome purification involves both upstream and downstream challenges that significantly impact their production and quality. Addressing these limitations is key for the future development of efficient and sustainable production of high-quality magnetosome-based products.

2.4.1. Factors affecting MTB physiology and magnetosome formation

The growth and the formation of magnetosomes in MTB are influenced by several key environmental factors, including nutrient composition, iron availability, oxygen concentration, pH, temperature, and redox conditions (**Figure 2.3**).

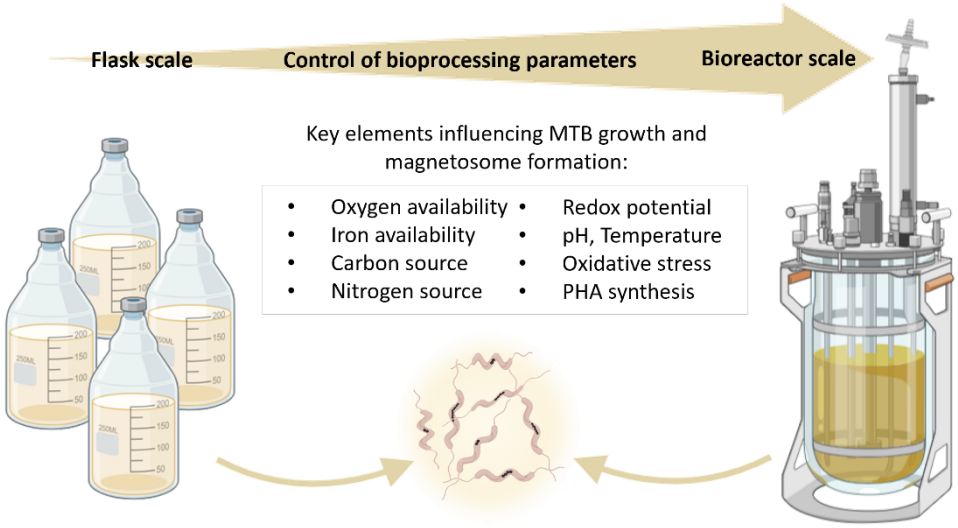

Figure 2.3. Main factors influencing magnetotactic bacteria growth and magnetosome production yields at flask and bioreactor scale.

Nutrient composition in the growth medium is crucial, with carbon and nitrogen being key elements. Carbon serves as an energy source, and its limitation can slow cell metabolism and halt non-essential processes like magnetosome formation [122]. MTB species use organic acids such as lactate, succinate, acetate or pyruvate as electron donors and main source of carbon, with lactate being the most commonly used in both small and large-scale cultures [8], [9], [11], [123]. Nitrogen is vital not only for biosynthesis of biomolecules such as amino acids [124], but can also be used as a terminal electron acceptor when oxygen is scarce [123].

Iron availability is a crucial factor for magnetosome synthesis, as MTB can accumulate iron up to 4% of their dry weight [4]. Commonly used iron sources include ferric citrate, ferric quinate, ferric malate, and ferrous sulfate [12], [125]. Ferrous or ferric salts at 20 to 50 µM concentrations are generally sufficient to allow for both growth and magnetosome formation [32]. However, iron concentrations above 200 µM have been reported to inhibit cell growth [126], [127]. Nevertheless, as explored in **Chapter 3**, higher iron concentrations do not necessarily exhibit toxicity under certain conditions. Additionally, iron availability influences gene expression in MTB, particularly genes involved in oxidation-reduction processes, ion binding and transport, and iron metabolism [128].

One of the most important factors that affects magnetite biomineralization is the oxygen concentration. MSR-1 can grow under aerobic, microaerobic and anaerobic conditions [33]. Under aerobic conditions, magnetite formation is inhibited and higher cell densities are obtained, whereas under limiting oxygen conditions, magnetosome synthesis is induced but lower cell growth is generally observed [11], [33]. Comparative transcriptomics analysis between microaerobic and aerobic cultures revealed differences in gene expression regulation of genes involved in cell metabolism, nutrient transport and cellular regulation [129]. Under microaerobic conditions, nutrient transport and physiological metabolism were reduced, whereas dissimilatory denitrification pathways were activated. MSR-1 can also employ nitrate as a terminal electron acceptor, leading to the formation of larger and more units of magnetite crystals (longer chain), although growth may be limited by toxic intermediates from denitrification [123], [130], [131]. The study of the extracellular metabolome of microaerobic and aerobic cultures revealed differences in catabolic and anabolic metabolic routes related to cell growth, protein synthesis of proteins involved in magnetosome biogenesis, and butanoate metabolism involved in the synthesis of PHA granules [17].

pH and temperature are also two parameters that require monitoring as they affect cell growth and magnetosome synthesis. The model strain MSR-1 thrives at temperatures around 28-30°C and a pH of 6.8-7. Deviations in pH can result in aberrant magnetosome crystals, while temperature fluctuations within the range of 10-20°C have less impact on magnetosome formation. However, temperatures outside this range can abolish magnetosome production [132].

Oxidation-reduction potential is an important parameter to monitor during bacterial cell growth, as small changes can affect its growth [133]. Reducing conditions were found to be best for magnetosome formation, ranging from -250 mV to -500 mV [134], and perturbation of these conditions inhibited magnetosome biomineralization [132]. While redox conditions do not alter the genetic regulation of magnetosome-associated genes, they can affect other metabolic pathways involved in magnetosome formation, such as denitrification, the respiratory chain, and iron uptake [129], [135]. For instance, the deletion of the *cbb3* terminal oxygen reductase in MSR-1 impairs biomineralization, indicating that this oxidase may act as an oxygen sensor, helping to maintain appropriate redox balance for magnetosome formation [136].

Oxidative stress, a consequence of excessive ROS production, is another critical factor that influences cell physiology. ROS, which are by-products of oxygen reduction in metabolic processes, can cause significant cellular damage when their accumulation surpasses the antioxidant cellular defence mechanisms [137]. This damage includes the oxidation of nucleic acids, proteins, and lipids, which directly compromises cell viability [138]. In the context of magnetosome formation, elevated

intracellular levels of iron, necessary for magnetosome synthesis, can accentuate ROS production through the Fenton reaction, where hydrogen peroxide (H_2O_2) reacts with ferrous iron to generate highly toxic hydroxyl radicals (•OH) [139]. Consequently, controlling ROS levels and iron homeostasis during MTB growth is crucial not only for maintaining cell health and viability but also for ensuring efficient magnetosome production. In *Magnetospirillum* strains, it has been seen that the global regulator OxyR participates in magnetosome biomineralization regulation as it is involved in the expression of antioxidant genes, iron-metabolism regulator genes and iron storage proteins genes [38], [40], [140]. Additionally, magnetosomes may have a ROS scavenging role, contributing to lowering overall ROS levels and further protecting the cell from oxidative stress, as they possess peroxidase-like activity [37]. The impact of oxidative stress in MSR-1 physiology and magnetosome synthesis is further explored in **Chapter 4**.

Other metabolic pathways, such as PHA synthesis, also participate in the overall physiology of MTB. PHA synthesis is upregulated under nutrient-limited conditions or oxidative stress, particularly when there is an excess of carbon source [141]. Monitoring PHA synthesis is important because PHAs serve as reservoirs of reducing power, which helps maintain intracellular redox balance and mitigate the formation of ROS [142]. By sequestering reducing equivalents (e.g. NADH, NADPH), PHAs prevent the accumulation of excessive reducing agents that could otherwise participate in redox reactions, leading to uncontrolled ROS production and oxidative damage [143]. Additionally, there is evidence that suggests the existence of an energy competition between magnetosome and PHA synthesis [13], [18], [144]. For instance, when PHA synthesis was genetically suppressed, an increase in magnetosome production was observed, indicating that the resources allocated to PHA synthesis can directly influence magnetosome biosynthesis [145]. Research carried out on AMB-1, showed that under anaerobic conditions, PHA content decreases, while under aerobic conditions, PHA production increases. [144]. This demonstrates that oxygen availability not only influences magnetosome formation but also impacts PHA metabolism, further highlighting the intricate balance between these two key physiological processes.

2.4.2. Cultivation strategies for mass production of magnetosomes

The use of bioreactors enables the growth of MTB at relatively high cell densities. MSR-1 flask cultures yield a maximum cell growth of 1-1.5 OD_{565} [33], [126], whereas bioreactor cultures can yield approximately 10-fold higher biomass concentrations. Table 2.3 shows a summary of biomass and magnetosome yields obtained using different culture strategies carried out at bioreactor scale. Increasing cell growth yield is advantageous, as a higher number of available cells can lead to greater

magnetosome production. Bioprocessing parameters such as the oxygen levels, nutrient supply and pH can only be controlled using bioreactors. Most laboratory scale fermenter studies are performed in volumes between 1 – 7.5 L. However, there is a small number of reports in which the process is scaled up to 42 L to demonstrate that cultivation can be applied to pilot plant production scale [8], [9], [118].

Table 2.3. Summary of magnetosome and cell yields of various MTB strains cultured using different strategies and culture media.

Strain	Cultivation strategy	Medium	Scale (L)	Cell yield (g DCW L^{-1})	OD_{565}	Magnetosome yield (mg Fe L^{-1})	Reference
MSR-1	Batch	FSM	4	0.4	1.4	7.9	[33]
AMB-1	Batch	FSM	4	0.48	2.5	4.7	[33]
MSR-1	Fed-Batch	OFM	42	2.17	7.24	41.7	[8]
MSR-1	pH-stat	OFM	42	-	12.2	83.23	[146]
MV-1	Batch	OGM	5	-	-	64.35	[147]
MSR-1	Semicontinuous	OFM	42	9,6	42	356.52	[9]
MSR-1	Semicontinuous	OFM	7.5	7.59	30.4	225.53	[9]
MSR-1	Fed-batch	MGM	40	2.4	8	10	[10]
MSR-1	pH-stat	FSM	5	4.2	16.6	54.3	[11]

OFM = Optimized flask medium; OGM = Optimized growth medium; MGM = Minimal growth medium; FSM = Flask Standard Medium.

Heyen and Schüler carried out what is considered to be the first bioreactor-type study that optimized cultivation conditions for various MTB strains applying different dissolved oxygen (dO_2) concentrations and optimized flask standard media (FSM) [33]. Oxygen was regulated by establishing an automatic cascade control system by gassing nitrogen and air separately. The authors determined that magnetite biomineralization is optimal under a 20 mbar O_2 threshold. Sun *et al.* opted for a microoxic fed-batch oxystat strategy in a 42 L fermenter [8]. In this aeration approach a fixed airflow rate was used and regulation of dO_2 was manually controlled by changing the agitation speed when a decrease of cell growth was detected. Liu *et al.* improved the feeding strategy by proposing a pH-stat feeding system to maintain optimal carbon, nitrogen and iron concentrations [146]. In this strategy, a feeding solution containing carbon, nitrogen and iron sources was employed to regulate and maintain the pH. Different sodium lactate concentrations and nitrogen sources were tested, and the work concluded that MSR-1 growth yield was higher when low concentrations of sodium lactate were used. Zhang *et al.* proposed a semi-continuous nutrient-balance feeding culture strategy [9]. In this approach, OFM (optimized flask medium) was modified to reduce the accumulation of Na^+ and Cl^- ions, thereby preventing an increase in osmotic potential, which can inhibit cellular growth and, consequently, magnetosome formation. Following this strategy, the authors reached the highest magnetosome and cellular growth yields shown to date. Our group reported the second highest production yields after Zhang *et al.* by

developing a simple pH-stat cultivation strategy without the need for sophisticated control tools, such as extremely sensitive dO_2 probes [11]. dO_2 was maintained below 1% air saturation by manually adjusting the airflow and agitation between 100 and 500 rpm. The effect of lactic acid and nitrate was also studied: cell growth was enhanced at lower lactic acid concentrations, whereas magnetosome production increased at high lactic acid concentration. Therefore, a balance must be reached between biomass and magnetosome production when designing new fermentation strategies. Cell physiology was also monitored throughout all the fermentation experiments with the help of FCM analysis [11], [18]. The study of MTB physiology of high-density cultures has not been investigated enough. Understanding which physiological parameters limit biomass and magnetosome yields could enhance industrial magnetosome production.

2.4.3. Cell disruption

Magnetosomes are intracellular products, and therefore they need to be released from the cells prior to their purification. This process involves breaking the cell wall and membrane while preserving the functional integrity of magnetosome chains, which is important for certain applications. For instance, in the biomedical industry, batch-to-batch consistency is essential, and a solution containing magnetosome chains of varying lengths is not ideal for standardization and reliable performance.

Cell disruption techniques are classified into mechanical and non-mechanical methods (**Figure 2.4**). Mechanical methods involve physical forces to break the cell structure (e.g. sonication, French press, bead milling), while non-mechanical methods rely on chemical or enzymatic processes to achieve cell lysis [148].

Sonication, which employs high-frequency sound waves to generate shear forces, is widely used for cell disruption due to its effectiveness in lysing cells. However, improper optimization can lead to damage of sensitive intracellular components. [149]. Kobayashi *et al.* optimised probe sonication for the disruption of *Magnetospirillum magnetotacticum* MS-1 [150], while Alphandéry *et al.* employed an ultrasonic bath to disrupt AMB-1 [100], [151]. It is important to note that prolonged ultrasonication can cause extensive breakage of magnetosome chains and agglomeration [15], [151].

The French press is another mechanical technique that employs high pressure to force cells through a narrow valve, causing them to burst [152]. This method has been extensively applied to MTB, including MS-1 [42], MSR-1 [49], [153], [154] and AMB-1 strains [155]. High-pressure homogenization (HPH), a technique similar to the French press, is widely used for microbial cell disruption due to its high

efficiency, versatility of operation (batch or continuous) and scalability [156]. HPH has also been employed in the disruption of MSR-1 [157]–[159].

Chemical disruption of MTB has been less frequently reported, primarily due to the potential damage to magnetosome membranes [49], [150], [151]. Enzymatic treatment, such as using lysozyme, has been applied mainly to study periplasmic and cytoplasmic fractions in MTB cells, rather than for efficient cell disruption[160]–[162].

Overall, although various cell disruption techniques are available, selecting the most suitable method for MTB downstream processing is critical to balancing efficient cell lysis with the preservation of magnetosome chain integrity. A detailed discussion of some of these approaches and their implications for magnetosome recovery is presented in **Chapter 5**.

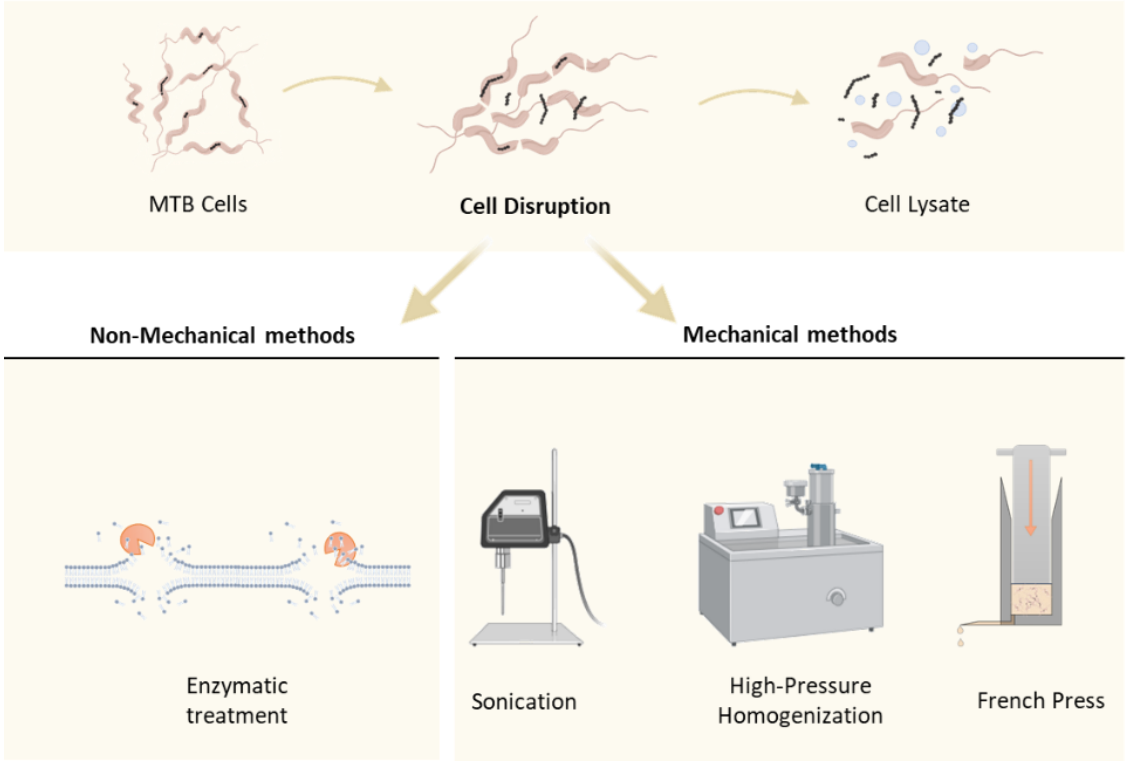

Figure 2.4. Overview of the cell disruption process in magnetotactic bacteria, highlighting both mechanical and non-mechanical methods. The figure illustrates the most highly employed cell disruption techniques, including enzymatic lysis, sonication, high-pressure homogenization and French press.

2.5. Biomineralization characterization

There are several approaches to studying magnetosome biomineralization. To determine whether a culture is producing magnetosomes, researchers often employ rapid qualitative tests to distinguish between magnetic and non-magnetic cell populations. For example, magnetic bacteria display a shimmering effect when cell suspensions are placed on magnetic stirrer plates [163]. The presence of dark-coloured cell pellets (Figure 2.5) and dark bacterial colonies are also indicators of magnetosome production. The magneto-spectrophotometric assay of suspended cells provides an indirect assessment of cellular magnetosome content by rapidly evaluating the cellular magnetic response (C_{mag}) of the culture [164]–[166].

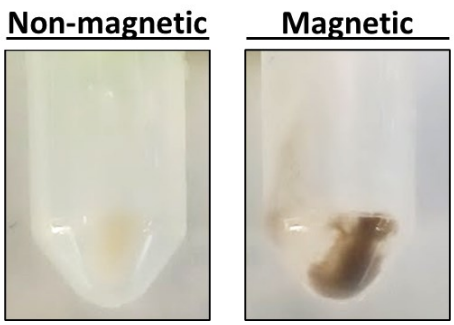

Figure 2.5. Cell pellets of *Magnetospirillum gryphiswaldense* MSR-1, illustrating the colour differences between non-magnetosome-producing (non-magnetic) and magnetosome-producing (magnetic) cells.

Monitoring iron content is also a crucial aspect of studying biomineralization. Spectroscopic techniques, such as inductively coupled plasma spectrometry (ICP) and atomic absorption spectroscopy (AAS), are widely used to estimate total intracellular iron content. When applied to whole cells, these measurements provide an approximation of magnetosome content, as they do not distinguish between iron contained within magnetosomes and iron present in other cellular components. However, when measured in purified magnetosome samples, total iron content closely correlates with magnetosome content, providing a more accurate assessment [11], [117], [167]. To measure ferrous iron concentrations ferrozine assay is also commonly employed [119]. FCM has also been used as a rapid and efficient analytical technique, offering insights into cell physiology and providing information about the intracellular iron pool by using a fluorescent iron probe [168].

Nevertheless, microscopy techniques, particularly transmission electron microscopy (TEM), are among the most widely used and direct methods for determining magnetosome content. TEM allows for the visualization of magnetosomes at high resolution, providing detailed information on their structure and organization within the cells [41], [169].

2.5.1. Microscopy-based techniques

Structural information is key to understand biomolecular functions and cellular processes. The field of structural biology is continuously evolving with advancements in techniques and methodologies to better unravel how the cellular machinery operates [170]. Due to the inherent complexity of biological systems, no single technique can capture all structural, dynamical, and functional information [171]. Therefore, integrating multiple techniques often provides a more accurate and holistic view of cellular events.

Microscopy-based techniques are fundamental to understand intracellular structural organization and its dynamic reorganization during cellular processes [172]. A variety of microscopy methods are available, each tailored to specific sample types and research needs. Conventional light microscopy, although widely accessible and suitable for imaging live samples, is limited in resolution, particularly for structures smaller than 1 µm. Fluorescence tags can enhance resolution up to 200 nm [173], especially in techniques like confocal microscopy and structured illumination microscopy (SIM) [174], [175]. However, fluorescence microscopy is limited to visualizing tagged regions, leaving other cellular structures undetected.

2.5.1.1. Electron-based microscopy techniques

Electron microscopy (EM) offers superior spatial resolution, revealing ultrastructural details at the nanoscale. Techniques such as scanning electron microscopy (SEM) and atomic force microscopy (AFM) provide topographical information, while TEM reveals intracellular structures.

Although conventional electron-based microscopy techniques are ideal to visualize highly resolved structures (down to 5 nm), they present some limitations. Sample preparation is often labour-intensive and time-consuming, with critical sample thickness requirements, typically around 100 nm. In addition, achieving sufficient contrast to visualize cell structures often necessitates chemical fixation, which may alter the sample [176]. In biological studies, preserving specimens in their near-native, hydrated state is crucial for gaining accurate structural, functional, and organizational insights. The development of cryo-electron microscopy (cryoEM) addressed this need by vitrifying the samples, enabling imaging in a near-native state without staining or sectioning [177]. CryoEM has become a popular tool for determining the three-dimensional structures of macromolecules, often in combination with cryo-electron tomography (CET) for detailed 3D reconstructions [178]. This approach has been instrumental in revealing cellular mechanisms, such as the determination of SARS-CoV-2

spike glycoprotein structure, a critical factor in virus-host cell attachment, that facilitated the development of therapies and diagnostics tools [179].

However, CET has limitations, particularly the low penetration power of electrons, which reduces resolution for samples thicker than 0.5 µm. This limitation has been evident in the imaging of whole eukaryotic cells, where the sample thickness compromises resolution [180]–[182]. Techniques such as focused ion beam (FIB) milling can be employed to reduce sample thickness but carry the risk of sample damage.

MTB and magnetosomes have been characterized using a variety of these techniques. TEM remains the primary method for examining magnetosome morphology and crystal structure [41], while energy-dispersive X-ray spectroscopy (EDX), often coupled with SEM or electron energy-loss spectroscopy (EELS), is used to determine the chemical composition [183]–[186]. Although not an electron-based technique, X-ray diffraction (XRD) has also been employed to analyse magnetosome crystal structure and purity in various MTB strains [187], [188]. Similarly, electron diffraction provides structural information but at the single-particle level. Besides magnetosomes, TEM enabled the identification of intracellular inclusion bodies (e.g., sulfur, polyphosphate, and PHA granules) [145], [189], [190] and diverse flagellar systems in MTB [191].

CryoEM and CET have also been employed to study magnetosome formation. Raschdorf *et al.* used CET to elucidate the role of Mam proteins in redox balance control and magnetosome membrane invagination [43], [62]. 3D reconstructions demonstrated that MSR-1 magnetosome vesicles detach completely from the cytoplasmatic membrane at the end of the invagination process [43]. Katzmann *et al.* studied magnetosome chain arrangement through CET, characterizing the associated cytoskeletal filament in various MSR-1 mutant strains [69]. Cornejo *et al.* employed CET to investigate magnetosome vesicle growth in AMB-1, proposing a two-step growth mechanism regulated by a biomineralization-dependent checkpoint [73]. Thus, structural characterization has played a significant role in understanding the cell biology behind magnetosome formation and its regulation.

2.5.1.2. Soft X-rays microscopy

Cryo-soft X-ray tomography (cryoSXT) represents an attractive alternative to CET. This synchrotron-based technique achieves resolutions down to 25 nm [192] and uses X-rays instead of electrons as its illumination source. Unlike electrons, X-rays can penetrate deeper, allowing for imaging of thicker samples, such as whole cells, without the need for sectioning.

Currently, cryoSXT is available at four synchrotron facilities: U41-TXM Bessy II (Berlin, Germany), XM2 Advanced Light Source (Berkeley, California, USA), Mistral ALBA (Barcelona, Spain) and B24 Diamond Light Source (Didcot, UK). Sample preparation for cryoSXT follows the same vitrification protocol used for cryoEM, preserving samples in a near-native state. An added advantage of cryopreservation is enhanced sample resistance to radiation damage, allowing for longer exposure times [193].

Soft X-rays have been successfully used to image a wide variety of specimens, including bacteria like *Escherichia coli* [194], yeasts such as *Saccharomyces cerevisiae* and *Saccharomyces pombe* [195], algae [196], Hepatitis C virus [197], and eukaryotic cells [198]. Unlike, hard X-rays, which have energies between 5 and 30 keV and are highly penetrating, soft X-rays have lower penetration depths, but are particularly advantageous for imaging biological samples. This is due to their ability to interact with light elements abundant in these organic materials (e.g. carbon, nitrogen, oxygen), as these elements absorption K-edges fall within the soft X-ray spectrum (0.1–1 keV) [199], providing element-specific contrast and detailed chemical information. In particular, the "water window", a spectral region between the carbon (284 eV) and oxygen (543 eV) absorption edges (**Figure 2.6A**), is commonly used for imaging [200]. This range takes advantage of the natural absorption characteristics of biological

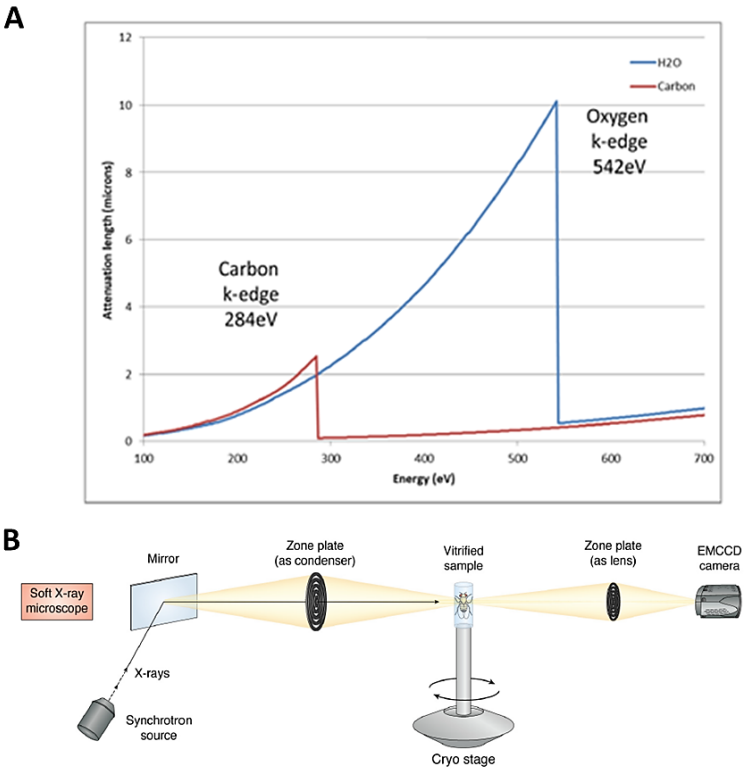

Figure 2.6. (A) K-absorption edges of carbon (284 eV) and oxygen (543 eV) within the "water window," where water (blue) is transparent, allowing carbon-rich structures (red) to produce sufficient contrast for imaging. (B) Schematic representation of a soft X-ray microscope. Images were adapted from (A) Groen *et al*. 2019 [176] and (B) Bayguinov *et al*. 2020 [202].

materials—carbon-rich elements absorb strongly, while water, which is oxygen-rich, absorbs weakly—creating high-contrast images of biological structures without the need to add any staining agents [201]. **Figure 2.6B** illustrates the principle of a cryoSXT microscopy. Briefly, X-rays from a synchrotron radiation source are passed through a bend magnet on the synchrotron ring and led to the microscope via a mirror. Once inside the microscope, x-rays are delivered to the sample, which is mounted on a cryo-stage, via a condenser zone plate. The resulting projections are directed via an objective zone plate to the detector or camera [202].

Soft X-rays-based techniques, such as scanning transmission X-ray microscopy (STXM), soft X-ray ptychography and cryoSXT have been also employed to characterize magnetosome biomineralization, as well as for characterizing magnetotactic holobiont specimens [203]–[205]. For instance, Zhu *et al.* employed soft X-ray ptychography to achieve a record spatial resolution of 7 nm, the highest reported for soft X-ray imaging below 1 keV, providing unprecedented detail in the study of magnetosome structures both intracellularly and extracellularly, with high chemical sensitivity [204]. Similarly, Le Nagard *et al.* employed STXM to conduct time-course chemical mapping, revealing that Fe^{3+}-rich particles are initially produced and gradually reduced to form magnetite, with organized chains of magnetosomes forming during later growth stages [203]. Furthermore, Chevrier *et al*.'s cryoSXT characterization of magnetotactic holobionts emphasized the evolutionary significance of collective magnetotaxis, raising important questions regarding the origins of symbiosis between eukaryotes and magnetotactic bacteria [205].

2.5.1.3. Correlative microscopy studies

Correlative microscopy studies combine the capabilities of two imaging techniques that complement each other to answer complex biological questions that otherwise could not be resolved by a single technique [206].

Most correlative studies synergise fluorescence microscopy and a high-resolution technique. Fluorescence microscopy is used to identify and localize molecules of interest, allowing the study of molecular interactions and dynamics within a biological system [207], while the high-resolution technique provides detailed ultrastructural information. Originally, correlative microscopy was developed to combine visible light microscopy with electron microscopy, but different modalities can be combined depending on the specific research question. A common correlative approach in biology, particularly for eukaryotic cells [208] and microorganisms [209], is the combination of cryo-fluorescence microscopy with cryoEM (CryoCLEM – correlative light and electron microscopy). Cryo-

fixation protects against radiation damage and extends the lifespan of fluorescent labels [210]. However, data correlation can be challenging due to differences in volume, thickness, and spatial resolution between light and electron microscopy. CryoSXT emerges as a bridge between these two techniques as the resolution gap is not as large [211]. When combined with super-resolution techniques like 3D-SIM, cryoSXT can be particularly powerful, as 3D fluorescence data can be correlated with tomographic images [212].

Although still relatively new, correlative light and soft X-ray microscopy have been employed to investigate various cellular processes, including mitochondrial fission in mammalian cells [213], reovirus intracellular release pathway [212] or the cellular structural changes that causes Hepatitis C virus during infection [197]. However, this approach has not yet been applied to MTB, presenting exciting opportunities for characterizing MTB and advancing our understanding of magnetosome formation at the single-cell level. In **Chapter 3**, a correlative light and soft X-ray microscopy study on MTB is presented, demonstrating its potential in this field.

Some correlative microscopy studies combining different microscopy techniques have been conducted on MTB. Günter *et al.* used a combination of fluorescence lifetime imaging microscopy-Förster resonance energy transfer (FLIM-FRET) and stimulated emission depletion (STED) microscopy to further investigate the role of MamK and MamJ in the arrangement of magnetosome chains in MSR-1 [214]. Woehl *et al.* performed in vivo imaging of AMB-1 cells immobilized in a fluid cell, using scanning-TEM and fluorescence imaging to assess cell membrane integrity. Surprisingly, the cell membranes exhibited minimal radiation damage when exposed to low electron doses [215]. Finally, Li *et al*. developed a strategy for the phylogenetic and structural characterization of uncultured MTB at the single-cell level by pairing fluorescence microscopy and SEM [216], [217]. These studies highlight the significant potential of correlative microscopy techniques for characterizing, investigating dynamic cellular processes and elucidating the intricate interactions and functions of magnetosomes in MTB, regardless of the specific combinations of microscopy techniques used. **Chapters 3** and **4** exemplify this potential; while each presents distinct advantages and limitations, the correlative microscopy techniques employed in these chapters provided valuable insights tailored to their respective research objectives.

Chapter 3.

An integrated approach to elucidate the interplay between iron uptake dynamics and magnetosome formation at the single-cell level in *Magnetospirillum gryphiswaldense*

The content of this chapter has been adapted from the following publication:

"An integrated approach to elucidate the interplay between iron uptake dynamics and magnetosome formation at the single-cell level in *Magnetospirillum gryphiswaldense*". M. Masó-Martínez, J. Bond, C. A. Okolo, A. C. Jadhav, M. Harkiolaki, P. D. Topham, A. Fernández-Castané. ACS Appl. Mater. Interfaces, vol. 16, 2024. DOI: 10.1021/acsami.4c15975

3.1. Introduction

Iron constitutes an essential element in all living organisms due to its participation in a wide range of fundamental biological processes such as respiration, nitrogen fixation and DNA synthesis [109]. Particularly, iron plays a crucial role in a group of Gram-negative bacteria known as MTB. These bacteria biomineralize large amounts of iron (up to 4% of their dry weight) to form a type of magnetic nanoparticles, known as magnetosomes, through a complex metabolic process.

Magnetosomes are nanoscale organelles consisting of membrane-coated magnetic crystals of magnetite (Fe_3O_4) or greigite (Fe_3S_4) usually arranged as a needle-like chain and their main function is to act as geomagnetic navigational systems [46]. Magnetosomes have tremendous potential for biotechnological and biomedical applications due to their unique properties such as narrow size distribution and biocompatibility [218]. However, their industrial biomanufacturing potential is hindered by their relatively limited growth and low magnetosome production yields [11], [219]. This limitation is likely due to the insufficient understanding of the magnetosome biomineralization process at the single-cell level, which may involve several factors, such as intrinsic energetic constraints (e.g., ATP generation/consumption), nutrient availability, the influence of secondary metabolites, or

environmental conditions [11]. Addressing these knowledge gaps could help unlock the full production potential of magnetosomes.

Despite the efforts invested in understanding the metabolic and biochemical pathways responsible for magnetite biomineralization, the mechanisms by which MTB uptake iron from the environment, its intracellular storage, and internalisation into the magnetosome vesicle remain poorly understood. Several models have been proposed. The first model suggests that iron is directly transported into magnetosome vesicles from the periplasm when the vesicle lumen is still in contact with the cytoplasmatic membrane by direct transport or diffusion [5]. The second model proposes intracellular accumulation of Fe^{2+} and ferritin and subsequent transportation to the magnetosome vesicle for its co-precipitation into magnetite [112]. Finally, the third model suggests that Fe^{2+} and Fe^{3+} are transported through the cytoplasmatic membrane via general iron uptake systems, such as the Feo (ferrous iron transport) system [117], [220] and transported into magnetosome vesicles with the help of magnetosome-specific transporters (MamB, MamM, MamH, MamZ) [46], [49], [55] with or without the help of ferric reductases that convert Fe^{3+} to soluble Fe^{2+} [221], [222].

Previous transmission TEM analyses combined with X-ray absorption spectroscopy and Mössbauer spectroscopy studies revealed the presence of other iron species besides magnetite involved in early stages of magnetite biogenesis (e.g. ferrihydrite, ferritin proteins, hematite) [112], [121], [223]–[225]. This led to the hypothesis that 99% of the intracellular iron corresponded to magnetite as most of these distinct iron species were no longer detected in the intracellular iron pool by the end of the biomineralization process. However, recent studies demonstrated that magnetite constitutes only 25-45% of the total intracellular iron content [10], [119], [226], [227], evidencing the heterogeneity of the intracellular iron pool in MTB.

The use of single-cell analysis tools has yielded valuable information regarding the intracellular iron pool and magnetosome biomineralization [226]. For instance, fluorescence microscopy has been used to characterize intracellular iron speciation and subcellular localization [119], [228]; FCM to monitor physiological parameters, including the intracellular iron pool [18]; and single-cell ICP-MS to quantify the intracellular iron content of individual MTB cells [167]. Despite providing valuable information on the intracellular iron pool, these techniques are limited in their ability to measure magnetosome content at the single-cell level. In contrast, techniques that can quantify magnetosome content at the single-cell level (e.g. TEM) cannot measure the intracellular iron pool [169]. Therefore, using a combination of these techniques compensates for the limitations of each method. For example, FCM is a high-throughput technique that enables real-time single-cell analysis of thousands of cells within a brief timeframe, examines heterogeneous cell populations within a single sample, and provides

physiological information such as cell size and complexity [229]. However, FCM only provides relative measurements of cellular characteristics but lacks detailed morphological information compared to microscopic techniques. Bulk quantification of magnetosome content is typically done by ICP-OES or AAS and supported by TEM magnetosome visualization [230]. Both methods require offline measurements, impeding real-time data acquisition while performing the experiment, and involving tedious sample preparation procedures. TEM analysis typically involves sample drying, staining, and sectioning, potentially inducing sample damage and compromising the visualization of cells under their native conditions, which may influence the resultant data [231].

Here, we propose for the first time the utilization of a correlative microscopy approach involving cryoSIM and synchrotron-based cryoSXT [212] on *Magnetospirillum gryphiswaldense* MSR-1, alongside the use of FCM, ICP-OES, and TEM to enhance our understanding of this intracellular iron pool and its relationship with magnetosome synthesis at single-cell level under different oxygen and iron dosage regimes. CryoSIM was employed to obtain information on the labile Fe^{2+} intracellular pool, utilizing a fluorescent iron probe, and cryoSXT enabled the acquisition of structural cell information and the characterization of magnetosome content for each cell. Another important advantage of using a technique such as cryoSXT, where samples are cryo-fixed, is the preservation of their native-hydrated state, which is crucial for obtaining valuable structural and functional information. Although other correlative cryo-imaging techniques, such as the combination of cryo-fluorescence and cryo-electron microscopy, are widely used to study relevant cellular structures and dynamic processes such as bacteria-cell interactions [172], the resolution gap between visible light and electron microscopy can make data correlation challenging. CryoSXT therefore bridges the gap between these two techniques as a mesoscale imaging method, occupying this resolution gap and facilitating more effective data integration [201]. This combinatorial toolkit of quantitative and qualitative methodologies spans multiple scales, from population analysis and observation of physiological cell behaviours to elemental analysis and the examination of individual cells. The combined application of these techniques mitigates the inherent limitations through the strengths of the other complementary methods. This strategy has led to the acquisition of more robust datasets and yields valuable insights that might otherwise have gone unnoticed.

Overall, the use of this holistic multi-scale approach not only allows a deeper comprehension of the relationship between intracellular iron pools and magnetosome content at a single-cell level, but also enables the investigation of the effects of varying iron and oxygen concentrations on cellular growth, magnetosome synthesis and the formation of PHA granules.

3.2. Materials and methods

3.2.1. Strains, growth media and culture conditions

Magnetospirillum gryphiswaldense MSR-1 (DMSZ 6631) was grown in FSM, comprising 3.5 $g \cdot L^{-1}$ potassium L-Lactate, 0.1 $g \cdot L^{-1}$ KH_2PO_4, 0.15 $g \cdot L^{-1}$ $MgSO_4 \cdot 7H_2O$, 2.38 $g \cdot L^{-1}$ HEPES, 0.34 $g \cdot L^{-1}$ $NaNO_3$, 0.1 $g \cdot L^{-1}$ yeast extract, 3 $g \cdot L^{-1}$ soy bean peptone, 5 $mL \cdot L^{-1}$ EDTA-chelated trace elements solution (EDTA-TES) and 0 – 1 mM iron citrate ($C_6H_5FeO_7$). For all experiments, an iron-free modified version of EDTA-TES solution was employed, consisting of 5.2 $g \cdot L^{-1}$ EDTA disodium salt; 30 $mg \cdot L^{-1}$ H_3BO_3; 85.4 $mg \cdot L^{-1}$ $MnSO_4 \cdot H_2O$; 190 $mg \cdot L^{-1}$; $CoCl_2$ $g \cdot L^{-1}$; 4 $mg \cdot L^{-1}$ $NiCl_2 \cdot 6H_2O$; 2 $mg \cdot L^{-1}$ $CuCl_2 \cdot 2H_2O$; 44 $mg \cdot L^{-1}$ $ZnSO_4 \cdot 7H_2O$ and 36 $mg \cdot L^{-1}$ $Na_2MoO_4 \cdot 2H_2O$. The pH of FSM and EDTA-TES was adjusted to 7.0 and 6.5, respectively, with NaOH prior to autoclaving.

For the first experiment, aerobic and microaerobic MSR-1 cultures were grown under different iron citrate dosages (0 – 50 – 100 – 300 µM) to compare the effects caused by these environmental factors on magnetosome formation and the intracellular iron pool. An additional experiment investigating MSR-1 microaerobic growth under a broader range of iron citrate dosages (0 – 100 – 300 – 500 – 1000 µM) was conducted to further explore iron tolerance. Both experiments were performed in hungate-type tubes (16x125 mm, Chemglass Life Sciences) with working volumes of 10 mL. Each tube was inoculated at a 1:10 ratio, and samples were collected before the end of the exponential growth phase (approximately at 72h).

For the time course experiment in which the evolution of the intracellular iron pool and magnetosome formation was monitored over time, 100 mL DURAN® bottles with working volumes of 40 mL were used. To study the time-dependent evolution of magnetosome formation, non-magnetic MSR-1 cells were used to inoculate aerobic and microaerobic cultures supplemented with 100 µM iron citrate at an initial OD_{565} of 0.1. Samples were then collected at various time points (0, 4, 8, 24, 28h).

All MSR-1 cultures were grown in triplicate at 30 °C in an Incu-Shake MAXI® (SciQuip Ltd, Newtown, UK) orbital shaker incubator operated at 150 rpm. To create microaerobic conditions, both bottles and hungate tubes were purged with N_2 for 10-30 min to remove all the dissolved O_2 and sealed with bromobutyl rubber stoppers. Subsequently, the necessary volume of sterile air was injected to achieve an oxygen concentration of 1%.

3.2.2. Bacterial growth and magnetic cellular response

Bacterial growth was determined by measuring the optical density of cultures in an Evolution 300 UV-Vis spectrophotometer (Thermo Fisher Scientific, Hemel Hempstead, Herts, UK) at a wavelength of 565 nm (OD_{565}). Cellular magnetic response (C_{mag}) was measured as described elsewhere immediately after obtaining the OD_{565} values [18]. Briefly, the spectrophotometer was equipped with two pairs of Helmholtz coils positioned around the cuvette holder — one pair perpendicular to the light beam and the other one parallel. The OD_{565} values were measured under each condition. In the presence of magnetic cells, the alignment with the two orientations leads to different optical densities, while non-magnetic cells will not be affected by the switch of the magnetic field, resulting in no change in optical density. C_{mag} values were calculated by dividing the OD_{565} values for cells aligned parallel and perpendicular to the light beam. C_{mag} values range from 1 to 3, with a value greater than 1 indicating the presence of magnetic cells.

3.2.3. Flow cytometry

Bacterial samples were collected from the liquid cultures, diluted in phosphate-buffered saline solution (PBS), and directly analysed in a BD Accuri C6 flow cytometer (Becton, Dickinson and Company, Oxford, UK). FCM was used to determine relative cell size (FSC-A), cell granularity/complexity (SSC-A), intracellular iron concentration and PHA formation. The intracellular iron concentration was detected using the Phen Green™ SK fluorophore (PG-SK), and PHA granules were stained with Pyrromethene-546 (Pyr-546). Details of the fluorescent probe staining conditions are provided in **Chapter 4** (**section 4.2.3**). Fluorescent labelled cells were excited using a 488 nm solid-state laser and fluorescence was detected using a 533/30 BP filter (FL1-A).

3.2.4. Determination of iron content

The intracellular and extracellular iron concentrations of MSR-1 cultures were analysed using ICP-OES (Thermo Scientific iCAP 7000) as an offline analysis. The iron concentration was determined at a wavelength of 259.94 nm. One mL of the sample was collected and centrifuged to separate cells from the culture media. The supernatant was acidified by adding 10 µL of 70% (v/v) nitric acid prior to analysis. Cell pellets were first washed using PBS to remove iron traces from the media and subsequently digested with nitric acid (70% v/v) at 98°C for 2h with shaking at 300 rpm in a Thermo Mixer HC (Starlab, Blakelands, UK) prior to analysis. All values obtained were then normalized using the dry cell weight (DCW) to avoid discrepancies due to different cell biomass.

3.2.5. Transmission electron microscopy

Transmission electron microscopy images of magnetic MSR-1 cells grown under various iron dosages (0 – 100 – 300 – 500 – 1000 µM iron citrate) were captured using a JEOL 2100F FEG microscope (JEOL, Herts, UK) operated at 200 kV and equipped with a Gatan K3 IS camera. MSR-1 cells (2 µL) were deposited on a lacey carbon 300 mesh copper supported grid (GOLC300Cu50, EM Resolutions, Sheffield, UK) and vacuum-dried before analysis. To determine the mean length of the magnetosome chains, 100 cells were randomly selected for each condition, and the number of magnetosome crystals per chain was counted. Statistical analysis was conducted using one-way analyses of variance (ANOVA) followed by Bonferroni's post-test to compare the effect of the different iron dosages on the magnetosome chain length. The cut-off value for statistical significance was set at $p < 0.01$.

3.2.6. CryoSIM and CryoSXT correlative microscopy collection and analysis

Vitrification of samples was done at Diamond Light Source synchrotron at beamline B24 (**Figure A1**). Grids (QUANTIFOIL® R 2/2 Au G200F1) were glow discharged before sample deposition using a PELCO easiGlowTM system. Before plunge freezing, samples were incubated with either PG-SK (1 mM – 5 min incubation) or Pyr-546 (0.1 $mg \cdot mL^{-1}$) at room temperature. The grid was then mounted in the plunging apparatus (Leica EM GP) and 2-4 µL of sample was deposited on top of the carbon surface of the grid. Before fiducial deposition, manual blotting from behind was performed using Whatman® filter paper. Once fiducials were deposited (2 µL of either 150 nm or 250 nm gold nanoparticles), the sample was automatically blotted from behind (on one side) for 0.5 – 1 s at room temperature in an environmentally controlled chamber at 70% humidity. Vitrification was achieved by rapidly plunging the grid into liquid ethane maintained at −170 °C. Finally, the grids were stored in liquid nitrogen until further analysis. Three replicates were prepared for each experimental condition.

Vitrified samples were loaded in a Linkam cryostage coupled to the cryoSIM microscope at beamline B24 for SIM data collection [212]. To identify regions of interest (ROIs), each grid was mapped by acquiring 2D brightfield transmission mosaics. Once ROIs were annotated, brightfield and SIM 3D data were collected along the z-axis. PG-SK and Pyr-546 fluorescence data were collected using a green laser (488 nm wavelength) for 40 ms (exposure time) at 50 mW of power. Fluorescence was collected through a 525 nm filter on a CCD camera.

For cryoSXT data collection, the vitrified samples were transferred to the UltraXRM-S/L220c transmission soft X-ray microscope (Carl Zeiss) at beamline B24. Grids were firstly visualised using an inline visible-light 20x objective to identify previously annotated ROIs. For cryoSXT collection, the

transmitted light was focused using a 25 nm zone plate (X-ray objective), resulting in a 10 x 10 µm field of view. 2D X-ray mosaics of ROIs were captured to identify interesting areas for tomography collection. Tilt series were collected using an incident beam of 500 eV ('Water Window') or 710 eV (Fe L_3-edge) at tilt angles from -60° to +60° with a step size of 0.5° and an exposure time of 0.5 s per frame.

After tilt series were acquired, tomograms were reconstructed either manually using IMOD© (University of Colorado) [232] or by an automated pipeline based on IMOD (batchruntomo) using a simultaneous iterative reconstruction technique. To correlate both cryoSTX and cryoSIM data sets, eC-CLEM software was employed [233], [234]. To measure individual cell PG-SK fluorescence intensity, Fiji (ImageJ) software was used. SuRVos2 Workbench [235] was used to segment cellular features such as the magnetosome chain, PHA granules or the cellular membrane and the 3D volume render was visualized using UCSF ChimeraX [236].

3.3. Results and discussion

3.3.1. Effect of iron and oxygen availability on MSR-1 growth and magnetosome biogenesis

Given the key roles that iron and oxygen play in magnetosome biomineralization [33], MSR-1 was grown under different oxygen and iron conditions. Samples were then collected at the end of the exponential growth phase for each condition and analysed.

The effect of oxygen on MSR-1 growth is depicted in **Figure 3.1A** and **Figure 3.1C**. As can be observed, there is a growth reduction in microaerobic (low oxygen) compared to aerobic conditions. This observation is in line with previously reported data [33]. In all known MTB, when oxygen is abundant, magnetite formation is suppressed, allowing the bacteria to allocate more energy towards cell growth and aerobic respiration [11]. For instance, it has been demonstrated that genes related to nutrient transport and physiological metabolism are down-regulated under microaerobic conditions as energy is redirected for magnetosome synthesis [129].

As for the iron concentration effect on cell growth, several observations were noted. First, the absence of iron in the media hinders cell growth, as evidenced in **Figure 3.1A** and **Figure 3.1F** [126]. A significant decrease in the cellular growth of MTB is not surprising given that iron is a key player in many biological reactions and metabolic pathways [109]. Importantly, aerobic cell growth was shown to be more significantly affected by the absence of iron than microaerobic cultures, given that a complete lack of growth was observed for this condition. This trend has been consistently observed when utilizing an EDTA-TES iron-free solution for aerobic cultures in preliminary experiments (data not presented). Secondly, the increase of iron citrate dosage did not exhibit any detrimental impact on cellular growth up to 300 µM (**Figure 3.1A**). Despite literature suggesting that iron toxicity for MSR-1 is set at concentrations exceeding 200 µM, [126], [127] such effects were not observed in our experimental set

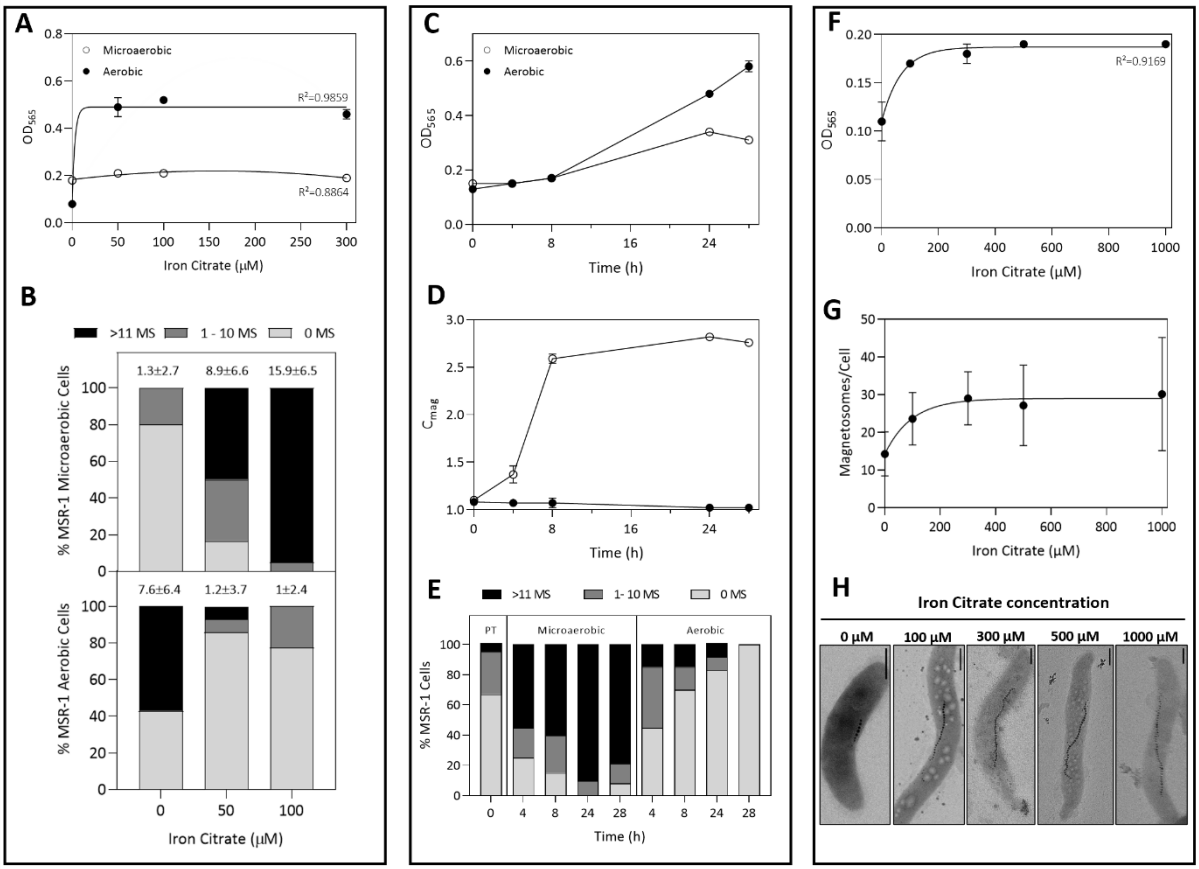

Figure 3.1. Effect of iron and oxygen availability on MSR-1 cell growth and magnetosome synthesis. (A-B) MSR-1 cells were grown under different iron dosages (0-50-100-300 µM iron citrate) either under microaerobic or aerobic conditions. (C-E) Time-course experiment in which MSR-1 cells were grown at 100 µM iron citrate under microaerobic or aerobic conditions over a period of 28h. (F-H) Iron tolerance test of MSR-1 cells grown under microaerobic conditions. The iron dosage range for this experiment was 0-100-300-500-1000 µM iron citrate. (A, C, F) Cell growth was monitored by measuring the optical density of the different cultures (OD_{565}). (D) Cellular magnetic response (C_{mag}) values obtained from time-course experiment. (B, E) Representation of magnetosome content of the two main correlative microscopy experiments ($n_{(B)}$= 102; $n_{(E)}$= 204). For each condition, magnetosome content was classified according to the magnetosome chain length: long chain (>11 MS), short chain (1 -10 MS) or no chain (0 MS). (G) Mean magnetosome chain length of iron tolerance test (n=500). (H) TEM images of iron tolerance test of MSR-1 cells. Error bars are standard deviation of triplicates. MS = magnetosomes; PT = Pre-transfer. Scale bar = 500 nm.

up. This discrepancy may be due to differences in experimental methodology, particularly the buffering capacity of the media. Consequently, a further experiment was conducted to assess MSR-1 iron tolerance. The results of this complementary experiment (**Figure 3.1F**) showed that cell growth remained unaffected even with an increase of iron concentration up to 1 mM. This observation, along with previous findings in MSR-1 fermentation experiments [11], [146], supports our hypothesis that MSR-1 endures greater iron tolerance than initially presumed. This suggests the existence of robust iron regulatory mechanisms (that remain poorly understood), such as iron deposition into bacterioferritins [121] and molecular processes that prevent the accumulation of ROS [38].

The number of magnetosomes per cell for each iron and oxygen condition was determined using cryoSXT (**Figure 3.1B**). Due to the resolution limitations of this technique, only magnetosomes containing magnetite crystals, and not empty magnetosome vesicles, can be detected. Therefore, from this point forward, any reference to the number of magnetosomes pertains exclusively to those containing a magnetite crystal. It should be noted that, unfortunately, grids corresponding to the 300 µM conditions have not be screened by cryoSXT due to time constraints. Magnetosome chains from all other conditions successfully screened by cryoSXT were then classified as short or long, depending on whether they contain less than or more than 10 magnetite crystals, respectively. Based on our analysis, microaerobic cells grown under a low iron concentration (50 µM) exhibited shorter chains and a more heterogeneous chain length distribution, as only 50% were considered long. In contrast, 95% of cells grown at a higher iron dosage (100 µM) presented long chains (**Movie 3.1**), reflecting a more homogeneous chain length distribution. These results suggest that higher extracellular iron concentrations may lead to the production of longer magnetosome chains. Nonetheless, iron tolerance test results (**Figure 3.1G**) showed that for iron citrate concentrations higher than 300 µM, magnetosome chains were not significantly longer (one-way ANOVA with Bonferroni test, $p < 0.01$). Other studies have reported that magnetosome yields do not improve when using iron citrate concentrations higher than 200 µM [127]. Around 80% of microaerobic cells grown without iron did not contain any magnetosome chain. However, some cells still had short magnetosome chains because of the presence of trace amounts of iron in the media carried over from pre-cultures (**Figure 3.1H** and **Movie 3.4**).

Although it is widely known that magnetite formation is suppressed under aerobic conditions [33], [126], some magnetosome production can still be observed under our experimental conditions. Since iron-starved aerobic cells did not grow, the amount of magnetosomes per cell (reflected in **Figure 3.1B**) corresponds to the initial presence of magnetic cells in the starting culture for this experiment. The presence of magnetite crystals in the 50 and 100 µM aerobic conditions can be attributed to the air transfer restriction caused by the use of sealed tubes with only 38% of headspace. As cell growth

progressed, the oxygen contained in the tubes was consumed, prompting cells to switch to microaerobic metabolism and activate magnetosome production. This increase in magnetosome formation due to oxygen depletion has been observed at both flask and bioreactor scales either by limiting the flask headspace volume [18] or ceasing bioreactor aeration [11], [219]. In line with recent findings by Pang *et al.*, oxygen depletion triggers denitrification pathways that allow for the generation of nitric oxide (NO), which is crucial for the expression of biomineralization genes. Under aerobic conditions, oxygen respiration may compete with nitrification/denitrification pathways and thereby impairing magnetite formation [130].

Due to the complexity of controlling oxygen limitation in tubes, a separate experiment was performed using 100 mL bottles where the headspace was larger (70%) and aerobic conditions could be prolonged over time. In this experiment, MSR-1 cells were grown using 100 µM iron citrate either under aerobic or microaerobic conditions. Then, parameters such as cell growth (**Figure 3.1C**), magnetic cellular response (C_{mag}) (**Figure 3.1D**) and magnetosome content (**Figure 3.1E**) were monitored over time. To facilitate the monitoring of magnetosome biomineralization from its onset, a low-magnetic pre-culture was used (C_{mag} = 1.1). Both C_{mag} values (**Figure 3.1D**) and magnetosome content (**Figure 3.1E**) clearly show that magnetosome production increased for cells under microaerobic conditions and reduced to C_{mag} ~ 1 for cells exposed to aerobic conditions. The peak of magnetosome production in microaerobic cultures occurred at the end of the exponential phase as previously observed by others [11], [219]. Magnetosome content in aerobic cells was roughly halved at every sampling time point. During MSR-1 cell division, the magnetosome chain is cleaved into two and each fragment passed onto a daughter cell [237]. Therefore, the magnetosome chains present in the magnetic cells of the starting culture did not disappear immediately after continuous exposure to air. As cells divide, the chains are split and become shorter until cells are depleted of magnetosomes.

3.3.2. Effect of iron and oxygen availability on the intracellular iron pool

While magnetosomes were previously considered to account for nearly all intracellular iron content [49], more recent studies suggest that a substantial portion remains in other intracellular iron pools [10], [119]. The remaining iron is used in general iron-dependent biochemical reactions [112], [227] or deposited in iron-storing proteins such as bacterioferritins to prevent toxicity [121]. The existence of these different intracellular iron pools adds more complexity and difficulty in elucidating the relationship between the intracellular iron pool and magnetosome formation. To this end, an

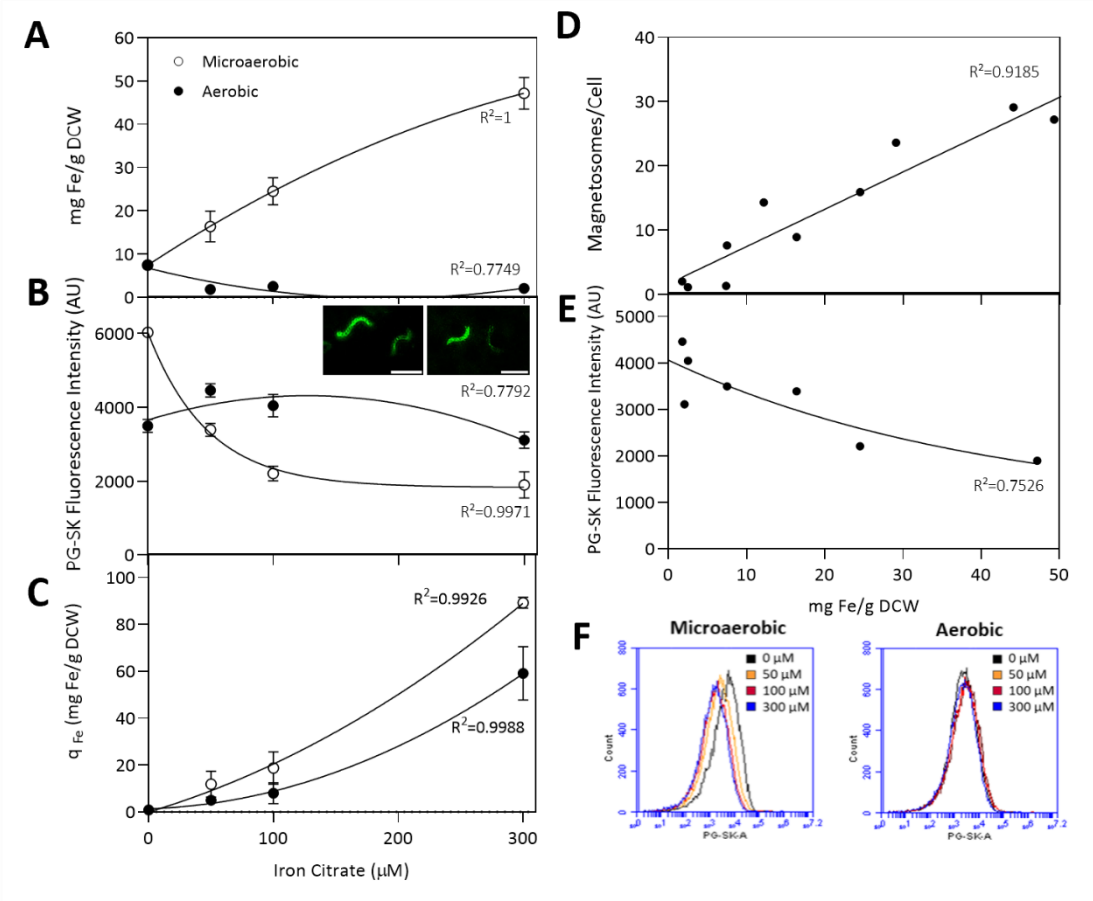

Figure 3.2. Effects of iron concentration and oxygen availability on the intracellular iron pool of MSR-1 cells grown under different iron dosages (0-50-100-300 µM iron citrate) under microaerobic and aerobic conditions. (A) Total intracellular iron concentration normalized to biomass (DCW=dry cell weight). Error bars represent standard deviation of triplicates. (B) PG-SK fluorescence intensity values obtained from flow cytometry (FCM) analysis. A total of 25,000 events were analysed per sample by FCM; Error bars show covariance. Insets images show cryoSIM images of MSR-1 cells stained with PG-SK (scale bar = 2 µm). (C) q_{Fe} iron uptake rates. (D) Correlation between the total intracellular iron concentration and magnetosome units per cell. (E) Correlation between the total intracellular iron concentration and PG-SK fluorescence intensity from FCM. (F) PG-SK fluorescence histograms from FCM analysis. AU = arbitrary units; FCM = Flow Cytometry.

innovative multipronged approach involving different techniques was combined to obtain a holistic view of the effects of the extracellular iron concentration of magnetic and non-magnetic MSR-1 cells on the intracellular iron pool and how this correlates with magnetosome formation.

Quantification of the total amount of intracellular iron was done by ICP-OES, whereas FCM was used to assess the labile Fe^{2+} intracellular pool by using PG-SK fluorescence probe. PG-SK is a chelatable fluorophore that has high affinity for Fe^{2+} and is quenched when it binds to it. PG-SK has been a useful tool for the detection of the intracellular iron pool in MSR-1 [18], [228], as well as in other eukaryotes [238] and bacteria [239].

The quantitative estimation of the total amount of iron in MSR-1 cells grown under microaerobic conditions (**Figure 3.2A**) revealed a clear correlation between the intracellular iron pool and the

supplemented iron from the growth media. This indicates that an increase in extracellular iron leads to a corresponding increase in intracellular iron concentration. However, it was found that under conditions where the initial iron levels in the media exceeded 300 µM, a plateau was reached, and the intracellular iron concentrations remained unchanged despite further increases in iron supplementation (**Figure A2**). Similar results have also been observed for the AMB-1 strain grown under different iron dosages [167]. Notably, our measurements of q_{Fe} iron uptake rates (**Figure 3.2C**) demonstrates a correlation with the extracellular iron concentration, indicating that MSR-1 enhances its iron uptake capacity as more iron becomes available in the environment, most likely by active transport mechanisms such as ABC or FeoB membrane proteins [240]. Amor *et al.* reported that iron incorporation in the phylogenetically close strain AMB-1 was 10-fold higher under high iron conditions (150 µM) compared to low iron conditions (30 µM) [119]. In contrast, under aerobic conditions, intracellular iron concentrations were notably lower compared to those observed under microaerobic conditions and remained stable despite increases in the initial iron concentration in the media (**Figure 3.2A**). As mentioned in the previous section, the depletion of oxygen in the tube headspace leads to a metabolic shift from aerobic to microaerobic metabolism. This explains why we observed a similar trend in aerobic q_{Fe} iron uptake rates, but with lower values and a less steep fitting slope. For all the graphs with fitted lines (R^2 value provided), it is important to note that the lines represent best fits used solely to display trends, and not to provide physical or mathematical interpretation. This approach applies to all fitted graphs presented in the thesis, where the fittings are included only for visualizing trends rather than offering specific physical or mathematical significance

Additionally, a clear linear correlation was observed between magnetosome content and intracellular iron concentration (**Figure 3.2D**). Specifically, as the length of magnetosome chains increased, there was a corresponding increase in the concentration of the total intracellular iron.

Upon examination of the intracellular labile Fe^{2+} pool using FCM, aerobic PG-SK fluorescence values were higher than in microaerobic conditions (**Figure 3.2B** and **Figure A3**). Considering that PG-SK quenches upon Fe^{2+} bonding, the decrease of green fluorescence is proportional to the size of the labile Fe^{2+} pool. Similar to the findings observed in the total iron concentration (**Figure 3.2A**), an indirect positive correlation was found in microaerobic conditions between the initial iron dosage in the media and the corresponding intracellular Fe^{2+} concentrations, in which the increase of the initial iron dosages caused the increase of the intracellular Fe^{2+} levels. Despite Fe^{3+} (iron citrate) being the only source of iron provided in the media, it has been proven that MSR-1 employs ferric reductases to convert Fe^{3+} to Fe^{2+} [221], [222] and uses general iron uptake systems such as Feo system to incorporate ferrous iron [117], [220]. Gene expression studies during cell growth and magnetosome synthesis revealed that under high-iron conditions, ferric reductase genes, ferrous transport system-related

genes, and ROS scavenging related genes are highly expressed whereas under poor iron conditions only iron transport-related genes are expressed [241]. This enhanced expression of ROS scavenging-related genes might be the key to understanding how MTB are able to uptake such high amounts of iron or live within these excessive iron concentrations.

Comparison of ICP-OES and FCM data reveal an inverse correlation between the total iron concentration and PG-SK fluorescence values (**Figure 3.2E**). Due to the quenching nature of PG-SK upon iron binding, this inverse correlation implies an actual direct relationship with Fe^{2+} concentration. Fluorescence intensity histograms (**Figure 3.2F**) also reflected the distinct variations in PG-SK fluorescence in microaerobic conditions with respect to the non-variant fluorescence profiles of the aerobic conditions. While all conditions displayed a unimodal distribution, the broadness of the peaks indicated significant variability in fluorescence intensity among cells within the same sample. This suggests a degree of heterogeneity in fluorescence across the population, which was further confirmed by fluorescence microscopy observations (**Figure 3.2B** insets). FCM population analysis (**Figure A4**) indicated that this variability in fluorescence could be attributed to the presence of two distinct cell populations. The first population was comprised of smaller cells with elevated intracellular Fe^{2+} levels, while the second consisted of larger cells with diminished intracellular iron concentrations. This pattern was consistent across all experimental growth conditions.

Based on the findings, cells with higher intracellular labile Fe^{2+} concentrations are likely to possess a higher number of magnetosomes compared to those with lower iron levels. Despite the evidence provided by ICP-OES and FCM data, this hypothesis could not be verified. Therefore, to corroborate this hypothesis, we performed, for the first time in MTB, a single-cell analysis using a synchrotron-based correlative microscopy approach involving cryoSXT and cryoSIM [212]. CryoSXT enabled direct visualization and characterization of magnetite formation, while cryoSIM was employed to indirectly examine the intracellular distribution of iron by locating its chemical signals of PG-SK-stained cells.

MSR-1 cells grown under varying iron and oxygen regimes were vitrified and screened by cryoSXT and cryoSIM at beamline B24 at the UK synchrotron, Diamond Light Source. However, preliminary correlative data was also acquired at MISTRAL beamline at ALBA synchrotron facilities (**Figure A5**) that significantly contributed to the success of our subsequent experiments at Diamond. Within the soft X-rays spectrum (0.1-1 keV), it is feasible to distinguish elements based on their absorption properties. There is a particular spectral region known as the "water window" located between the absorption edges of carbon (284 eV) and oxygen (543 eV) that is especially advantageous for visualizing biological specimens because carbon- and nitrogen-rich components absorb X-rays strongly, compared to the oxygen-rich media that surround them, without the need to add any contrast staining reagents [176].

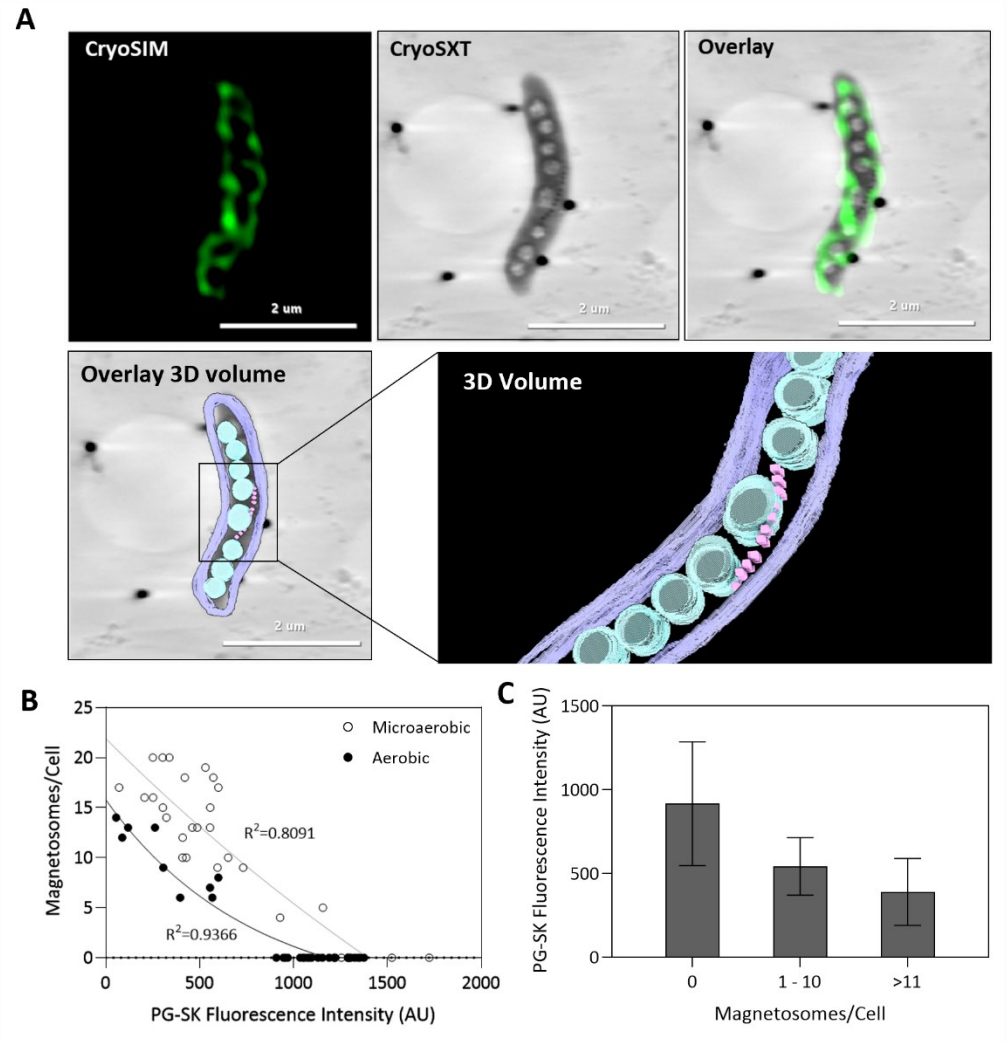

Figure 3.3. (A) Representative tomogram slices of MSR-1 magnetosome-producing cell grown under microaerobic conditions imaged by cryoSIM and cryoSXT, including a 3D volumetric representation of this cell using SuRVos2 workbench. Magnetosomes are coloured in pink, PHA granules in blue and the cell membrane in purple. (B) Single-cell correlation between cryoSIM PG-SK fluorescence and number of magnetosome crystals per cell of microaerobic and aerobic MSR-1 cells (n=63). (C) Mean cryoSIM PG-SK fluorescence values of MSR-1 cells with no magnetosomes, short magnetosomes chains (1-10) and long magnetosome chains (>11) (n = 104). AU = arbitrary units; CryoSIM = Cryo-structured illumination microscopy; CryoSXT = Cryo-soft X-ray tomography.

X-ray tomographs of MSR-1 imaged at the "water window" (500-510 eV) were acquired alongside 3D cryoSIM data from the same cells (**Figure 3.3A** and **Movie 3.2**). PG-SK green fluorescence was homogeneously distributed in the cytoplasm except in regions containing PHA granules that remained unstained. For each individual cell, the number of magnetosomes was counted and PG-SK fluorescence intensity measured using the Fiji imaging software. The corresponding single-cell correlation data is shown in **Figure 3.3B**. Cells with a higher count of magnetosomes displayed lower levels of PG-SK fluorescence, indicating elevated intracellular Fe^{2+} iron concentrations. Inversely, a decrease in the number of magnetosomes per cell caused a reduction in the intracellular Fe^{2+} pool under both

microaerobic and aerobic conditions. However, it is important to note that in the aerobic condition, cells likely entered a microaerobic state during growth due to oxygen consumption and limited oxygen exchange in the hungate tubes. This transition may have influenced the intracellular iron concentrations observed in the aerobic samples. The number of magnetosomes per cell and their correlation with PG-SK fluorescence values was consistent whether PG-SK fluorescence was obtained via flow cytometry (**Figure A6**) or from cryoSIM data (**Figure 3.3B**), as similar trends were observed.

Moreover, when cells were analysed solely based on the length of the magnetosome chain, regardless of the different growth conditions, significant differences were observed (one-way ANOVA with Bonferroni test, $p < 0.01$) with regards to the PG-SK fluorescence intensities among cells classed as "no" (zero), "long" (> 11), or "short" (1 – 10) magnetosome chain length (**Figure 3.3C**). Cells with long magnetosome chains exhibited the highest intracellular Fe^{2+} iron concentrations, while those without presented the lowest Fe^{2+} levels. Notably, 85% of cells with long magnetosome chains were grown under microaerobic conditions, whereas 65% of magnetosome-lacking cells were grown aerobically (**Figure A7**). Cells with short magnetosome chains had a more balanced distribution between cells grown under microaerobic (56%) or aerobic conditions (44%). To the best of our knowledge, this level of analyses has not been performed before this work, hence, we provide new insights into the elucidation of iron uptake dynamics and its correlation with magnetosome formation in MSR-1.

3.3.3. Evolution of the intracellular iron pool during biomineralization

In the previous section, the focus was on the impact of iron and oxygen availability on the intracellular iron pool and magnetosome formation. MSR-1 cells were harvested at the end of their exponential growth phase, when magnetosome chain length is typically maximal in their cell cycle [219]. To further explore the relationship between the intracellular iron pool and magnetosome formation, we conducted a time-course study aiming to monitor the changes in the intracellular iron pool as magnetosome chains form in time. MSR-1 cells were grown under identical initial iron citrate conditions (100 μM) under microaerobic and aerobic conditions. Samples were subsequently taken at several time points and analysed using the same analytical and correlative microscopy techniques employed in the preceding experiment.

Figure 3.4A illustrates the magnetosome biomineralization process over time. Visual inspection of the cryoSIM images (bottom row) revealed a striking decrease in PG-SK fluorescence as magnetosome chains elongated under microaerobic conditions. It was also observed that some of the cells containing

the longest chains barely exhibited any fluorescence, indicating a potential substantial accumulation of Fe^{2+}. Contrary to what Amor *et al.* observed when using another ferrous fluorescent probe (FIP-1) [119], we did not observe localized fluorescence. They reported Fe^{2+} accumulation around the magnetosome chain and at the cell poles during cell division. However, due to the quenching properties of the PG-SK fluorophore, we were unable to quantify any localization. Our observations were limited to the turn-off nature of the fluorophore when quenched by Fe^{2+}.

One advantage of using soft X-rays for imaging cellular structures is the ability to visualize different elements depending on the chosen X-ray energy within the spectrum [242]. In this experiment, in addition to imaging at an energy within the "water window" (**Figure 3.4A** – top row), where water is transparent and carbon absorbs X-rays heavily thus generating contrast, we also imaged our samples by changing the energy of the transmission X-ray microscope at beamline B24 to the Fe L_3 absorption edge (**Figure 3.4A** – middle row). Magnetosomes presented higher contrast at the Fe L_3 absorption edge (circa 710 eV), making them more discernible compared to the "water window" (**Movie 3.3** *versus* **Movie 3.4**), as iron-rich elements selectively absorbed X-rays at this energy [205]. Additionally,

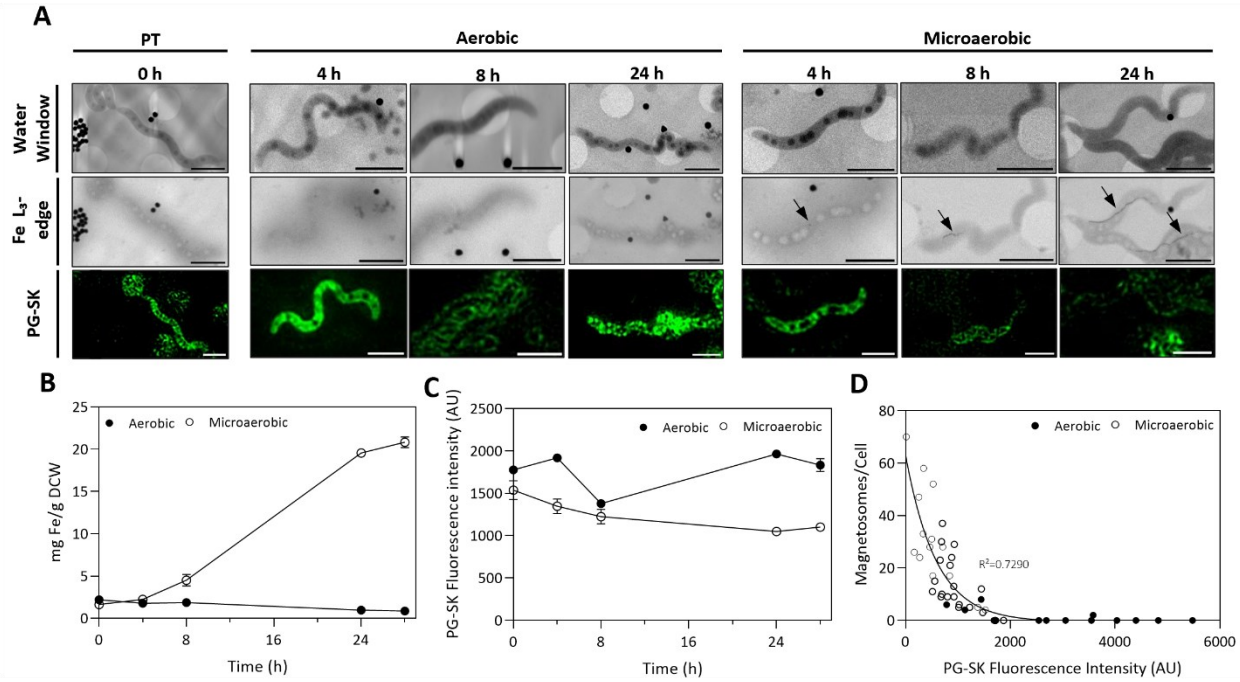

Figure 3.4. (A) Representation of magnetosome biomineralization evolution illustrated by cryoSXT and cryoSIM images of MSR-1 cells grown under microaerobic or aerobic conditions over a period of 24h. Two different photonic energies were employed for cryoSXT acquisition: 500 eV (top row) and 710 eV (middle row). MSR-1 cells were stained with a PG-SK fluorescent probe before cryoSIM data acquisition. Arrows indicate the presence of magnetosome chains. Evolution of (B) the total intracellular iron concentrations and (C) PG-SK mean fluorescence intensity values (FCM) of MSR-1 cells grown with 100 µM iron citrate under microaerobic or aerobic conditions. (D) Single-cell correlation between PG-SK fluorescence (cryoSIM) and number of magnetosome crystals per cell of microaerobic and aerobic MSR-1 cells grown under 100 µM iron citrate (n = 62). Error bars indicate standard deviation (n = 3). A total of 25 000 events were analysed per sample by FCM. Scale bar = 2 µm. PT = Pre-transfer. AU= arbitrary units; CryoSIM = Cryo-structured illumination microscopy; CryoSXT = Cryo-soft X-ray tomography; FCM = Flow Cytometry.

microaerobic cells appeared darker overtime at the Fe L_3 edge (**Figure 3.4A** – middle row), indicating an increase in cellular iron content during magnetosome formation. This increased dark contrast due to iron accumulation in the cytoplasm, also enhanced the visibility of cell structures such as PHA granules or cell membranes by the end of the biomineralization process. In contrast, as aerobic cells exhibited low intracellular iron content, the cytoplasm had less contrast and cells appeared less defined, which challenged the visualization of cell structural details compared to microaerobic cells.

Total intracellular iron concentration results (**Figure 3.4B**) determined by ICP-OES confirmed the variance in iron content observed between microaerobic and aerobic conditions already evidenced in the Fe L_3-edge data. Results shown in **Figure 3.4B** are consistent with C_{mag} results (**Figure 3.1D**). In both graphs, it is apparent that the start of iron accumulation occurred at the beginning of the exponential growth phase (t = 8h), a period in which magnetosome production started to be significant, while the iron concentration and C_{mag} values under aerobic conditions remained at consistent low levels throughout the duration of the experiment, as biomineralization is inhibited in the presence of oxygen [33].

Time-course PG-SK fluorescence intensity results obtained by FCM (**Figure 3.4C**) were consistent with cryoSIM fluorescence measurements (**Figure A8**). Microaerobic cells exhibited a 1.5-fold decrease in green fluorescence, indicating an increase in Fe^{2+}. This modest increase in labile Fe^{2+} concentration compared to the 9-fold increase observed in the total amount of intracellular iron (**Figure 3.4B**) suggests that labile Fe^{2+} is not the only form of iron present at the end of the biomineralization process distinct from magnetite. As reported by Amor *et al.* and Berny *et al.* in separate studies, only 25 - 45% of the total intracellular iron corresponds to magnetite [118], [119] and this study supports this hypothesis. The other suggested iron species constituting the intracellular iron pool, aside from magnetite, are likely to be associated with proteins that contain heme-binding domains [243] or iron storage proteins, such as bacterioferritins [112], [121]. Nevertheless, further analytical and spectroscopic studies (e.g. STXM) are required to identify the presence of these compounds during biomineralization to verify this hypothesis. The identification of all iron-uptake and regulation mechanisms involved in magnetosome synthesis can also enhance our comprehension of the composition of the intracellular iron pool and the specific roles each component plays in the biomineralization process. Evidence indicates that general iron uptake systems participate in transporting iron into the intracellular space [244]. However, it has been suggested that an additional iron uptake pathway specific to biomineralization may exist. The variability of different general iron uptake mechanisms and homeostasis systems among MTB species supports this hypothesis. For instance, siderophore synthesis has been reported for AMB-1, MV-1, and MS-1 strains, but not for MSR-1 [114]–[116]. To further support this hypothesis, suppression of FeoB1 ferrous iron transporter

[117] or ferritin expression in MSR-1 [43], [121], led to reduced, but not completely supressed, biomineralization, suggesting the existence of additional, yet unidentified, iron uptake mechanisms. **Figure 3.4D** shows the correlation between the number of magnetosomes per cell and PG-SK intensity values at the single-cell level. This correlation was comparable to that observed between magnetosomes per cell and PG-SK intensity values obtained using FCM (**Figure A9**). Additionally, the relationship between magnetosome content and PG-SK fluorescence is consistent to the one observed in the previous correlative microscopy experiment shown on **Figure 3.3B**. Cells with a greater number of magnetosomes per cell displayed lower green fluorescence, indicating higher concentrations of Fe^{2+} compared to the cells with fewer magnetosomes. However, it is worth noting that other non-producing magnetosome cells followed a different correlation pattern. Such cells displayed the highest fluorescence values, but as shown in **Figure 3.4D**, some of these cells exhibited three times more fluorescence than other non-producing magnetosome cells. This observed increase in fluorescence only occurs from 24 h onwards and it further highlights the variability in fluorescence among the cell population [11], [18].

Among the various models proposed for MTB iron uptake, our results discarded the possibility of direct iron transport into the magnetosome vesicle lumen during membrane invagination, as no iron localization was detected in those areas prior to magnetite synthesis [5]. Instead, our findings align with MTB iron uptake models suggesting that iron is first accumulated in the cytoplasm before being transported to the magnetosome vesicles [112], [117], [227]. Earlier studies on magnetosome biomineralization primarily involved bulk spectroscopic characterization and assumed that the iron species, other than magnetite, that were detected during the early stages of magnetosome formation (e.g., ferritin, hematite) did not persist until the end of the biomineralization process [112], [223]–[225]. These analyses conducted using cells in bulk rather than single-cell analysis, likely resulted in the magnetite signal overshadowing other iron species present in the cells, making it difficult to detect these additional signals. Hence, this emphasizes the significance and merit of employing single-cell analysis. Chevrier *et al.* also observed a significant presence of intracellular iron species different from magnetite in MSR-1 cells during biomineralization through single-cell analysis using nano-X-ray fluorescence mapping and nano-X-ray absorption near-edge structure analysis (nano-XANES) [226]. Consistent with our results, the authors also observed that the intracellular iron pool does not deplete after the synthesis of magnetosome chains. While nano-XANES is effective for chemical identification of iron species, its time-consuming nature limits the number of cells that can be analysed, making it challenging to obtain statistically significant data. Additionally, the process of drying cells prior to analysis means that the observations may not fully represent their native conditions. In contrast, our study utilized cryo-preservation to maintain samples in a fully hydrated near-native state, allowing for

observations that more accurately reflect physiological conditions within MSR-1 cells. Furthermore, the efficiency of our approach enabled the screening of a larger number of cells at the single-cell level. The use of a fluorophore specific for Fe^{2+} also provided qualitative iron speciation under near-native conditions, offering additional insights into the cellular processes.

3.3.4. Effect of iron dosage and oxygen regime on PHA formation

It is widely known that PHAs are intracellular inclusions synthesized under conditions of carbon excess, nutrient limitation, or environmental stress [142]. Although extensive research has been conducted on PHA synthesis in various microorganisms, studies focusing on PHA production in MTB remain limited. Here, the fluorescent probe Pyr-546, which stains PHA granules green, was used to assess PHA content by FCM. Pyr-546 dye is a commonly used probe to detect PHA granules [245] and has previously been used in studies involving MSR-1 [11], [18].

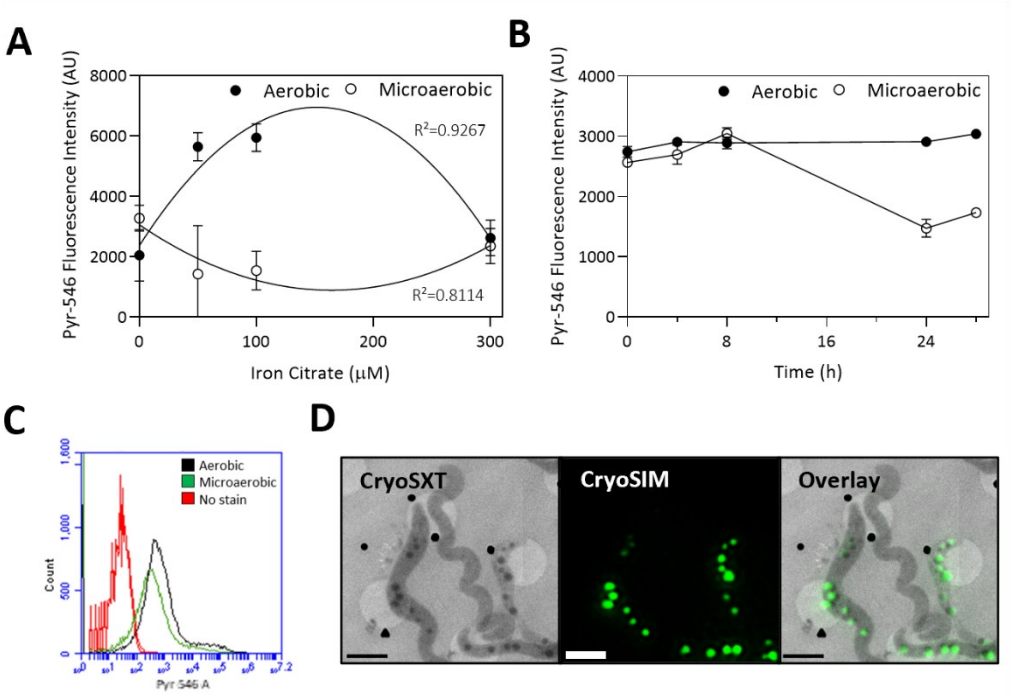

Figure 3.5. Analysis of the effect of iron and oxygen availability on PHA formation using FCM. (A) Comparison of Pyr-546 fluorescence values of MSR-1 cells grown under different iron dosages (0-50-100-300 µM iron citrate) under microaerobic or aerobic conditions. Errors bars indicate covariance. A total of 25 000 events were analysed per sample by FCM. (B) Evolution of Pyr-546 fluorescence values between microaerobic or aerobic MSR-1 cells grown with 100 µM iron citrate over a period of 28h. Error bars are standard deviation. (C) Comparison between fluorescence intensity histograms of microaerobic and aerobic MSR-1 cells stained with Pyr-546. (D) CryoSXT and cryoSIM images of MSR-1 cells stained with Pyr-546. Scale bar = 2 µm. AU = arbitrary units; CryoSIM = Cryo-structured illumination microscopy; CryoSXT = Cryo-soft X-ray tomography; Pyr-546 = Pyrromethene-546. FCM = Flow Cytometry.

Our results indicate that aerobic conditions favour PHA formation in MSR-1 cells over microaerobic conditions, independent of the initial iron concentration in the media (**Figure 3.5A** and **Figure 3.5B**). Su *et al.* studied the effects of aerobic and anaerobic conditions on PHA production in AMB-1 strain and observed a reduction in PHA content when switching to anaerobic conditions, and an increase when switching to aerobic conditions [144]. Notably, the absence of iron led to the highest PHA content under oxygen-limited conditions (**Figure 3.5A** and **Figure A10**), suggesting that iron limitation may induce stress responses that promote PHA synthesis as a carbon storage mechanism. Previous work in the group also observed higher Pyr-546 fluorescence values in MSR-1 cells grown in the absence of iron compared to cells grown with iron [18]. Interestingly, iron did not accumulate in or around PHA granules (**Figure 3.4A** – middle row) and the additional stress of being grown under high iron concentrations did not cause an increase in PHA content (**Figure A10**). These results suggest that oxygen may play a more important role in PHA synthesis and regulation than other stress factors such as high iron concentration.

The evolution of PHA content over time when comparing aerobic and microaerobic conditions (**Figure 3.5B**) is highly relevant and enables to understand the relationship between PHA and magnetosome synthesis. Previous studies have suggested the existence of an energy competition between magnetosome and PHA formation [11], [13], [18], [144]. When PHA synthesis was suppressed by genetic modification, magnetosome production was increased [145]. Our results also reflect this competitive relationship. As shown in **Figure 3.5B**, PHA formation was reduced when significant magnetosome production started (t = 8h), while under conditions inhibiting magnetosome synthesis (aerobic cultures), PHA content remained stable over time.

Pyr-546 fluorescence histograms (**Figure 3.5C**) reveal heterogeneity in PHA content. A prominent peak is observed accompanied by a smaller peak or tail, which indicates the presence of a sub-population with significantly higher PHA levels. Such variability, has been observed in other studies carried out with MSR-1 [18] as well as in other bacterial species [246], [247]. **Figure 3.5D** shows evidence of this variability in PHA content among cells grown under the same conditions. Karmann *et al.* suggested that these differences could be due to different cellular growth rates, distinct ability to degrade PHA or an asymmetric PHA distribution during cell division [246].

FCM population analysis identified two distinct cell populations: smaller, less complex cells with higher intracellular Fe^{2+} and lower PHA content, and larger, more complex cells with lower Fe^{2+} and higher PHA levels (**Figure A4**). Our results suggest that cells with higher intracellular labile Fe^{2+} content typically exhibit higher magnetosome presence. Moreover, according to FCM population analysis, these high Fe^{2+} cells presented lower PHA levels, supporting the proposed hypothesis of the existence

of an energy competition between magnetosome and PHA production. Nevertheless, further research is required to verify this relationship and to more comprehensively determine the specific conditions that stimulate PHA formation in MTB.

The observed differences in cell size, complexity, intracellular iron concentration, and PHA content among these populations can be attributed to several factors. Variability in the cell cycle and growth phase, as well as phenotypic heterogeneity, can result in differences in cell morphology and intracellular contents. Environmental microgradients, such as variations in nutrient or oxygen availability, may also create localized differences in bacterial behavior. Furthermore, different stages of magnetosome formation and metabolic imbalances can influence iron and PHA accumulation. Finally, stress responses and genetic diversity within the population can further contribute to the observed heterogeneity [248].

3.4. Conclusions

The present study explored the effects of iron and oxygen availability on MSR-1 growth, magnetosome biogenesis and the dynamics of its intracellular iron pool at a multi-scale level, to gain further insights into the magnetosome biomineralization process. A correlative microscopy approach was conducted by employing cryoSIM and cryoSXT for the first time in MSR-1 and further complemented with FCM, ICP-OES and TEM. Our findings confirm the critical role of iron for both MSR-1 growth and magnetosome formation. Data obtained from FCM and ICP-OES suggested a potential association in which higher intracellular iron levels facilitate greater magnetosome production. This relationship was demonstrated at the single-cell level by employing correlative microscopy analysis revealing a direct correlation between the labile intracellular Fe^{2+} pool and magnetosome content. This demonstrated that cells exhibiting higher intracellular labile Fe^{2+} concentrations possessed a greater number of magnetosomes than those with lower iron levels. Additionally, the variation of iron dosages in the media directly impacted both magnetosome chain length and the intracellular iron concentration, with higher extracellular iron concentrations resulting in longer chains and increased iron uptake. We have identified a saturation point at approximately 300 µM iron citrate, beyond which additional iron supplementation did not further increase magnetosome chain length or total intracellular iron concentrations. Moreover, our results also demonstrated that only a fraction of the total intracellular iron content corresponded to magnetite as the intracellular labile Fe^{2+} pool persisted without depletion throughout the biomineralization process. These findings align with proposed MTB iron uptake models

suggesting that iron is first accumulated in the cytoplasm before being transported to the magnetosome vesicles. Overall, these findings highlight the value of single-cell analysis and the necessity of adopting a holistic methodology across different scales to enhance our comprehension of magnetosome biomineralization necessary for efficient future biomanufacturing.

Chapter 4.

Impact of oxidative stress on *Magnetospirillum gryphiswaldense* MSR-1 physiology and magnetosome biomineralization

4.1. Introduction

Oxidative stress is a consequence of the excessive production of ROS, which are by-products of oxygen reduction in metabolic processes [137]. Organisms residing in oxygen-rich environments have developed scavenging systems to mitigate this oxidative stress [249]. However, when ROS accumulation surpasses the cellular antioxidant defence mechanisms, it can lead to damage of nucleic acids, proteins, lipids, and other cellular components, directly compromising cell viability [138]. Controlling ROS accumulation is thus a critical parameter in bioprocessing. Excessive ROS not only affects cell health and viability, but also induces oxidative modifications that can affect product quality, introduces variability in cell growth and limits productivity. Therefore, the activation of cellular stress responses that alter metabolism and cell behaviour can further impact the efficiency and consistency of the bioprocess.

The magnetic nanoparticles naturally produced by MTB, called magnetosomes, represent an attractive alternative to chemically synthesized magnetic nanoparticles for biomedical and biotechnological applications due to their unique properties [5]. Magnetosomes are intracellular membrane-enveloped magnetic nanosized crystals of either magnetite (Fe_3O_4) or greigite (Fe_3S_4) depending on the species, typically arranged in a needle-like chain that acts as a compass needle enabling an active orientation within the Earth's magnetic field.

Magnetosome synthesis involves a complex and highly regulated biomineralization process that requires large amounts of iron [46]. However, elevated intracellular levels of iron ions can lead to significant oxidative stress as hydrogen peroxide (H_2O_2) reacts with ferrous iron (Fe^{2+}) in the so-called “Fenton reaction” to produce hydroxyl radicals (•OH) [139], which are among the most toxic ROS. Therefore, monitoring cell physiology during cell growth and magnetosome production is crucial to ensure cell viability and to control iron homeostasis to avoid the formation of specific physiological inhibitors, such as excessive ROS accumulation.

The mechanisms by which MTB tackle oxidative stress remain a significant and unresolved research question. Several studies have identified oxidative stress regulation mechanisms in these bacteria that are similar to those in other prokaryotic organisms. For instance, the presence of an OxyR-like redox-sensing transcription factor has been identified in some MTB species such as *Magnetospirillum gryphiswaldense* MSR-1 and *Magnetospirillum magneticum* AMB-1 [38], [40], [140]. Additionally, it has been observed that magnetosomes possess peroxidase-like activity, which could contribute to lowering overall ROS levels [37]. This potential ROS scavenging role of magnetosomes has suggested additional functions for magnetosome chains beyond merely aiding in orientation within a magnetic field.

In this study, changes in magnetosome biomineralization and cell physiology in the MTB species *Magnetospirillum gryphiswaldense* MSR-1 were monitored upon exposure to external oxidative stress conditions, such as the addition of H_2O_2 and high levels of extracellular iron (in the form of Fe(III)-citrate). To evaluate the effects of these stress factors, both magnetosome-producing and non-magnetosome-producing cells were used to further explore the potential role of magnetosomes as ROS scavenging agents by tracking changes in key physiological parameters, including cell viability, cell growth, intracellular iron accumulation, PHA formation, and ROS accumulation.

To this end, FCM was employed as an in-line tool for the rapid assessment of the physiological state of MSR-1 cells, focusing on parameters such as cell viability, intracellular ROS levels, and PHA formation. Additionally, ICP-OES was used as an offline tool to quantify magnetosome and iron content. To further complement this dataset, a correlative light and electron microscopy (CLEM) study was conducted. To the best of our knowledge, only a few correlative microscopy studies had been performed on MTB [215]–[217], and none have combined cryoEM with cryo-fluorescence microscopy before. In this study, cryoEM provided detailed structural information on MSR-1 cells and enabled the characterization of magnetosome content, while cryo-fluorescence microscopy was employed to evaluate ROS and intracellular iron accumulation. This strategy aimed to elucidate the relationship between ROS, the intercellular labile iron pool and magnetosome content at the single-cell level. Ultimately, understanding these interactions will enhance the consistency and efficiency of bioprocesses, ensuring cell health and optimizing the production of high-quality magnetosomes.

4.2. Materials and methods

4.2.1. Strains, growth media and culture conditions

Magnetospirillum gryphiswaldense MSR-1 (DMSZ 6631) was grown in FSM, comprising 3.5 $g \cdot L^{-1}$ potassium L-Lactate, 0.1 $g \cdot L^{-1}$ KH_2PO_4, 0.15 $g \cdot L^{-1}$ $MgSO_4 \cdot 7H_2O$, 2.38 $g \cdot L^{-1}$ HEPES, 0.34 g·L−1 $NaNO_3$, 0.1 $g \cdot L^{-1}$ yeast extract, 3 $g \cdot L^{-1}$ soy bean peptone, 100 µM iron citrate ($C_6H_5FeO_7$) and 5 $mL \cdot L^{-1}$ EDTA-chelated trace elements solution (EDTA-TES). EDTA-TES solution consisted of 5.2 $g \cdot L^{-1}$ EDTA disodium salt; 30 $mg \cdot L^{-1}$ H_3BO_3; 85.4 $mg \cdot L^{-1}$ $MnSO_4 \cdot H_2O$; 190 $mg \cdot L^{-1}$; 2.1 $g \cdot L^{-1}$ $FeSO_4 \cdot 7H_2O$, $CoCl_2$ $g \cdot L^{-1}$; 4 $mg \cdot L^{-1}$ $NiCl_2 \cdot 6H_2O$; 2 $mg \cdot L^{-1}$ $CuCl_2 \cdot 2H_2O$; 44 $mg \cdot L^{-1}$ $ZnSO_4 \cdot 7H_2O$ and 36 $mg \cdot L^{-1}$ $Na_2MoO_4 \cdot 2H_2O$. The pH of FSM and EDTA-TES was adjusted to 7.0 and 6.5, respectively, using 1 M NaOH prior to autoclaving.

MSR-1 cultures were grown in 100 mL DURAN® bottles, each with a working volume of 90 mL, under aerobic and microaerobic conditions in an Incu-Shake MAXI® (SciQuip Ltd, Newtown, UK) orbital shaker incubator set at 150 rpm and 30°C. To generate microaerobic conditions, bottles were purged with N_2 for 30 min to remove all the dissolved O_2 and sealed with bromobutyl rubber stoppers, and later injected with the necessary sterile air volume to achieve ~ 1% O_2. Aerobic bottles were left with their lids slightly loosened to allow free air exchange.

Each bottle was inoculated at a 1:10 ratio and incubated for 60 hours, with samples taken every 6-12 hours for analysis. During the early exponential growth phase, a pulse of iron citrate (final iron concentration of 400 µM) or H_2O_2 (final concentration of 150 µM) were added to both aerobic and microaerobic cultures to induce oxidative stress. Experiments were carried out in triplicate.

4.2.2. Bacterial growth and magnetic cellular response

Bacterial growth was assessed by measuring the optical density of cultures using an Evolution 300 UV-Vis spectrophotometer (Thermo Fisher Scientific, Hemel Hempstead, Herts, UK) at a wavelength of 565 nm (OD_{565}). The cellular magnetic response (C_{mag}) was evaluated according to a previously described method immediately after the OD_{565} measurements [23]. In brief, the spectrophotometer has two pairs of Helmholtz coils mounted on the cuvette holder, one pair oriented perpendicular to the light beam and the other parallel. For magnetic cells, the different alignments result in varying optical densities due to cell migration as a result of the applied magnetic field, whereas non-magnetic cells show no change when the magnetic field orientation is altered, thus maintaining constant optical density. C_{mag} values are then determined by the ratio of OD_{565} measurements for cells aligned parallel and perpendicular to the light beam. C_{mag} values range between 1 and 3, with values exceeding 1 indicating the presence of magnetic cells.

4.2.3. Flow cytometry

Bacterial samples were collected from the liquid cultures, diluted in PBS, and directly analysed in a BD Accuri C6 flow cytometer (Becton, Dickinson and Company, Oxford, UK). FCM was employed to determine relative cell size (FSC-A), cell granularity/complexity (SSC-A), intracellular soluble iron concentration, cell viability, PHA formation and ROS accumulation. The soluble intracellular iron pool was detected by incubating the cells with PG-SK fluorophore (5 µM) for 10 min; PHA granules were stained with Pyr-546 (0.5 µg/mL); cell viability was assessed by incubating the cells with propidium iodide (PI) (100 ng/mL) and bis (1.3-dibutybarbituric acid) trimethine oxonol (BOX) (100 ng/mL) for 2 min; and the presence of ROS was detected by incubating the cells for 30 min at 30°C with CellROX™ Deep Red (CRDR) fluorophore (5 µM). Cells stained with green (PG-SK, Pyr-546, BOX) and red fluorophores (PI) were excited with a 488 nm solid-state laser, with fluorescence detected using a 533/30 BP filter and a 670 LP filter, respectively. Far-red fluorescent labelled cells (CRDR) were excited with a 640 nm solid-state laser and detected through a 675/25 BP filter. Details of MSR-1 CRDR staining optimization are provided in the **Appendix B1**.

4.2.4. Determination of iron content

ICP-OES (Thermo Scientific iCAP 7000) was employed as an offline analysis to monitor the changes in the intracellular and extracellular iron concentrations of MSR-1 cultures. One mL of each sample was centrifuged to separate cells from the culture media. Supernatants were acidified by adding 10 µL of the nitric acid solution, while cell pellets were digested using 500 µL of a nitric acid (70% v/v) solution and incubated at 98°C for 2 h with shaking at 300 rpm. After digestion, the final volume was re-adjusted to 1 mL by adding deionized water. Samples preparation was done and analysed in triplicate.

4.2.5. Correlative light and electron microscopy

MSR-1 cells were grown until just before the end of their exponential growth phase. To detect intracellular iron and ROS accumulation, cells were incubated with PG-SK and CRDR, respectively. Vitrification of the samples was performed at The Electron Bio-Imaging Centre (eBIC) located at Diamond Light Source UK's synchrotron (**Figure B4**). Approximately 4 µL of the cell suspension was applied to the front of Quantifoil R2/2 grids, with 0.5 µL applied to the back. The grids were then blotted for 6 seconds using an EM GP2 Automatic Plunge Freezer (Leica Microsystems) before plunge freezing.

After sample vitrification, the grids were transferred to a Leica EM cryoCLEM microscope (Leica Microsystems) to acquire fluorescence data. ROIs were identified based on fluorescence signals indicative of intracellular iron and ROS accumulation. The identified ROIs were subsequently imaged using a Titan Krios microscope (Thermo Fisher Scientific), operated at 300 kV with a Gatan K3 detector. Two-dimensional search maps were acquired at a magnification of 4800X. For tomographic data collection, a magnification of 8700X was used, corresponding to a pixel size of 10.51 Å. The total electron dose was 27.53 $e^-/Å^2$. Tilt series were acquired from +60° to -60° in 3° increments, with a defocus value of -25 µm. Tomograms were reconstructed using the IMOD software package (University of Colorado, Boulder, CO). Microscopy Image Browser and UCSF ChimeraX were employed for volume segmentation and visualization of tomograms [236], [250].

From 2D search maps, several parameters were measured using Fiji (ImageJ) software, including cell length (n = 50 cells per condition), number of magnetosomes per cell (n = 50 cells per condition), percentage of area occupied by PHA granules relative to the total cell surface area (n = 20 cells per condition), and magnetite crystal size (n = 500 crystals per condition).

4.3. Results and Discussion

4.3.1. MSR-1 physiological responses to stress conditions

This section describes the effects of external oxidative stress conditions, induced by the addition of H_2O_2 and iron citrate mid-growth, on MSR-1 physiology by assessing various parameters, such as cellular growth, cell viability, cell morphology and size, PHA formation and ROS accumulation.

4.3.1.1. MSR-1 growth and viability

MSR-1 was grown under microaerobic and aerobic conditions to obtain magnetosome-producing cells and non-magnetosome-producing cells, respectively. When the bacterial cells reached the early exponential growth phase ($OD_{565} \simeq 0.15$) a pulse of iron citrate (400 µM) or H_2O_2 (150 µM) was introduced to induce oxidative stress. The concentrations of iron citrate and H_2O_2 used in this experiment were selected based on literature data [38], [40], [126], [127], [251] and H_2O_2 tolerance tests performed on MSR-1 (**Figure B5**)**.**

Bacterial growth and cell viability were monitored over a period of 60 h. In microaerobic cultures, the addition of iron citrate did not impact bacterial growth (**Figure 4.1A**) or cell viability (**Figure 4.1B**). The extracellular iron concentration increased from 6 mg/L to approximately 20 mg/L following the iron

citrate pulse (**Figure B6**). Although previous work suggests that a 20 mg/L concentration should be toxic for MSR-1 [126], [127], our findings reported in **Chapter 3** and again herein, indicate that neither bacterial growth (**Figure 3.1F**) nor cell viability (**Figure B7A**) were affected by the increase of the extracellular iron concentration (across the studied concentration range up to 55 mg/L). In contrast, while bacterial growth in aerobic cultures remained unaffected by the addition of iron citrate (**Figure**

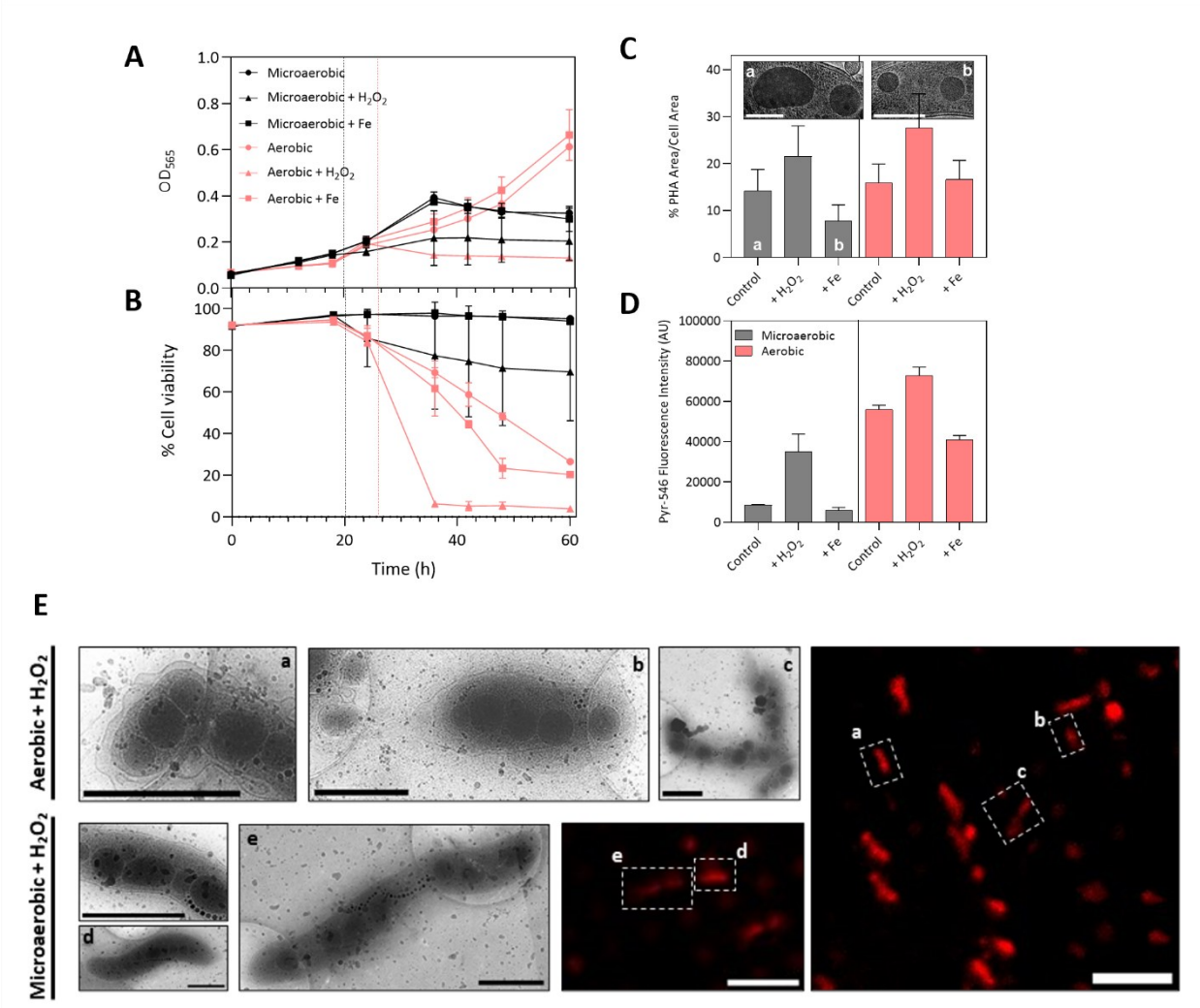

Figure 4.1. Effects of iron citrate and H_2O_2 addition on the physiology of MSR-1 cells grown under microaerobic and aerobic conditions. (A) Time course of cell growth. (B) Cell viability over time, determined by FCM. Vertical lines in graphs A and B indicate the addition of iron and H_2O_2 pulses in microaerobic (black) and aerobic (red) cultures. (C) Percentage of PHA area relative to the total cell area, measured from cryoEM images when MSR-1 cells were at the end of the exponential growth phase (n=20 cells/condition). Inset cryoEM images: (a) microaerobic condition and (b) microaerobic condition with iron addition. Scale bar = 300 nm. (D) Analysis of PHA content by FCM using Pyr-546 fluorophore. (E) CryoEM images of MSR-1 cells grown under aerobic and microaerobic conditions after the addition of H_2O_2 (~150 µM). The cryo-fluorescence image shows MRS-1 cells exposed to H_2O_2, incubated with the CellROX Deep Red fluorophore, which detects the presence of reactive oxygen species (ROS). The areas labelled (a-e) in the cryo-fluorescence images correspond to the cells highlighted in the cryoEM images with the same labels. Scale bar = 1 µm (cryoEM) and 10 µm (cryo-fluorescence). 25 000 events were analysed per sample by FCM. Error bars represent the standard deviation of triplicates. FCM = Flow Cytometry; CryoEM = cryo-electron microscopy; Pyr-546 = Pyrromethene-546.

4.1A), cell viability declined more rapidly compared to control conditions (**Figure 4.1B**). This accelerated decline is tentatively attributed to potential cellular damage caused by the the Fenton reaction [139].

In contrast, the addition of H_2O_2 significantly impacted bacterial growth (**Figure 4.1A**). Aerobic growth was completely ceased as the OD_{565} values dropped from 0.19 to 0.13, likely due to cell lysis. Meanwhile, the growth rate under microaerobic conditions was reduced but not completely restrained (OD_{565} = 0.22) compared to the control conditions (OD_{565} = 0.37). Furthermore, aerobic cultures exhibited a steeper decline in cell viability compared to microaerobic cultures (**Figure 4.1B**). Following H_2O_2 addition, cell viability in microaerobic cultures decreased by only 25% relative to the control, while the viability of aerobic cultures dropped sharply from 85% to less than 10% immediately after the H_2O_2 pulse. Maintaining cellular viability, membrane selective permeability, and proton motive force are features of intact membranes [252]. When H_2O_2 is added, it can interact with the bacterial cell membrane, causing lipid peroxidation [253]. Oxidative stress can also reduce proton motive force by inhibiting transport across the cell membrane, which reduces ATP production, and consequently inhibits cell growth leading to cell death [254].

There are only a few studies published on the impact of H_2O_2 on MTB growth. The majority of which were performed under microaerobic conditions solely and started to see a significant impact on bacterial growth at 200-300 µM concentrations in the media [40], [251], [255]. However, these studies typically grew the bacteria with different H_2O_2 concentrations from the start, whereas our study introduces a pulse of H_2O_2 during mid-growth, which may explain the differences in the observed behaviour.

4.3.1.2. MSR-1 cell morphology, size and complexity

The impact of external oxidative stress on the morphology, size, and complexity of MSR-1 cells was analysed, with a focus on the changes induced by doping high iron and H_2O_2 concentrations. FCM analysis provides insights into cell size and granularity, while cryoEM images offer high-resolution details of cellular structures. Together, these methodologies reveal the extent to which oxidative stress affects MSR-1 cells, highlighting differences in their structural and intracellular organisation.

The obtained results indicate that the addition of iron does not result in any noticeable morphological differences when grown under microaerobic or aerobic conditions. In contrast, as shown in **Figure 4.1E**, H_2O_2 doping induces various effects on MSR-1 morphology. Aerobic cells subjected to H_2O_2 exhibited significantly more structural cell damage compared to microaerobic cells. The cell membrane

of aerobic cells was notably compromised, with many cells losing their characteristic spirillum shape and becoming smaller and more rounded (**Movie 4.1**). Some cells also appeared to be broken. Although some damage was observed in microaerobic cells exposed to H_2O_2, it was considerably less severe compared to the damage seen in aerobic conditions (**Figure 4.1E**). This difference in structural cellular damage correlates with the larger decrease in cell viability observed in **Figure 4.1B** under H_2O_2-doped aerobic conditions, where viability was reduced by 80%, compared to a 25% reduction in H_2O_2-doped microaerobic cultures. The sensitivity of bacterial cells to H_2O_2 has been documented in other bacterial species. For instance, *Campylobacter jejuni* changes from a spiral-shaped to a coccoid form upon interaction with ROS [256], while *Escherichia coli* turns from a bacillus form to a coccoid form [257]. These morphological changes occur as bacteria attempt to repair the membrane damage caused by ROS, which, if unrepaired, may lead to DNA damage and cell death [258]. **Table 4.1** displays the differences in cell length under iron and H_2O_2 doping conditions, with cell length measured from cryoEM 2D search maps using Fiji software. The results revealed that exposure to H_2O_2 led to significantly shorter cells, about half the size of those in the control group, while iron exposure had no effect on cell size. This reduction in size is likely due to morphological changes caused by lipid peroxidation of the cell membrane from H_2O_2 exposure. Our findings also indicate that aerobic cells were significantly longer (8.3 ± 3.1 µm) than microaerobic cells (6.1 ± 1.8 µm) (one-way ANOVA with Tukey test, $p < 0.01$). Some aerobic cells even reached double the size of some microaerobic cells, measuring up to 16 µm, which has also been previously reported by others [33]. The analysis of the forward scatter (FSC-A) data from the FCM which provides information regarding cell size, are in line with the microscopy results, showing that aerobic cells generally exhibited longer dimensions than microaerobic cells (**Figure B8A**). Besides oxygen availability, other changes in the growth conditions or other stress factors, such as variations in lactic acid and nitrate concentrations in the media [11], the method of cultivation (plates *vs.* liquid cultures) [18], or exposure to UV-B radiation [39], have been shown to affect the size and morphology of MTB. Monitoring and controlling cell size is therefore important, as this phenotypic feature can significantly impact bioprocess efficiency, influencing both upstream factors like nutrient uptake and downstream processes such as cell disruption and product recovery [16].

FCM was also used to obtain information regarding the intracellular cell complexity or granularity, assessed through side scatter (SSC-A) measurements. In MSR-1, aside from magnetosome chains, cells typically accumulate intracellular inclusions such as phosphate or PHA granules [259]. As well known, PHA synthesis is notably enhanced under conditions of nutrient deficiency or oxidative stress, particularly when there is an excess of carbon source. Monitoring PHA synthesis is important because PHAs serve as reservoirs for reducing power, thereby helping to manage intracellular redox balance

Table 4.1. Effects of doping iron citrate and H_2O_2 on cell length (n=50/condition), magnetosome content (n=50/condition) and magnetite crystal size (n=500/condition) in microaerobic and aerobic MSR-1 cells. All measurements were obtained from cryoEM 2D search maps using Fiji software.

	Cell length (μm)		Magnetosomes/cell		Magnetite size (nm)	
	Microaerobic	Aerobic	Microaerobic	Aerobic	Microaerobic	Aerobic
Control	6.1 ± 1.8	8.3 ± 3.1	24.6 ± 5.5	11.8 ± 7.9	48.6 ± 10.5	34.5 ± 9.4
H_2O_2 addition	3.7 ± 1.8	4.5 ± 1.8	20.7 ± 7.2	8.0 ± 4.7	43.4 ± 10.6	43.1 ± 10.7
Iron addition	5.9 ± 1.0	7.5 ± 2.1	31.8 ± 7.0	8.4 ± 5.0	48.2 ± 11.4	35.0 ± 8.1

and mitigate ROS formation [142]. By sequestering reducing equivalents (e.g. NADH, NADPH), PHA synthesis prevent the accumulation of excessive reducing agents, which could otherwise contribute to redox reactions and promote uncontrolled ROS production, leading to oxidative damage. During periods of starvation, cells can degrade PHAs to release monomers that enter central metabolic pathways, such as the TCA cycle and glycolysis, thereby restoring the cellular reducing power necessary for maintaining redox balance [143]. Here, PHA granules were stained with the Pyr-546 fluorophore, and their accumulation was monitored through FCM analysis. The changes in cell granularity (SSC-A) and Pyr-546 intensity values over time are shown in **Figure B8B** and **Figure B8C,** respectively. Both plots clearly indicate that aerobic conditions exhibited higher fluorescence and SSC-A values, suggesting increased PHA granule synthesis under these conditions. Our results are in accordance with the investigation of Su *et al.* using the AMB-1 strain in which they observed a decrease in PHA content under anaerobic conditions and an increase under aerobic conditions [144]. **Figure 4.1C** and **Figure 4.1D** display the percentage of PHA inclusions in the cytoplasmic space and Pyr-546 fluorescence intensity values, respectively, for MSR-1 cells at the end of the exponential growth phase. Both analytical approaches (FCM and cryoEM) showed similar trends in PHA content across the different conditions. Under aerobic conditions, iron addition did not result in significant differences in PHA content as cells exhibited similar values to the control conditions (16% PHA area/cell area). However, under microaerobic conditions, the PHA area relative to total cell area decreased significantly from

14% to 8% with iron addition (one-way ANOVA with Tukey test, $p < 0.01$). CryoEM images in **Figure 4.1C** further demonstrate that the size of PHA granules was significantly reduced after iron addition under microaerobic conditions. The higher PHA content observed in H_2O_2-exposed cells (22% and 28% for microaerobic and aerobic cultures, respectively) is likely biased by the changes in cell size and morphology resulting from H_2O_2-induced cell damage. For instance, broken cells had cytoplasmic leakage, reducing the total cell area and thereby increasing the ratio of PHA to cytoplasmic space, due to the cell damage rather than increased PHA production.

4.3.1.3. Intracellular ROS accumulation

MSR-1 cells were stained with CellROX Deep Red (CRDR) fluorophore and analysed by FCM to investigate the accumulation of ROS. This fluorescent probe has been effectively employed for ROS detection in other Gram-negative bacteria such as *Escherichia coli* [260] and *Fusobacterium nucleatum* [261].

Figure 4.2A illustrates ROS accumulation of MSR-1 cells exposed to oxidative stress conditions over time. Generally, cells under aerobic conditions exhibited significantly higher levels of intracellular ROS compared to those under microaerobic conditions. In microaerobic cultures, the addition of iron did not lead to an increase in ROS production. This was consistent with complementary experiments in which MSR-1 cells were grown with varying iron concentration (up to 1 mM) as shown in **Figure B7B**. In previous work, gene expression analysis performed during cell growth and magnetosome synthesis revealed that genes associated with ferric reductases, ferrous transport system and ROS scavenging are highly expressed when exposed to high iron concentrations [39]. The upregulation of ROS scavenging-related genes under high iron concentration presumably facilitates the ability of MTB to uptake large amounts of iron and thrive in iron-rich environments. However, under aerobic conditions, an increase in ROS production was observed towards the end of the exponential growth phase in cells subjected to an iron pulse, likely due to the Fenton reaction.

The addition of H_2O_2 resulted in a moderate increase in ROS accumulation for microaerobic conditions compared to the control (**Figure 4.2A** and **Figure 4.1E**). Surprisingly, H_2O_2-aerobic cultures exhibited lower CRDR fluorescence values compared to the control conditions when analysed by FCM. However, fluorescence microscopy images (insets in **Figure 4.2A**) revealed similar fluorescence levels to those achieved in aerobic control conditions. Aerobic cells were significantly damaged under the influence of H_2O_2, resulting in smaller, more compact, and even fragmented cells (**Figure 4.1E**). This

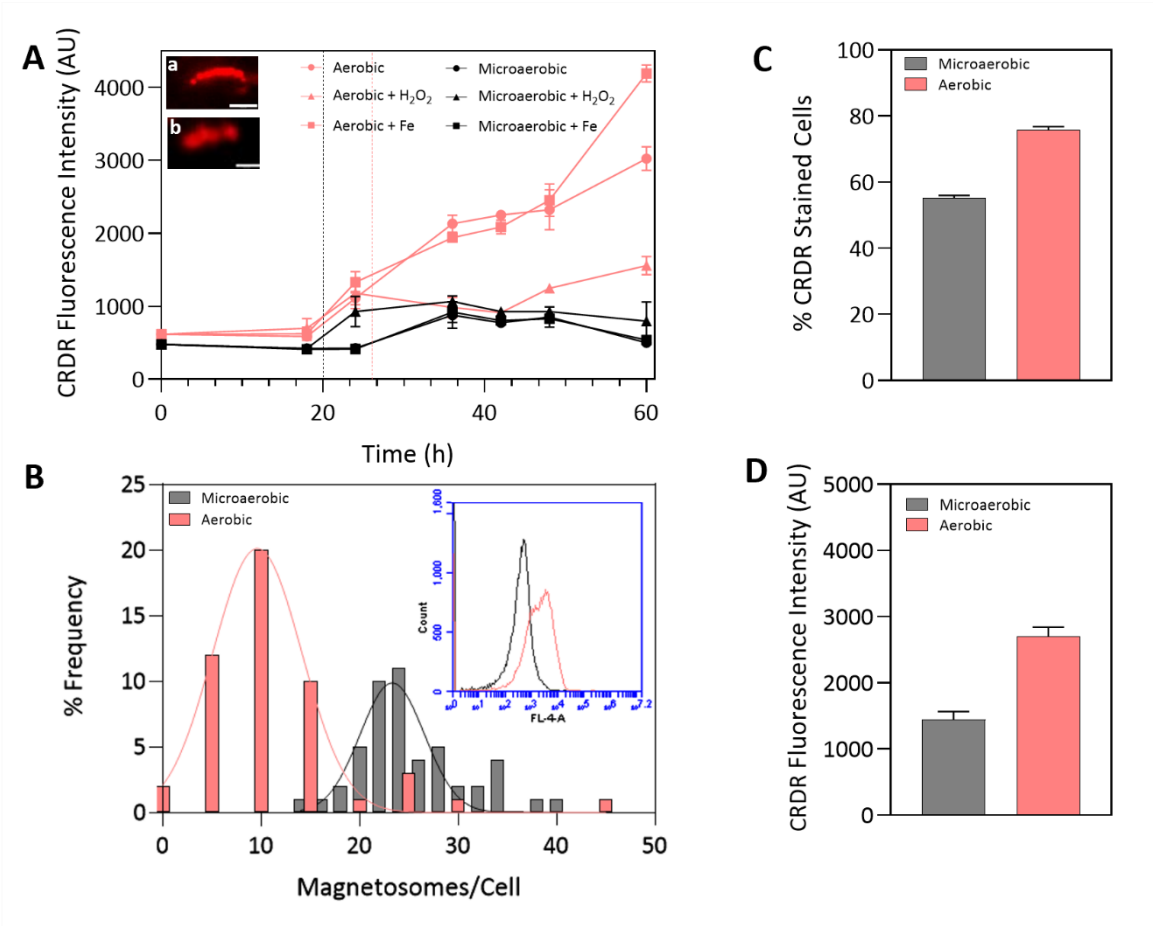

Figure 4.2. (A) Accumulation of ROS in CRDR-stained MSR-1 cells by FCM. Inset cryo-fluorescence images: (a) aerobic control condition and (b) aerobic condition with H_2O_2 addition. Scale bar = 2 µm. (B) Magnetosome chain length histogram distribution of aerobic and microaerobic cells. The inset graph corresponds to CRDR fluorescence histograms obtained from FCM analysis of aerobic and microaerobic cells. Comparison between aerobic and microaerobic MSR-1 cells of (C) the percentage of CRDR-stained cells and (D) the fluorescence intensity values of the CRDR-stained cells only. Vertical lines in graph (A) indicate the addition of iron and H_2O_2 pulses in microaerobic (black) and aerobic (red) cultures. 25 000 events were analysed per sample by FCM. Error bars represent the standard deviation of triplicates. CRDR = CellROX Deep Red; FCM = Flow Cytometry; AU = arbitrary units.

morphological change may explain the decrease in CRDR fluorescence detected by FCM, as the fragmented cells have reduced overall fluorescent content compared to intact cells.

Using the gating capability of FCM, a more in-depth analysis of ROS distribution was conducted by comparing low magnetosome-producing cells (aerobic) with high magnetosome-producing cells (microaerobic), as magnetosomes are believed to decrease and eliminate ROS due to their peroxidase-like activity [37]. Analysis of the proportion of CRDR-stained cells (ROS^+) in **Figure 4.2C** revealed only a 20% difference between these two conditions, with 55% of ROS^+-microaerobic cells compared to 75% ROS^+-aerobic cells. However, a closer examination of the mean fluorescence intensity values of ROS^+ cells (**Figure 4.2D**) reveals that ROS^+-aerobic cells showed double the fluorescence compared to ROS^+-microaerobic cells, indicating clear contrast in ROS levels between the two conditions.

Additionally, based on FSC-A (cell size) and SSC-A (cell granulometry) plots, two distinct populations can be identified for both microaerobic and aerobic conditions (**Figure B9A**). The first population (P1) consists of smaller cells with fewer granules, constituting approximately 70% of the total cell population, while the second population (P2) consists of larger cells with higher granule content, representing the remaining 30%. Both aerobic populations also exhibited a much higher percentage of ROS^+ cells (P1: 70%; P2: 90%) compared to microaerobic populations (P1: 45%; P2: 70%) (**Figure B9B**). A similar trend to the one previously observed is clear, with aerobic populations displaying at least twice the level of fluorescence compared to microaerobic populations (**Figure B9C**). It is also noteworthy to mention that the difference in fluorescence values between P1 and P2 under microaerobic conditions is only 1.6-fold, whereas under aerobic conditions, it is 2.2-fold. This indicates lower fluorescence heterogeneity, and thus lower ROS levels, in magnetosome-producing cells (microaerobic) compared to non-magnetosome-producing cells (aerobic). This fluorescence heterogeneity is also reflected in the FCM fluorescence histograms (**Figure 4.2B** inset). The CRDR fluorescence peak observed in the CRDR histograms for microaerobic cells was narrower compared to the broader distribution observed for aerobic cells. This pattern was in line with the magnetosome chain length distribution plots for both conditions (**Figure 4.2B**), where the distribution of magnetosome chain lengths in aerobic cells was much more dispersed than in microaerobic cells. The aerobic distribution has a coefficient of variation (CV) of 135%, indicating higher relative dispersion compared to the microaerobic distribution, which has a CV of 96%. This suggests that the higher fluorescence heterogeneity observed in aerobic conditions is potentially correlated with greater heterogeneity in magnetosome content. Considering that prior studies have demonstrated that MSR-1 mutants deficient in magnetosome production exhibit significantly higher ROS levels compared to the wild-type MSR-1 strains capable of magnetosome production [37], our findings suggest a potential correlation between the heterogeneity in magnetosome content and ROS levels, as reflected by the observed fluorescence heterogeneity.

4.3.2. Impact of stress conditions on magnetosome biomineralization

The regulation of iron homeostasis is intrinsically linked with the bacterial response to oxidative stress, reflecting a coordinated control system to manage these demands [262]. In MTB this coordination is particularly crucial, as iron is a key component in magnetosome biomineralization. In here, the impact of stress conditions on magnetosome formation in magnetosome-producing and non-magnetosome-producing MSR-1 cells is further explored. Understanding these interactions and regulatory

mechanisms is vital for elucidating how MTB manage iron homeostasis while minimizing oxidative damage. Thus, it is of special interest to improve current bioprocessing strategies.

4.3.2.1. Magnetosome chain length, morphology and crystal size

Changes in the culture media and external environmental factors, such as temperature, pH, dissolved oxygen and iron concentration can affect the number and shape of the magnetosome crystals [5], [132], [263], [264]. In this study, the impact of adding H_2O_2 and iron citrate on magnetosome content, chain morphology, and crystal size was analyzed using cryoEM (**Table 4.1**).

Despite the suppression of magnetosome biomineralization under aerobic conditions [33], magnetosome chains were still present due to the high magnetism of the inoculum used (C_{mag} = 2.7, **Movie 4.2**). However, as displayed in **Table 4.1**, the chains in aerobic cells were only half as long (11.8 ± 7.9 magnetosomes/cell) as those in microaerobic cells (24.6 ± 5.5 magnetosomes/cell) (**Movie 4.3**). The addition of iron and H_2O_2 to aerobic cells did not significantly alter the number of magnetosomes per cell. In contrast, under microaerobic conditions, the iron pulse resulted in the formation of significantly (one-way ANOVA with Tukey test, $p < 0.01$) longer magnetosome chains (31.8 ± 2.1 magnetosomes/cell). These findings align with our previous observations in **Chapter 3**, which demonstrated that increasing extracellular iron content promotes the formation of longer magnetosome chains.

As shown in **Figure 4.3G**, the spacing between magnetite crystals in aerobic cells was larger compared to microaerobic cells [33]. While the addition of iron did not induce any noticeable changes in magnetosome chain morphology, the exposure to H_2O_2 affected the chain structure. The oxidative stress induced by H_2O_2 led to the loss or deformation of the typical needle-like shape and, in some cases, caused chain fragmentation. MamK is an actin-like protein responsible for organizing the magnetosome chain along the cell axis [45]. Similar to what has been observed in eukaryotic cells, where H_2O_2 disrupts actin dynamics [25], oxidative stress from H_2O_2 could have impaired the function of MamK, leading to the observed structural alterations.

Measurement of magnetite crystal size under the different culture conditions (**Table 4.1**) from 2D cryoEM search maps, revealed that microaerobic magnetosomes were significantly larger (48.6 ± 10.5 nm) than those present in aerobic cells (34.5 ± 9.4 nm) [219]. Iron addition did not enlarge magnetosome crystals under microaerobic conditions, but H_2O_2 exposure resulted in significantly smaller crystals (one-way ANOVA with Tukey test, $p < 0.01$). This reduction in magnetite crystal size caused by H_2O_2 is consistent with previous studies in which MSR-1 cells were exposed to similar H_2O_2

concentrations (200 μM) [130]. Although other research has reported a correlation between increased extracellular iron concentration and larger magnetite crystals in AMB-1 strain [167], our results did not show an increase in magnetite size upon iron addition (48.2 ± 11.4 nm). This discrepancy may be due to differences in experimental protocols, as bacteria were grown at different iron concentrations from the start, while in this study the iron pulse was added mid-growth, potentially affecting magnetite growth differently. Other studies have reported that increasing extracellular iron concentration can alter the morphology of magnetosome crystals rather than their size when iron uptake rates are affected [263]. Specifically, magnetosomes grown under high iron uptake rates displayed cuboidal morphologies, while those grown with slower iron uptake rates exhibited the classical cubo-octahedral morphology. These observations highlight the complexity of magnetosome biomineralization and emphasize the critical role of environmental factors in shaping magnetosome morphology.

4.3.2.2. Interplay between iron content and ROS accumulation

Figure 4.3A shows C_{mag} values recorded at regular intervals to enable online analysis of magnetosome content over time. The determination of the number of magnetosomes per cell by cryoEM was conducted at a single time point (at the end of the exponential growth phase), thus the collection of C_{mag} values ensured a more continuous assessment of magnetosome content, complementing the cryoEM data. As aforementioned, the inoculum used was highly magnetic, so C_{mag} values for microaerobic conditions were consistently high from the beginning and maintained throughout the experiment (C_{mag} = 2.3 - 2.9). For aerobic cultures there was a period of adaptation of approximately 20 hours in which cells switched to their aerobic metabolism. Afterwards, C_{mag} values began to decrease, down to 1.3, indicating the suppression of magnetosome production [11], [33]. There were practically no C_{mag} differences between the control and the iron-doping conditions for both microaerobic and aerobic conditions. Notably, differences in C_{mag} values were only observed in conditions where H_2O_2 was added (**Figure 4.3A**). These observations showed some inconsistencies with the cryoEM magnetosome content results displayed in **Table 4.1,** where no significant differences in magnetosome content were found upon H_2O_2 addition. Although C_{mag} measurements provide a qualitative and rapid assessment of magnetosome content, this technique is based on optical density, which can be influenced by other factors beyond magnetosome content alone, such as cell length and morphology [18]. The morphological changes induced by H_2O_2 were likely responsible for the discrepancies noted between the C_{mag} values and cryoEM data.

Total intracellular iron content results (**Figure 4.3B**) followed a trend similar to that observed in the C_{mag} results. In aerobic cultures, the iron concentration decreased up to 7 mg/g DCW, whereas in

microaerobic cultures, the iron concentration remained consistently high, around 30 mg/g DCW over time [33], [219]. Unlike C_{mag} data, microaerobic conditions with added iron displayed higher intracellular iron concentrations (38 mg/gDCW), likely due to the presence of longer magnetosome chains (**Table 4.1**). After H_2O_2 addition in aerobic conditions, the intracellular iron levels remained constant. This was attributed to the cease of cell growth and significant cell viability reduction (**Figure 4.1**) that these cells suffered under these conditions.

Measurement of the total intracellular iron content has been commonly used to assess magnetosome content. However, as noted in **Chapter 3** and by others, there are different intracellular iron pools distinct from magnetite [10], [119], [265]. In addition to its role in magnetite biomineralization, iron is also required for other general iron-dependent biochemical reactions [112], [227] or stored in proteins such as ferritins to prevent toxicity [121]. Consequently, some studies have suggested that only a

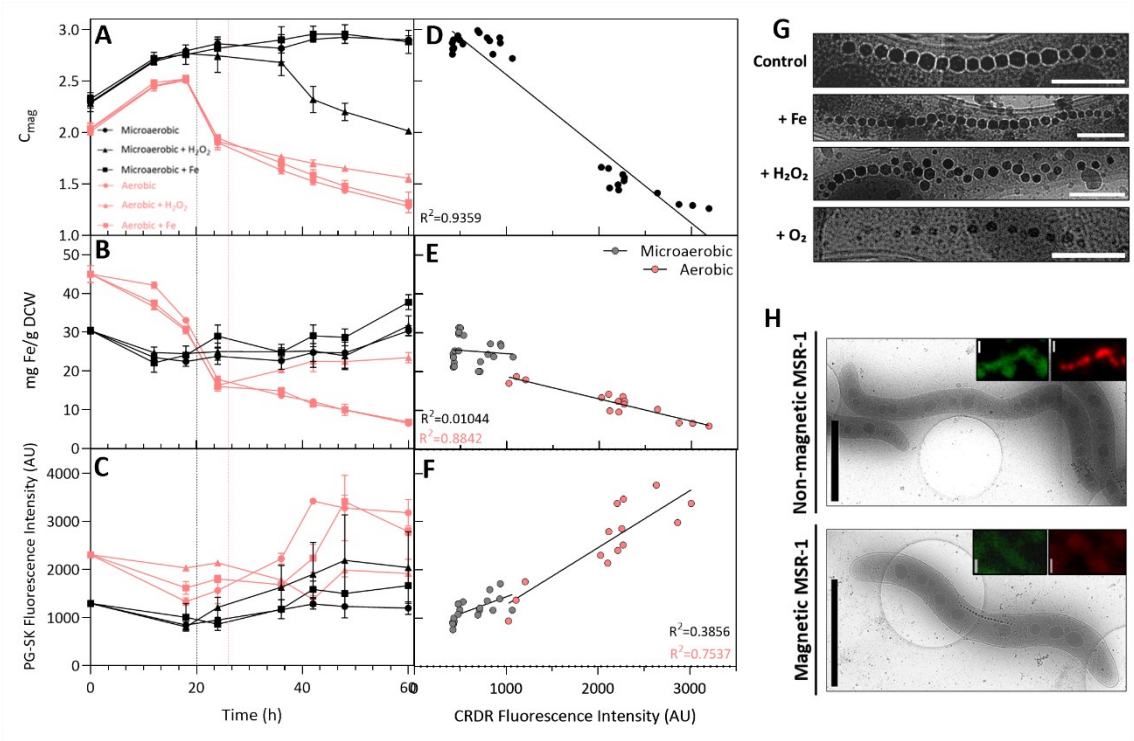

Figure 4.3. Analysis of iron dynamics and ROS accumulation during magnetosome biomineralization. (A) C_{mag}, (B) total intracellular iron content, and (C) labile ferrous iron levels in MSR-1 cells grown under various stress conditions over a period of 60 hours. Vertical lines in (A-C) indicate the addition of iron and H_2O_2 pulses in microaerobic (black) and aerobic (red) cultures. (D-F) Correlation of C_{mag} (n=30), total intracellular iron content (n=36), and labile ferrous iron levels (n=35) with intracellular ROS accumulation of microaerobic and aerobic cells, respectively. (G) Effects of the addition of iron citrate (+ Fe), hydrogen peroxide (+ H_2O_2) or aerobic conditions (+ O_2) on the magnetosome chain structure. Scale bar = 300 nm. (H) Comparison between non-magnetic (aerobic) and magnetic (microaerobic) MSR-1 cells using PG-SK and CRDR fluorescence, alongside their corresponding cryo-EM images. Scale bar = 2 µm. Labile ferrous iron levels and ROS accumulation were measured using (C-F) flow cytometry (FCM) or (H) cryo-fluorescence microscopy with PG-SK (green fluorescence) and CRDR (red fluorescence) fluorophores, respectively. 25 000 events were analysed per sample by FCM. Error bars represent the standard deviation of triplicates. CRDR = CellROX Deep Red; PG-SK = PhenGreen SK; AU = arbitrary units.

fraction of the total intracellular iron (25-45%) corresponds to magnetite [10], [119]. Hence the importance on also tracking changes of the soluble Fe^{2+} intracellular iron pool. This is particularly important because free iron (Fe^{2+}) can react with H_2O_2 to generate hydroxyl radicals.

Labile Fe^{2+} intracellular iron concentration was monitored by FCM using PG-SK fluorophore, which quenches upon binding to free Fe^{2+} ions [18], [228]. As shown in **Figure 4.3C**, aerobic cultures displayed higher green fluorescence values compared to microaerobic cultures, indicating a notably lower presence of Fe^{2+} under aerobic conditions. This observation was corroborated by cryo-fluorescence microscopy, as shown in **Figure 4.3H**. Under microaerobic conditions, the addition of H_2O_2 led to a decrease in Fe^{2+} levels. This decrease was likely due to oxidation of Fe^{2+} to Fe^{3+} via the Fenton reaction, as ROS levels also increased (**Figure 4.2A**).

In **Chapter 3**, a direct correlation between the number of magnetosomes and the intracellular Fe^{2+} iron pool was reported [265]. Cells with longer magnetosome chains exhibited higher Fe^{2+} levels than those with shorter chains (**Figure 3.3**). Additionally, not all internalized Fe^{2+} was used for magnetite synthesis, as a substantial labile Fe^{2+} pool remains even after biomineralization is complete [226]. Given these observations, in this chapter, we aimed to elucidate the relationship between ROS accumulation, the intracellular soluble iron pool and magnetosome content. To this end, C_{mag} values (**Figure 4.3D**), total intracellular iron content (**Figure 4.3E**) and intracellular Fe^{2+} levels (**Figure 4.3F**) were correlated with ROS accumulation. Furthermore, the cryoCLEM approach was employed to obtain data at the single cell level (**Figure 4.3H** and **Figure 4.4**) by comparing magnetic (microaerobic) and non-magnetic (aerobic) cells.

Evidence suggests that MSR-1 possesses homologues for the global regulators Fur [244], OxyR [251], and IrrB [266], indicating that these regulators work together to fine-tune iron homeostasis and oxidative stress responses during magnetosome biomineralization. In MSR-1, Fur is involved in regulating the transcription of Fe^{2+} transport systems *feoAB1* and *feoAB2*, as well as genes involved in oxidative stress responses, such as *katG* (catalase) and *sodB* (superoxide dismutase) [220], [244]. This highlights Fur's dual role in managing both iron levels and oxidative stress. OxyR, a key regulator of the oxidative stress response, responds to H_2O_2 by upregulating genes that mitigate ROS damage such as *katG* and *dps* (iron storage protein) [267]. Therefore, OxyR also indirectly influences iron metabolism by promoting iron sequestration and reducing free iron levels, thus helping to lower ROS formation [38]. The combined actions of Fur and OxyR underscore the complex interplay between iron regulation and oxidative stress management.

Our results shown in **Figure 4.3D** revealed an inverse correlation between C_{mag} values and ROS accumulation. Specifically, higher C_{mag} values, which indicate greater magnetosome content, were

associated with lower ROS levels. This suggests that increased magnetosome formation might be linked to reduced oxidative stress, potentially due to iron sequestration within magnetite or their peroxidase-like activity [37]. This trend is further supported by single-cell correlative microscopy images presented in **Figure 4.4**, where MSR-1 cells with higher magnetosome content exhibited lower CRDR fluorescence than cells with lower magnetosome content.

By analysing the correlation between the total intracellular iron content and ROS levels (**Figure 4.3E**), distinct patterns between microaerobic and aerobic conditions were observed. It was expected that, due to the Fenton reaction, cells with higher intracellular iron concentrations would exhibit elevated ROS levels, as excess iron can catalyse ROS formation. However, under microaerobic conditions, which

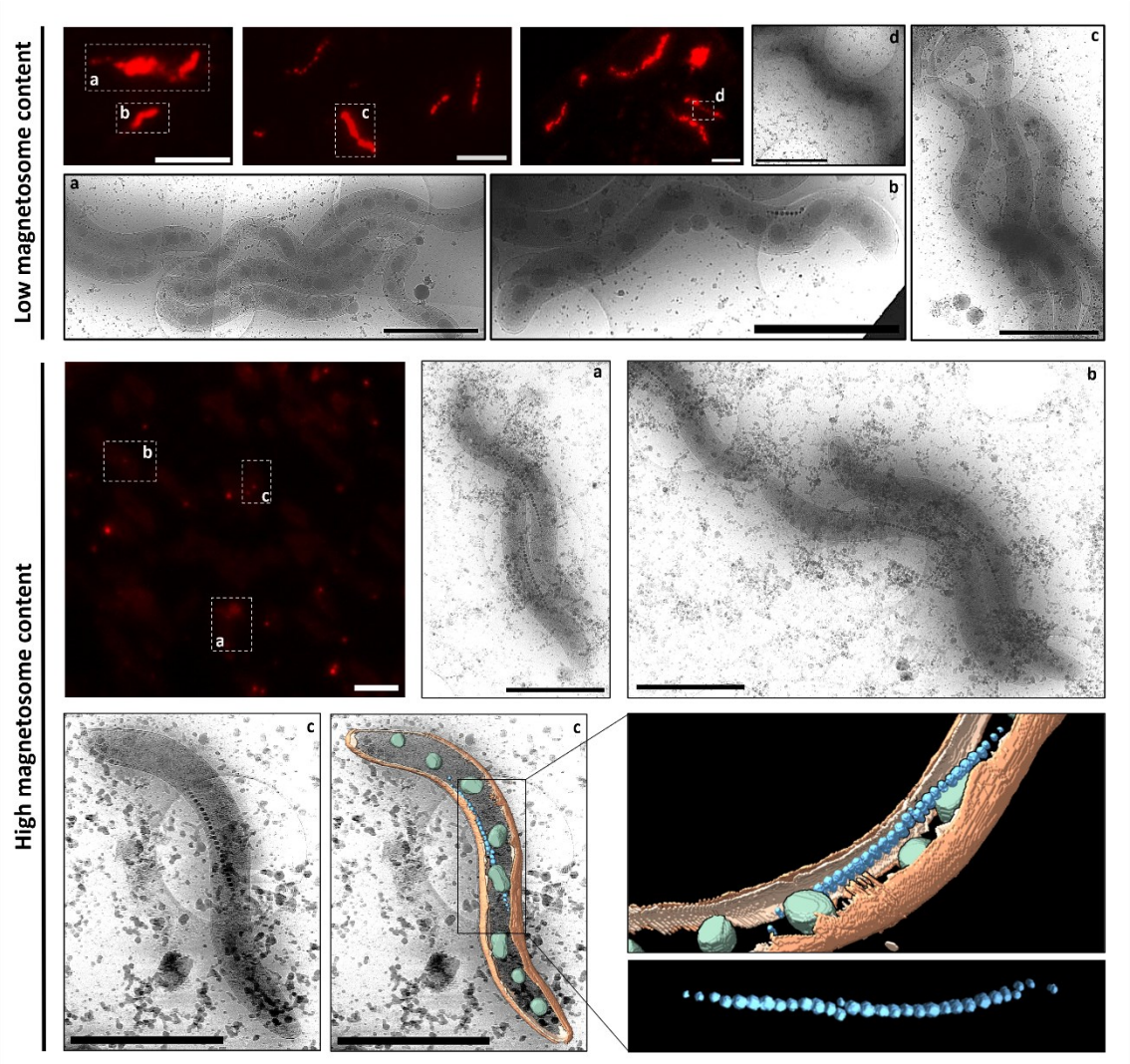

Figure 4.4. Comparison of intracellular ROS accumulation of MSR-1 cells containing high or low magnetosome content. Cells were stained with CellROX Deep Red fluorophore to detect ROS presence. CryoEM images of selected cells are matched to the corresponding cryo-fluorescence images as indicated by the same letter labels. A representative 3D volumetric representation of a highly magnetic cell is included. Magnetosome chain is coloured in blue, PHA granules in green, outer membrane in orange and inner membrane in light orange (**Movie 4.4**). Scale bar = 2 µm (cryoEM) and 10 µm (cryo-fluorescence).

exhibited high intracellular iron concentrations over time, did not show a significant correlation between total iron content and ROS accumulation. This lack of correlation demonstrates the efficiency of MSR-1's regulatory systems in managing high iron levels without apparent oxidative harm. In contrast, in aerobic conditions, a decrease in total intracellular iron content corresponded with an increase in ROS levels. This may result from a reduction in the number of magnetosomes per cell, thereby diminishing the capacity of MSR-1 cells to mitigate oxidative stress through magnetosome-associated ROS scavenging activity [37], [40]. Despite Fur acting directly as a global regulator responding to iron levels [268], oxidative stress (such as that caused by high oxygen conditions) can influence iron homeostasis and indirectly affect Fur activity. Cells might respond by more tightly regulating iron uptake and storage to minimize the availability of free iron that could participate in ROS generation. This response could hypothetically involve Fur-mediated pathways to ensure iron levels are kept within a safe range, even though Fur's primary direct response is to iron rather than to ROS or oxygen levels [244].

The correlation between labile Fe^{2+} (detected by PG-SK fluorescence) and ROS levels also varied notably depending on oxygen availability (**Figure 4.3F**). Under microaerobic conditions, no significant correlation was observed. However, under aerobic conditions, a clear inverse correlation was observed: lower Fe^{2+} levels, indicated by higher PG-SK fluorescence, were associated with increased ROS accumulation. This relationship can be explained by the Fenton reaction. Since PG-SK has a high affinity for Fe^{2+} but not for Fe^{3+} [269], its fluorescence increases as Fe^{2+} is oxidized and becomes less detectable by PG-SK, while ROS levels rise. Correlative microscopy images in **Figure 4.3H** further illustrate this situation, showing that magnetic cells exhibited low PG-SK and CRDR fluorescence, while non-magnetic cells exhibited high fluorescence.

Overall, these results suggests that magnetosomes likely play a significant role in mitigating oxidative stress and highlight the complex interplay between antioxidant mechanisms, iron homeostasis, and magnetosome biomineralization in MTB.

4.4. Conclusions

In this study, the effects of important stress factors - extracellular iron concentration and H_2O_2 - on MSR-1 cell physiology and magnetosome biomineralization were explored through the integration of advanced microscopy with high-throughput and elemental analysis methodologies (e.g. FCM, ICP-OES and cryoCLEM imaging). These techniques enable the capture of dynamic cellular responses in real-

time and at the single-cell level, providing a detailed view of how MSR-1 cells respond to such external factors. Our findings reveal distinct differences in how magnetosomes-producing (microaerobic cultures) and non-producing (aerobic cultures) MSR-1 cells manage magnetosome production, iron content, and oxidative stress under varying oxygen regimes. Under microaerobic conditions, cells maintained high levels of magnetosomes and intracellular iron, with minimal oxidative stress, whereas aerobic conditions led to reduced magnetosome production and intracellular iron content, alongside increased ROS levels. These results underscore the crucial role of magnetosomes in mitigating oxidative stress and highlight the complex interaction between antioxidant mechanisms, iron regulation, and magnetosome biomineralization. Additionally, the observed changes in MSR-1 cell morphology and viability exposed to external stress factors emphasize the importance of monitoring physiological changes to improve bioprocess efficiency and robustness, which is vital for advancing the production of high-quality magnetosomes. This is of utmost importance for future large-scale production and application of magnetosomes in biomedicine and biotechnology. Overall, this study not only contributes to the understanding of oxidative stress responses in MTB but also demonstrates the value of integrating cutting-edge analytical techniques to advance in the development of more consistent and efficient bioprocesses.

Chapter 5.

Evaluation of cell disruption technologies on magnetosome chain length and aggregation behaviour from *Magnetospirillum gryphiswaldense*

The content of this chapter has been adapted from the following publication:

"Evaluation of cell disruption technologies on magnetosome chain length and aggregation behaviour from *Magnetospirillum gryphiswaldense* MSR-1". M. Masó-Martínez, B. Fryer, D. Aubert, B. Peacock, R. Lees, G. A. Rance, M. W. Fay, P. D. Topham, A. Fernández-Castané. Front. Bioeng. Biotechnol., vol. 11, no. May, pp. 1–13, 2023, doi: 10.3389/fbioe.2023.1172457.

5.1. Introduction

Chemically-synthesized magnetic nanoparticles (MNPs) have been widely studied for their potential application in nanomedicine and biotechnology [99]. However, synthetic MNPs face various drawbacks, such as high toxicity, lack of biocompatibility and harsh conditions required for their synthesis [3]. Some of these issues can be remediated by adding extra steps in the synthesis process, but these often come at the expense of production complexity and increasing costs. Therefore, research interests are shifting towards finding more efficient and sustainable biomanufacturing approaches to synthesize biocompatible MNPs.

The discovery of the biological MNPs, termed '*magnetosomes*' back in the 1970s, attracted the attention of the scientific community for their potential to replace synthetic MNPs [21]. Magnetosomes are magnetic nanoparticles within the size range of 35-120 nm and are naturally produced by MTB [5]. Usually, magnetosomes are arranged in a needle-like chain and their main attributed function is to act as a geomagnetic navigation system. A typical magnetosome composition consists of an inorganic core (Fe_3O_4 or Fe_3S_4) enveloped in a lipid membrane bilayer containing transmembrane proteins [49]. Some of the unique properties of magnetosomes include their narrow

size distribution, high crystal purity, high heating capacity, facile functionalization, and high biocompatibility. These properties collectively make magnetosomes an attractive alternative to synthetic MNPs with great potential for biomedical, biotechnological and environmental application [218]. Unfortunately, the ability to implement a robust large-scale magnetosome biomanufacturing system has proven to be challenging despite the best efforts to enhance magnetosome yield [11], [219], [270]. The future widespread application of industrial magnetosome biomanufacturing is currently hindered by: (i) the limited understanding of magnetosome biomineralization; (ii) the identification of MTB growth and physiological bottlenecks [17], [18], [132]; (iii) the ability to produce magnetosome batches with the same structure, chain length and functionality (*i.e.* batch-to-batch reproducibility); and (iv) the development of characterization techniques allowing rapid assessment of magnetosomes preparation.

Magnetosomes have the potential to become the next generation of therapeutic agents but there is a critical need to scale-up the biomanufacturing process, whilst achieving homogeneous chain length preparation and preserving the envelope of embedded transmembrane proteins that can be used for functionalization purposes. The first step in the downstream process that compromises the size of magnetosome chains is cell disruption. Different lab-scale mechanical cell disruption techniques such as ultrasonication [83], [85], French Press [49], [153] or high-pressure homogenization [157], [158] are commonly used for MTB disruption thus rendering magnetosomes accessible for recovery. However, very few studies have been conducted to systematically compare different cell disruption treatments, and thus evaluate their efficiency and impact on the length and integrity of the isolated magnetosome chains [162], [271]. The integrity of the magnetosome chain is particularly relevant for certain applications, as variations in chain size and arrangement can lead to distinct characteristic and influence their magnetic properties [100], [271], [272]. Additionally, in biomedical and industrial applications, achieving uniform and stable magnetosome preparations is essential to ensure consistent performance and efficacy, irrespective of whether they consist of individual magnetosomes, long chains, or magnetosome aggregates.

In this study, we employ three nanoparticle (NP) characterization techniques—TEM, dynamic light scattering (DLS), and nano-flow cytometry (nFCM)—to evaluate the effect of three different cell disruption techniques on magnetosome chains. The combination of such complementary techniques allows one to obtain a holistic picture of the composition of the magnetosome preparation as each technique has its own advantages and disadvantages. For instance, TEM offers high size resolution but low throughput, whereas the opposite is observed in DLS analysis. nFCM was used for the first time to characterize magnetosomes and we have evaluated its potential to become a rapid quality assurance technique for magnetosome preparation. The combination of light scattering and fluorescence

detection from nFCM allows the facile collection of data to inform the particle size distribution, particle concentration and identification of sub-populations labelled with fluorescent markers, which makes nFCM a very powerful and innovative technique [168].

5.2. Materials and methods

5.2.1. Bacterial strains and culture conditions

Magnetospirillum gryphiswaldense MSR-1 was obtained from Deutsche Sammlung von Mikroorganismen und Zellkulturen GmbH (DSMZ, Germany). MSR-1 was grown in a 5-L Biostat B (Sartorius Stedim UK Ltd, Surrey, UK) bioreactor following a pH-stat strategy described elsewhere [11]. Briefly, MSR-1 cells were grown at 30°C, under microaerobic conditions (pO_2 < 1%.), in FSM without iron citrate at a pH of 7. The pH was maintained by automated addition of an acidic iron-rich feeding solution. Once the culture reached stationary phase, MSR-1 cells were harvested by centrifugation (4000 rpm, 20 min, 4°C) in a Heraeus Multifuge X1R centrifuge (Thermo Scientific, Massachusetts, USA). The supernatant was removed and the pellet was stored at -80°C until further use.

5.2.2. Cell disruption

MSR-1 biomass was thawed overnight at 4°C and cells were disrupted using three different methods: (i) enzymatic disruption (EZ); (ii) sonic probe disruption (SP); and (iii) high-pressure homogenization (HPH). Prior to disruption, MSR-1 biomass for HPH and SP samples were suspended in a HEPES-EDTA buffer solution (50 mM HEPES, 5 mM EDTA, pH 7.4) to a final concentration of 10% (w/v). High-pressure homogenizer disruption was conducted using a bench top CF1 Cell Disruptor (Constant Systems Ltd., Daventry, Northants, UK). Suspended cells were disrupted in a single pass at 10 kpsi at 4°C [273]. Sonic probe disruption was completed by sonicating the cells for 20 minutes at 4°C using 70% amplitude with a pulse setting of 1 second on / 1 second off using the Fisherbrand™ Model 120 Sonic Dismembrator (500 W, 20 kHz) (**Figure C3**). The enzymatic disruption protocol was adapted from the manufacturer's instructions. Briefly, cells were suspended (10% (w/v) with B-PER™ Complete Bacterial Protein Extraction Reagent (Thermo Scientific), which contained a mild non-ionic detergent and lysozyme, for 60 min at 25°C at 100 rpm.

5.2.3. Magnetosome purification

Regardless of the methodology employed to disrupt MSR-1 cells, magnetosomes were recovered following the same purification protocol adapted from Fernandez-Castane *et al.* [15]. The disrupted cell suspensions were subjected to magnetic separation using a NdFeB N45 magnet by performing at least a series of 10 washes. The magnet was placed vertically against the tube containing the cell homogenate for 30-45 min at 4°C, except for the first wash which was left overnight. The magnet attracts any magnetic material and cell debris remains in the suspension or sedimented at the bottom of the tube. Using a pipette, the MSR-1 cell debris fraction was carefully removed before adding 20 mL of fresh HEPES-EDTA buffer. Then, the solution was resuspended and left with the magnet for another 30-45 min. The same procedure was repeated 10 times except only 6 mL of HEPES-EDTA buffer was used to resuspend the magnetosomes in the final wash. To remove remaining impurities, ultracentrifugation of the recovered magnetosomes was performed using a Ti 70.1 Rotor on the Optima™ L-80 XP Ultracentrifuge (Beckman Coulter). One mL portions of the recovered magnetosomes were layered onto a 5 mL 60% (w/v) sucrose cushion using 10.4 mL Polycarbonate Bottles with Cap Assembly (Model 355603, Beckman Coulter, Indianapolis, United States) and ultracentrifuged at 45,000 rpm, 4 °C for 2.5 h. After centrifugation, the 'light' sucrose top phase was carefully removed using a Pasteur pipette, and the 'heavy' fraction at the bottom containing magnetosomes was resuspended in PBS (pH 7.4). Samples were subsequently collected and stored at 4°C in a reducing environment to avoid magnetosome oxidation until further analysis.

5.2.4. Treatment of purified magnetosomes

Purified magnetosomes were analysed by TEM, DLS and nFCM. A fraction of these purified magnetosome solutions were split and used to obtain (i) single magnetosomes with intact membrane and (ii) membrane-stripped magnetosomes. To obtain single magnetosomes, the preparations were vortexed for 1 min and sonicated for 5 min in a Clifton SW1H Ultrasonic bath (200 W, 37 kHz). Membrane-stripped magnetosomes were generated as described elsewhere [274]. Briefly, purified magnetosomes were treated with a series of detergents and organic solvents and after each treatment, magnetosomes were isolated from non-magnetic organic debris using a NdFeB N45 magnet as follows: (i) 20 s sonication of PBS-resuspended magnetosomes in an ultrasonic bath; (ii) overnight resuspension of magnetosomes in a 1% SDS solution at 60°C; (iii) sonication of magnetosomes in phenol solution (pH 8) for 2 h at 60°C in an ultrasonic bath; (iv) chloroform-resuspension of magnetosomes for 2 h at 60°C; and (v) sonication of magnetosomes resuspended in a 1 M NaOH

solution for 1 h at 60°C in an ultrasonic bath. Subsequently, membrane-stripped magnetosomes were resuspended in PBS.

5.2.5. Transmission electron microscopy

TEM was used to image magnetosome chains. Magnetosome preparations (2 µL) were drop cast on a graphene oxide on lacey carbon 300 mesh copper supported grid (GOLC300Cu50, EM Resolutions, Sheffield, UK) and vacuum-dried before analysis. TEM images were obtained using a JEM-2100 F microscope (JEOL, Herts, UK) operating at 200 kV and equipped with a Gatan Orius CCD camera (Pleasanton, USA). To determine the length distribution of the purified magnetosome chains, 100 magnetosome chains per sample were selected randomly and the number of magnetosome units of each chain was counted. Magnetosome chains were also classified into three different categories: short (1-5 magnetosome units), medium (6-10 magnetosome units) and long chains (>11 magnetosome units). Other relevant parameters, such as mean values and cumulative frequency distributions were also calculated and analysed for each sample. From cumulative frequency data, relevant percentiles, $P_{0.5}$ ($L_{50,}$ median) and $P_{0.1}$ (L_{10}), were calculated. Microscope images of the pre-disrupted MSR-1 cells were analysed as described above.

5.2.6. Dynamic light scattering

DLS was used for the characterization of the size distribution of the purified magnetosome solutions. The size of particles, as hydrodynamic diameter, is calculated from the translational diffusion coefficient related to the velocity of Brownian motion by using the Stokes-Einstein equation [275]. Each sample was analysed using a Zetasizer Nano-ZS (Malvern Panalytical, Worcs, UK) in a standard capillary cell with a backscattering angle of 173°. PBS was used as the suspension buffer (viscosity 0.8872 cP, 1.330 refractive index, 25°C). A total of 6 measurements per sample were performed and average size values are presented.

5.2.7. Determination of iron concentration

ICP-OES (Thermo Scientific iCAP 7000) coupled to a Teledyne CETAC ASX-520 Random Access Autosampler was used to determine the iron concentration of magnetosome preparations at a wavelength of 259.94 nm. 100 µL of purified magnetosome preparation were used and digested with

500 µL of nitric acid (70% v/v) solution. Samples were prepared in triplicate, incubated at 98°C for 2 h with shaking at 300 rpm prior to be analysed by ICP-OES.

5.2.8. Flow cytometry

Samples were taken before and after cell disruption, diluted in PBS and immediately analysed in a BD Accuri C6 Flow Cytometer (Becton, Dickinson and Company, Oxford, UK). Samples were stained with Syto®62 (0.4 µM), a permeant DNA dye, to stain MSR-1 cells to determine cell disruption efficiency. Syto®62 was excited with a 640 nm solid-state laser and detected through a 675/25 BP filter (FL4-A).

5.2.9. Nano-Flow Cytometry

A NanoAnalyzer U30 instrument (NanoFCM Inc., Nottingham, UK) equipped with dual 488/640 nm lasers and single-photon counting avalanche photodiode detection (SPCM APD) was used for simultaneous detection of side scatter (SSC) and fluorescence of individual particles. Bandpass filters allowed for collection of light in specific channels (SSC - 488/10; FL1 – 525/40; FL2 – 670/30). HPLC-grade water served as the sheath-fluid via a gravity feed, reducing the sample core stream diameter to ~1.4 µm. Measurements were taken over a one-minute interval at a sampling pressure of 1.0 kPa, maintained by an air-based pressure module. All samples were diluted in PBS to attain a particle count within the optimal range of 2,000 – 12,000/min. During sample acquisition, the sample stream is fully illuminated within the central region of the focused laser beam, resulting in approximately 100% detection efficiency, which leads to accurate particle concentration measurement via single-particle enumeration. The concentration of samples was determined by comparison to 250 nm silica nanoparticles of known concentration to calibrate the sample flow rate. Particle sizing was carried out according to standard operating procedures using a proprietary 4-modal silica nanosphere cocktail (NanoFCM Inc., S16M-Exo – 68, 91, 113 and 155 nm). Using the NanoFCM software (NanoFCM Profession V1.8), a standard curve was generated based on the side scattering intensity of the different silica particle populations. In order to detect the whole particle size distribution of the different samples, the laser was set to 10 or 20 mW and the SS (side scatter) decay to either 10% (40 – 200 nm particle range) or 0.2% (200 – 1000 nm particle range). Data processing was handled within the nFCM Professional Suite v1.8 software, with dot plots, histograms, and statistical data. Gating within the software allows for proportional analysis of subpopulations separated by fluorescent intensities with size distribution and concentration available for each sub-population. To homogenize magnetosome preparations, to avoid clumps and aggregates, and to obtain a uniform particle concentration, the

solutions were subjected to 5 s vortexing and 10 s gentle sonication using a Clifton SW1H Ultrasonic bath.

5.2.9.1. Magnetosome labelling

Purified and treated preparations of single magnetosomes were used to conduct this experiment. To avoid aggregates, samples were homogenized by vortexing and sonication as described above every time sample manipulation was required (e.g. diluting, staining). Purified magnetosome preparations were labelled using the fluorophore CellMask™ Deep Red (Invitrogen™, UK), which is a lipid membrane stain, adapting a protocol described elsewhere [276], [277]. To determine the optimal concentration of CellMask™ Deep Red, different fluorophore concentrations were used (1.25, 6.25, 20, 25, and 100 µg/mL). Incubation conditions were maintained constant: after dye was added, samples were incubated for 30 min at room temperature. After 15 min of incubation, samples were again briefly sonicated and vortexed. Three replicates were prepared per each staining condition.

5.2.10. Statistical analysis

Unless otherwise indicated, results are represented as means ± standard error of the mean. One-way analyses of variance (ANOVA) followed by Bonferroni's post-test were performed to compare the different groups. The cut-off value for statistical significance was set at $P < 0.05$.

5.3. Results and discussion

In this study, the effect of cell disruption treatment on the length and integrity of the magnetosome chain was studied. Three different cell disruption treatments (EZ, SP and HPH) and three different magnetosome characterisation techniques (TEM, DLS and nFCM) were employed to determine magnetosome chain length from MSR-1 cells cultivated at relatively high cell densities.

5.3.1. Bioreactor cultures

MSR-1 was cultured in a 5-liter bioreactor using a pH-stat strategy, where the pH was automatically maintained by the controlled addition of an acidic feeding solution, to ensure stable growth conditions and avoid nutrient limitations. Initially, no oxygen supply was provided until the pO_2 decreased to 0.1%. At this point, air supply was initiated and manually adjusted by increasing the airflow in response to

the cellular oxygen demand. This aeration strategy enables MSR-1 to start growing rapidly under aerobic conditions, then gradually adapt to the decreasing pO_2, and finally resulting in optimal microaerobic conditions necessary for magnetosome biomineralization [11]. As the biomass increased, the pH raised; however, the automated addition of the acidic feeding solution - containing carbon source and other nutrients such are iron - maintained the optimal pH (set point 7). As illustrated in **Figure 5.1**, the fermentation process lasted over 59 hours, reaching a maximum OD_{565} of 8.5 and yielding 2.3 g DCW. C_{mag} values and the total intracellular iron concentration increased following the initiation of magnetosome production at around 10 h and reached maximum values of 2.4 and 10.6 mg Fe/g DCW, respectively. The colour of the fermentation broth also progressively darkened throughout the experiment, indicating an increase in magnetosome formation (**Figure C1**). **Figure C2** illustrates the time profile of key process parameters, including pO_2, feeding rate, temperature, pH, and stirring speed during the fermentation.

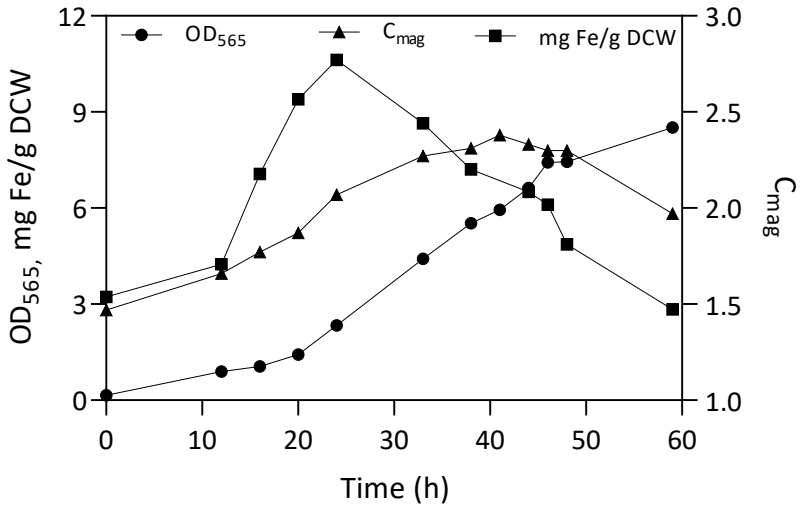

Figure 5.1. Cellular growth (OD_{565}), cellular magnetic response (C_{mag}) and intracellular iron content (mg Fe/g DCW) profile of MSR-1 grown in a 5L bioreactor under pH-stat mode. DCW = Dry cell weight.

5.3.2. Disruption efficiency

Breaking down the cell membrane is necessary to release the intracellular contents and thus extract and isolate magnetosome chains. To determine the efficiency of each disruption treatment, cells were stained with Syto®62 and analysed by FCM. Efficient magnetosome recovery requires a high disruption efficiency, but to accomplish this, the magnetosome chain integrity might be compromised. **Figure 5.2A** shows that all three disruption techniques exhibit high efficiency (>89%) in terms of cell lysis. This is due to the fact that all three techniques and operation conditions were carried out under optimal

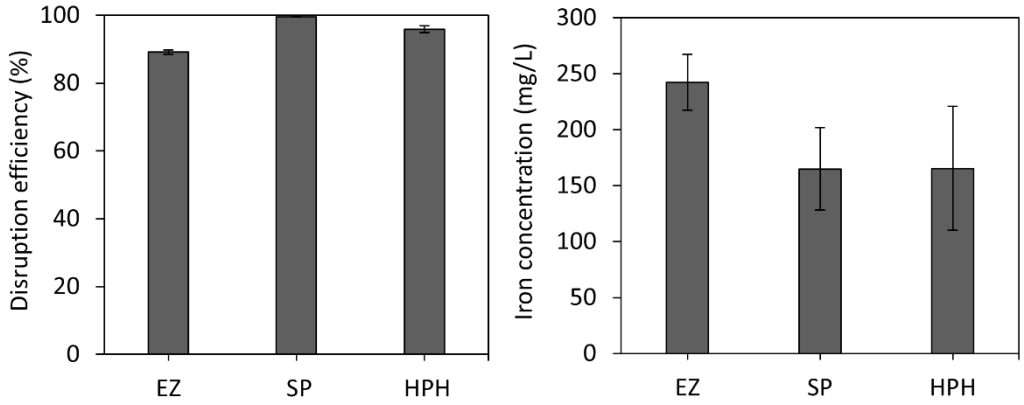

Figure 5.2. (A) MSR-1 cell disruption efficiencies of EZ, SP and HPH cell disruption treatments. (B) Estimation of iron concentration of purified magnetosome solutions. Error bars represent standard deviation of triplicates. EZ (enzymatic), SP (sonication probe) and HPH (high-pressure homogenizer) treatments.

conditions for efficient MSR-1 disruption. As no significant differences in cell disruption efficiencies were observed, other factors, such as time, scalability or availability of resources, must be considered and are further discussed in this work. EZ treatment displayed the lowest efficiency (89%) among all treatments. As expected, SP treatment resulted in the highest disruption efficiency (>99%) followed by HPH treatment (96%). Previous work done by Li and co-workers reported a similar disruption efficiency of 92% using a high-pressure homogenizer and also reported that it was easier to disrupt MSR-1 cells when they were harvested at the exponential phase rather than when cells were in stationary phase [273]. Cell wall strength, shape and size can play an important role in cell disruption efficiency, especially in high-pressure homogenisation [278].

Usually, ICP-OES or other spectroscopic techniques are commonly used to obtain a quantitative estimation of magnetosome content. In this case, the analysis of iron content of the purified magnetosome solutions using ICP-OES also provided information regarding the cell disruption efficiency. **Figure 5.2B** shows that magnetosome samples isolated using SP and HPH contain similar iron content, however, for those samples using EZ higher iron levels were observed. All steps after MSR-1 cell disruption were fixed to evaluate solely the effect of the disruption step. EZ disruption was the least efficient cell disruption method, which indicated that a higher number of cells remained intact after the disruption and purification processes compared with the other treatments. In fact, whole cells were observed in some of the EZ TEM images (**Figure C4**) whereas the presence of whole cells was not observed in TEM images from SP and HPH samples. The presence of whole cells in the EZ magnetosome preparation could explain the superior iron levels in those samples. Until recently, it was believed that 99.5% of the intracellular iron content of MTB cells corresponded to magnetite crystals [49]. However, recent studies estimated that only 25-45% of the bulk cellular iron corresponded to magnetite [118], [119]. The remaining intracellular iron is believed to be used to carry out general biochemical reactions that require iron. Therefore, all the intracellular iron content of

undisrupted cells in the EZ treatment that do not correspond to magnetite was added up to the final iron concentration.

The EZ commercial kit used contained lysozyme in combination with a mild non-ionic detergent. Lysozyme had previously been used to study periplasmatic and cytoplasmatic fractions in MTB cells [160], [161], but very few studies have used this enzyme for magnetosome extraction [162]. French press [49], [279], high-pressure homogenization [15], [158], [280] or sonication [150], [151] are more commonly used for disruption of MTB due to their simplicity and cost-effectiveness. The effect of these disruption techniques on magnetosome chains has not been studied in detail yet, but large aggregates have been observed when the magnetosome membrane is removed. Extensive ultrasonication time or enzymatic treatments can cause the loss of the magnetosome membrane [100], [162], which prevents a homogeneous particle distribution. Increasing the number of passes in HPH treatment also enhances chain breakage [273]. Very little has been reported in terms of systematic and comparative cell disruption studies in MTB, hence the importance of the work herein.

5.3.3. Effect of cell disruption method on magnetosome chain length and aggregation state

The effect of cell disruption treatment on magnetosome chain length was first examined by TEM (**Figure 5.3**). Micrographs of the purified magnetosome solutions were analysed to assess chain integrity and length. Up to 100 magnetosome chains per treatment were randomly selected and the number of magnetosome units in each chain was quantified. The variation of the mean values of magnetosome chain length revealed the existence of significant differences among some of the disruption treatments (**Figure 5.3D**). EZ treatment generated statistically significant shorter magnetosome chains compared with the rest of the treatments (one-way ANOVA with Bonferroni test, $P < 0.05$). However, there are no significant differences between SP and HPH treatments or between HPH and pre-disrupted chains. As **Figure 5.3A-C** shows, the distributions of magnetosome chain sizes in all the disruption treatments are broad, displaying heterogeneity in the magnetosome preparations and the existence of different chain-size populations.

Table 5.1 classifies magnetosome chains in three different groups based on their length: short, medium, and long. Considering that 80% of the magnetosome chains were long before cell disruption, it can be observed that cell disruption caused chain cleavage in all three treatments as the prevalence of long chains was reduced by at least 15% in each case (**Table 5.1**). As a result of chain breakage, short chains which were not present in pre-disrupted MSR-1 cells were detected after cell disruption. HPH treatment seemed to be the technique that generated less damage to the chains, yielding the lowest

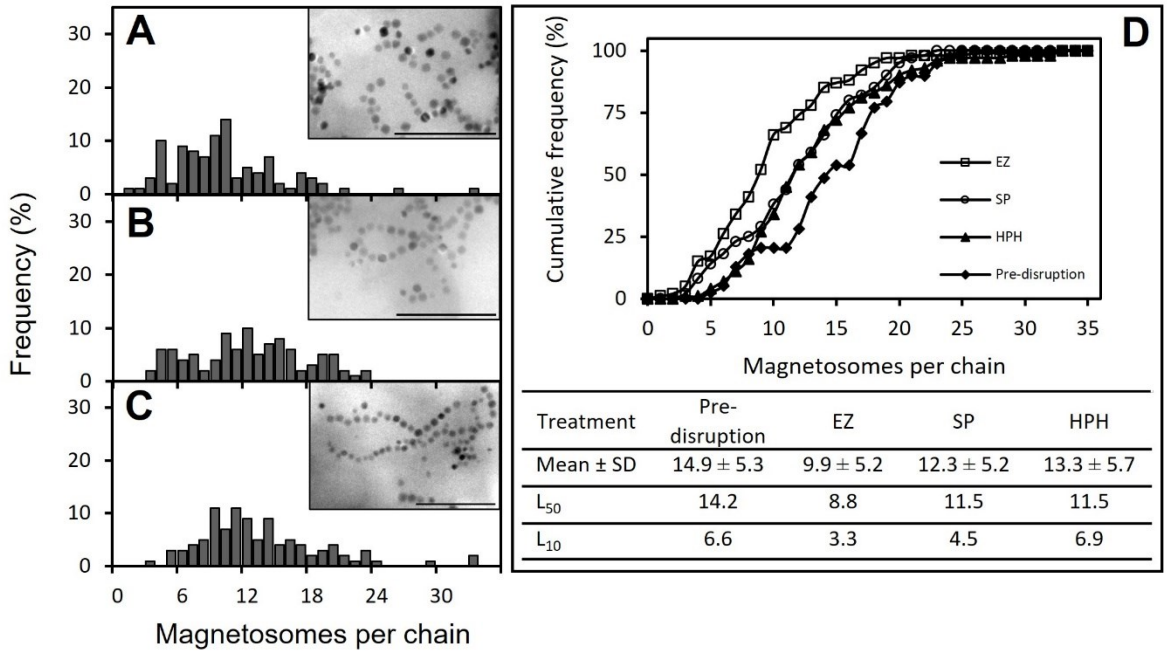

Treatment	Pre-disruption	EZ	SP	HPH
Mean ± SD	14.9 ± 5.3	9.9 ± 5.2	12.3 ± 5.2	13.3 ± 5.7
L_{50}	14.2	8.8	11.5	11.5
L_{10}	6.6	3.3	4.5	6.9

Figure 5.3. Transmission electron microscopy (TEM) analysis of purified magnetosome chains *of M. gryphiswaldense* MSR-1. (A-C) Magnetosome chain length frequency distribution plots and TEM images of purified magnetosome preparations in which (A) enzymatic treatment, (B) sonication and (C) high-pressure homogenizer were employed to disrupt MSR-1 cells. (D) Cumulative frequency curves of magnetosome chain length before and after magnetosome purification. The table includes the mean values of the length of the magnetosome chains pre- and post- cell disruption, as well as relevant statistical parameters, L_{50} and L_{10}. EZ (enzymatic), SP (sonication probe) and HPH (high-pressure homogenizer) treatments. Scale bar = 500 nm.

short-chain frequency (4%) and the highest long-chain frequency (66%) [15], [271], [273]. The results also revealed that EZ treatment most significantly affected the chain integrity as only 34% of the chains were considered long and 17% short. These results suggest that the enzymatic cocktail used could be compromising the cell membrane as well as the magnetosome membrane. In addition, MamK, the actin-like protein that arranges magnetosomes in a chain, could also be affected by the EZ treatment as it has been seen that actin polymerization can be affected by the presence of detergents [281]. The EZ kit used contained a mild non-ionic detergent that may contribute to MamK degradation, causing more magnetosome chain cleavage.

Table 5.1. Classification of magnetosome chains length frequency (%) into short, medium or long chains before (pre-disruption) and after magnetosome purification based on TEM analysis.

		Short	Medium	Long
Pre-disruption		0	20	80
Disruption Treatment	EZ	17	49	34
	SP	14	24	62
	HPH	4	30	66

Cumulative frequency is used to determine the number of observations that lie above or below a particular value in a data set. Determination of relevant cumulative frequency percentiles such as L_{50} (median) and L_{10} are particularly useful in cases like this study in which the distribution of events is asymmetric, as these percentiles are less sensitive to extreme values and provides a more precise estimate of the size distribution. Cumulative frequency curves (**Figure 5.3D**) indicated that SP and HPH followed similar chain length distributions, whereas the EZ treatment deviated from them by displaying shorter magnetosome chains. SP and HPH L_{50} values showed no differences between them (11.5 magnetosome per chain), but smaller percentile values such as L_{10} revealed disparities in chain length between these two magnetosome preparations (4.5 and 6.9 magnetosomes per chain, respectively), which suggested the presence of higher quantities of short chains in the SP preparation. It is known that uncoated or partially coated magnetosomes are prone to self-aggregation [150]. Previous studies revealed extensive chain breakage and magnetosome agglomeration as a direct consequence of magnetosome ultrasonication over an extended period of time [15], [151]. Nakamura and co-workers compared ultrasonication and lysozyme disruption treatments by studying the particle sizes as well as magnetosome membrane thickness [162]. TEM images revealed that the degree of chain aggregation in the EZ preparation was higher than in the SP preparation. In addition, magnetosome membrane thicknesses in lysozyme-treated magnetosomes were thinner than ultrasonicated magnetosomes, indicating the effect of the EZ treatment not only on MTB cells but also on the magnetosome membrane [162]. Nakamura combined the lysozyme treatment with either the addition of SDS, which can denature some Mam proteins [282], or incubation with NaOH for 12 h, which can be time consuming. The MTB species used is not specifically identified in their study either, so to our knowledge, our study is the first one to use a lysozyme treatment on MSR-1 for cell disruption purposes.

Powerful techniques, such as TEM, allow the determination of the exact number of magnetosome crystals per chain and the study of the chain and crystal morphology. However, this technique only scrutinizes a small fraction of the sample, hence there is a clear need to combine this with different

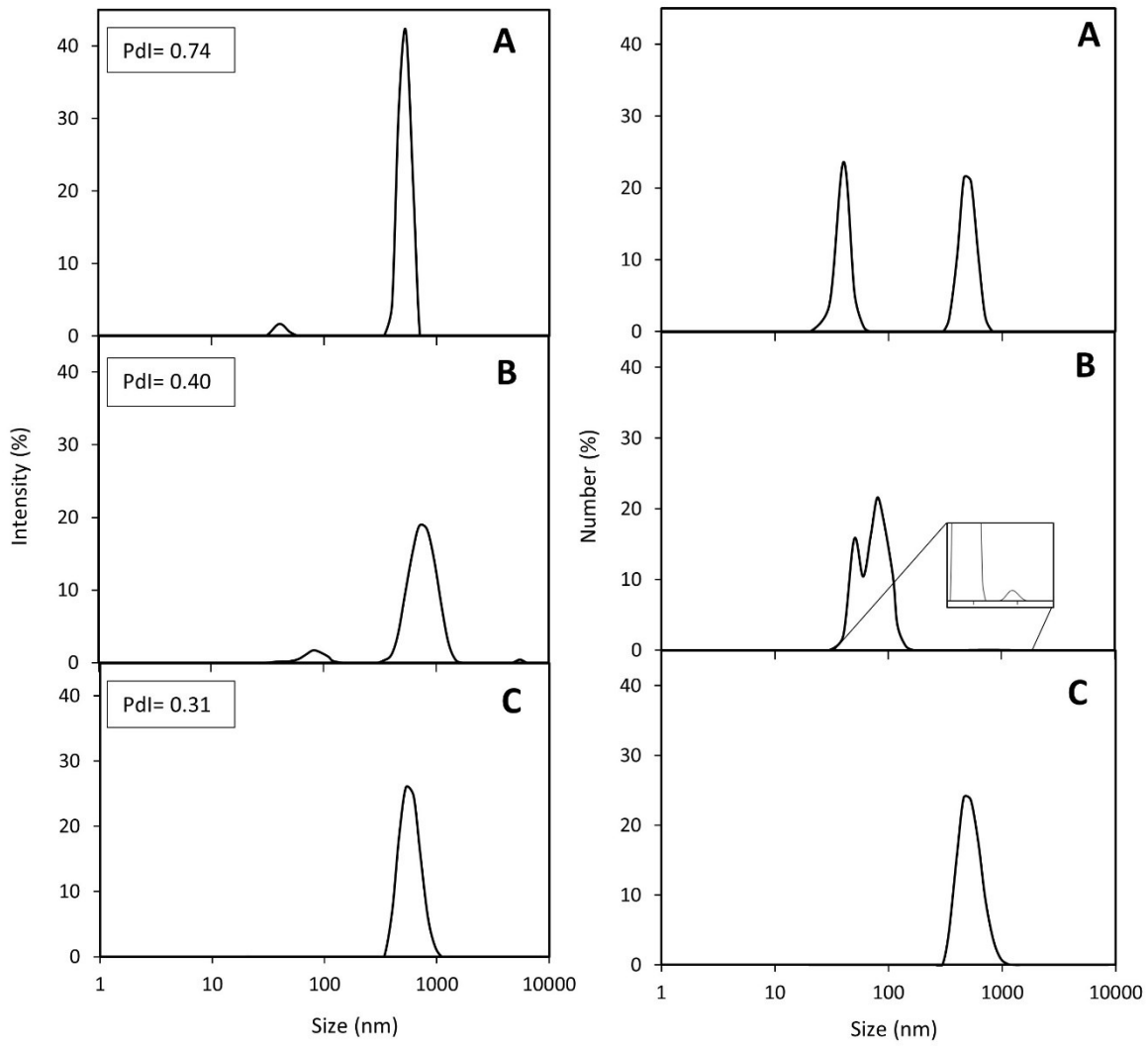

Figure 5.4. Dynamic light scattering (DLS) analysis of purified magnetosome chains extracted from *M. gryphiswaldense* MSR-1. Intensity and number distributions of purified magnetosome solutions obtained from disrupting MSR-1 cells using either (A) enzymatic, (B) sonication or (C) high-pressure homogenization treatments. Polydispersity index (PdI) values for each magnetosome preparation are included.

techniques to obtain a broader picture. In this study we used DLS and nFCM to address the limitations of TEM analysis. One advantage of employing DLS is that this technique can analyse the whole preparation and study the particles behaviour in solution in a short period of time. DLS and TEM results are often complementary to each other but, given the two techniques fundamentally measure attributes such as size in different ways, they do not always directly correlate with one another. For instance, DLS provides an estimate of the average length/size of the chains as a hydrodynamic diameter; as this assumes a spherical morphology, it cannot readily account for the absolute shape of the chains (e.g., curved, straight, closed loops, agglomerates). Moreover, as they are in suspension, magnetosomes are free to move, rotate and interact with each other, providing an opportunity to study aggregation dynamics in real time [283]. **Figure 5.4** shows the intensity and number distributions of the three different magnetosome solutions. In both distributions, the same peaks can be observed.

Number distributions emphasize the species with highest number of particles (usually smaller particles) whereas intensity distributions highlight the species with the largest scattering intensity (usually the larger particles), hence the difference in height of the peaks. Since the particle size distribution of the magnetosome preparations produced in this work is not narrow, the presence of larger particles, such as aggregates or long chains, will contribute to an increase in light scattering, shifting the measured particles size towards larger values [284]. While analysis of HPH (**Figure 5.4C**) only resulted in one peak, EZ (**Figure 5.4A**) and SP (**Figure 5.4B**) bimodal size distributions indicate the presence of two magnetosome populations: one consisting of short chains or single magnetosomes and the other of long magnetosome chains [285], [286]. The higher prevalence of short chains in EZ and SP treatments compared to HPH is consistent with TEM results (4% HPH, 14% SP, 17% EZ frequency of short chains) (**Table 5.1**). The polydispersity index (PdI) of a solution measures the uniformity of particle sizes in a solution, with values closer to 1 generally indicating higher polydispersity. The high PdI of the EZ magnetosome preparation (PdI=0.74) (**Figure 5.4**) reflects the existence of a broader size distribution and indicates that the peak corresponding to single magnetosomes might represent a much larger population of short magnetosome chains than the one from SP treatment. Our results show that the chain integrity and agglomeration can be tuned as a function of the cell disruption technique, potentially impacting their suitability for specific applications. For some applications in which single magnetosomes are preferred or when the magnetosome membrane needs to be stripped to cover the magnetite crystals with different polymers, preserving chain length is less relevant [103], [274], [287]. Therefore, the chain cleavage effect of EZ treatment is not concerning in these cases. For other applications, such as alternative magnetic field cancer therapy [100] or magnetic hyperthermia treatment of tumours [271], magnetosome chains are more effective than using single magnetosomes. Other studies reported the benefits of using clustered magnetosomes as contrast agents for magnetic particle imaging instead of linear chains [272].

Scalability, time consumption and the cost of the different cell disruption treatments, among other factors, are also important elements to consider when determining the optimal magnetosome downstream processing for each intended application. SP is typically used in laboratories because of its simplicity, low operational costs and ease of use to treat small volumes [148]. HPH treatments are more effective and easier to adapt for large-scale processes but usually require higher energy input [288], contrary to EZ treatments, which require less energy consumption. The possibility of scaling-up is feasible for all three technologies in terms of industrial equipment; however, SP is usually less scalable and EZ generates higher costs for long term use on an industrial scale [289]. One advantage of the EZ treatment over SP and HPH is that heat is not generated while operating and does not require a refrigeration system to avoid sample damage [290]. At smaller scale, time is not that detrimental as

working with smaller volumes and lower cell concentrations usually ease the process. However, time costs and the amount of personnel needed to operate the system is more important at industrial scale when choosing the preferred disruption method as it will significantly contribute to the final costs of the process.

5.3.4. Suitability of nanoflow cytometry analysis for the characterisation of magnetosome preparations

Conventional characterization techniques such as TEM and DLS are powerful and commonly used for nanoparticle characterization studies, yet they can be time consuming and have a low detection sensitivity, respectively. In this study, we assessed nanoflow cytometry as a tool for rapid characterisation of magnetosome preparations with high sensitivity, which, to the best of our knowledge, has never been used before. The detection of nanoparticles by scatter and fluorescence allows the capture of real time data of nanoparticle size populations, size distribution, concentration and biochemical properties.

5.3.4.1. Effect of ultrasonication on magnetosomes concentration

Magnetosome preparations were diluted to be within the optimal particle count range of 2000-12,000/min. Due to the nature of the samples, dilution to suitable and uniform concentrations proved to be difficult. If the solution is not properly resuspended when diluting, magnetosome aggregates can be taken from the sample, and later when they are disaggregated the concentration increases. To solve this problem, a protocol was established in which samples were vortexed for 5 s, sonicated for 10 s, and immediately diluted or analysed before aggregates started to form. Following this methodology, data obtained for particle concentration was more stable and reproducible. If samples are sonicated too many times or for too long, it can affect the integrity of the magnetosome membrane, which can lead to the formation of more aggregates and cause constant changes in sample concentration [150].

5.3.4.2. nFCM analysis of the effect of cell disruption on magnetosome chains

The effect of cell disruption treatment on magnetosome chain length and the particle concentration of each preparation was examined by nFCM. To detect all magnetosome chain sizes, different laser settings were required to distinguish smaller particles (40-200 nm) from larger particles (200-1000 nm). nFCM particle concentration results revealed a vast difference in sample concentration when the

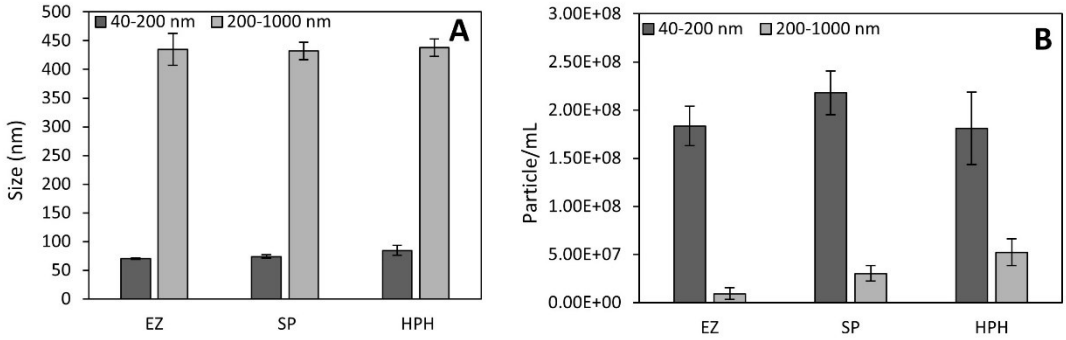

Figure 5.5. (A) MSR-1 magnetosomes chain size mean values and (B) particle concentrations of magnetosome preparations measured by nFCM using a smaller (40-200 nm) and larger (200-1000 nm) particle detection range. Each sample was analysed for 1 minute by nFCM and the number of events collected ranged from 5000 to 6000 depending on the sample. Error bars represent the standard deviation of triplicates. EZ (enzymatic), SP (sonication probe) and HPH (high-pressure homogenizer) treatments. nFCM = Nano-flow cytometry.

preparations were analysed using the small or the large particles detection ranges (**Figure 5.5B**). For the smaller particles range, the concentrations obtained were much higher than for the larger particles. EZ, SP and HPH samples were 20, 7 and 3 times more concentrated when measured using the smaller particles detection range than when using the large particles range, respectively. The three-fold particle concentration difference of the HPH preparation compared to the 20-fold difference of the EZ sample indicated the presence of a higher amount of short magnetosome chains from the EZ conditions, which matched the 4% and 17% short magnetosome chains measure from TEM results, respectively (**Table 5.1**). However, the EZ preparation showed the lowest concentrations among all three treatments. Magnetosomes with damaged or stripped membranes tend to aggregate to form clusters, which are not suitable for nFCM analysis [150], [151]. When analysing membrane-stripped magnetosomes, clusters larger than 1 µm were observed and impeded the analysis with nFCM. Therefore, if EZ cell disruption affects not only the cell membrane but the magnetosome membrane

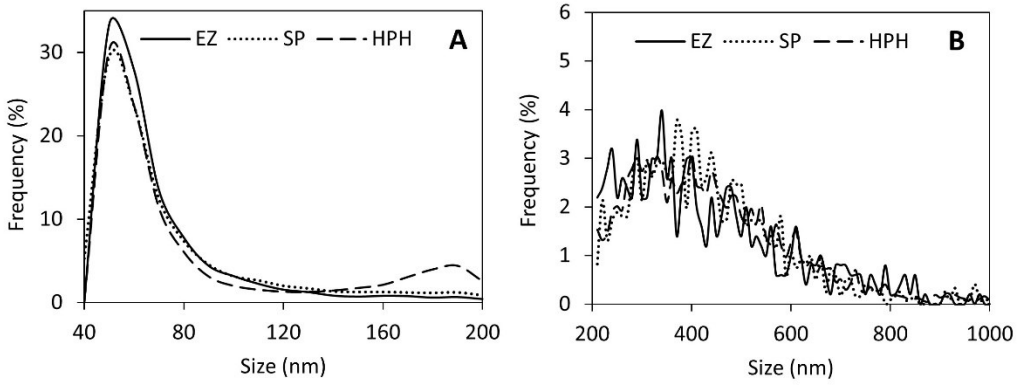

Figure 5.6. nFCM analysis of MSR-1 magnetosome chain size distributions using different detection ranges for (A) smaller particles (40-200 nm) and (B) larger particles (200-1000 nm). Enzymatic (EZ), sonication (SP) or high-pressure homogenization (HPH) treatments.

too, membrane-stripped magnetosomes cannot be detected during nFCM analysis, which explains the decrease in the overall EZ particle concentration [162].

Particle size distribution plots (**Figure 5.6**) did not show significant differences among the three different disruption treatments. Only the small particles plots (**Figure 5.6A**) exhibited a clear peak around 60 nm, which likely corresponded to single magnetosomes. Mean size values (**Figure 5.5A**) did not show significant differences among the treatments either (one-way ANOVA, $P < 0.05$). The results suggest the better suitability of nFCM to characterize single magnetosomes than longer magnetosome chains. In addition, the necessity of having to acquire two size ranges (40-200 nm and 200-1000 nm) and the sample preparation protocol may bias the actual size distributions as well as the particle concentrations of the different magnetosome preparations, which may represent a disadvantage over other similar techniques such as Nanoparticle Tracking Analysis (NTA) [15]. nFCM is a reliable technique to determine nanoparticle concentrations but due to the heterogeneity in the magnetosome chain length and the nature of the technology, this technique is not suited to characterize the size distribution of untreated magnetosome preparations. Individual membrane-encapsulated magnetosomes have a larger surface area-to-volume ratio, which might be an advantage for certain applications [291]. **Table 5.2** shows a summary of all the results obtained using the different

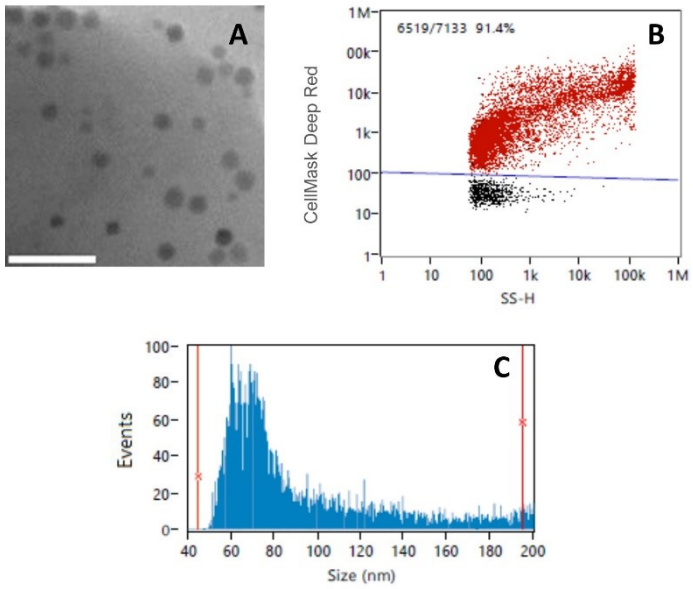

Figure 5.7. (A) Transmission electron microscopy (TEM) image of single magnetosomes. Example of (B) CellMask™Deep Red-stained magnetosomes and (C) size distribution of single magnetosomes analysed by NanoFCM Profession V1.8. In (B), the line represents the threshold separating magnetosomes stained by CellMask™ Deep Red from the unstained ones. Scale bar = 200 nm.

characterization and disruption techniques.

Table 5.2. Summary of the magnetosome preparation characterization results for each disruption technique. MS = magnetosomes; TEM = Transmission electron microscopy; DLS = Dynamic light scattering; PdI = Polydispersity index; nFCm = Nano-flow cytometry; EZ = Enzymatic disruption, SP = Sonic probe disruption; HPH = High-pressure homogenization.

		EZ		SP		HPH	
Disruption efficiency (%)		89.2 ± 0.6		99.6 ± 0.2		95.9 ± 1	
TEM	MS per chain	9.9 ± 5.2		12.3 ± 5.2		13.3 ± 5.7	
DLS	PdI	0.74		0.40		0.31	
	Intensity Peak (nm)	Peak 1	Peak 2	Peak 1	Peak 2	Peak 1	
		40	530	80	830	530	
nFCM	Particle Mean Size (nm)	40 – 200 nm	200 – 1000 nm	40 – 200 nm	200 – 1000 nm	40 – 200 nm	200 – 1000 nm
		74.34 ± 1.36	406.37 ± 36.75	77.11 ± 0.66	404.63 ± 15.97	100.44 ± 7.43	414.66 ± 17.41
	Particle/mL	$1.84x10^8$	$9.27x10^6$	$2.18x10^8$	$3.03x10^7$	$1.81x10^8$	$5.23x10^7$

5.3.4.3. nFCM analysis as a promising tool for characterising fluorescent magnetosomes

CellMask™ Deep Red has been previously used to stain both cells and extracellular vesicle lipidic membranes [276], [292]. In this study, we tested a range of different fluorophore concentrations to determine the optimal magnetosome membrane staining conditions using nFCM technology. It was previously established that nFCM is best suited for single magnetosomes, therefore, the 40-200 nm detection range and single magnetosomes were employed for this analysis (**Figure 5.7**). **Figure 5.8A** showed the fluorescence positivity of CellMask™ Deep Red stained magnetosomes. Over 90% of the magnetosomes were successfully labelled, and the optimal dye concentration was found to be at 20 µg/mL reaching 100% of stained magnetosomes. For higher concentrations, fluorophore saturation caused a fluorescence positivity decrease [261]. When every molecule is consistently in an excited state, fluorophore saturation can occur, in which an increase in excitation light does not result in a proportional increase in fluorescence emission [293]. **Figure 5.8B** showed similar particle concentrations between stained and unstained magnetosomes preparations, proving the capacity of CellMask™ Deep Red to specifically stain the magnetosome membrane. The successful detection of labelled magnetosomes shows the promising capacity of this technique to be used as a quality assurance tool for magnetosome preparations. In future studies, being able to directly quantify fluorescently labelled magnetosomes using nFCM will be advantageous for a wide range of different applications (e.g. identification different magnetosome populations, immunofluorescence studies or detection of fluorescent recombinant proteins expressed on the magnetosome surface) [294]–[296].

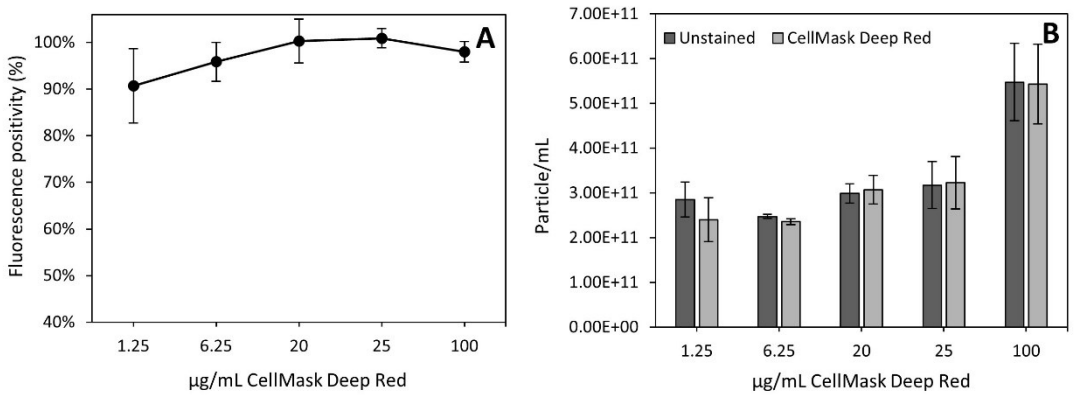

Figure 5.8. nFCM analysis of magnetosome labelled using CellMask™ Deep Red lipophilic dye. (A) Percentage of positive fluorescently labelled magnetosomes using different CellMask™ Deep Red concentrations. (B) Particle concentrations of unstained and stained magnetosome solutions. Error bars represent the standard deviation of triplicates.

5.4. Conclusions

Studying the effect of different cell disruption treatments on magnetosome chain length is the key to unlock the potential of magnetosomes to become the next generation of functional materials. In this study, we systematically compared three optimized disruption techniques for MSR-1 and studied their effects on isolated magnetosome chain length, integrity and aggregation behaviour. The results from this study will directly contribute to develop better magnetosome production systems for future applications. Experimental results revealed that EZ treatment caused the highest magnetosome chain breakage, reducing the prevalence of long chains by 46%, whereas HPH best preserved chain integrity, with only a 14% reduction in long chains. Herein, we have employed nFCM for the characterization of magnetosome for the first time and whereas the tool can be used for quality assurance to determine nanoparticle concentration, we conclude that this novel technology is best suited to characterize single magnetosomes with the particular advantage of being able to reliably determine labelled magnetosomes. Hence nFCM has the potential to become a rapid analytical tool to assess the quality of single magnetosome preparations prior to application studies.

Chapter 6.

Conclusions and future work

6.1. Conclusions

The research presented in this thesis has provided significant insights into key challenges of magnetosome bioprocessing that currently hinder the development of large-scale industrial magnetosome production. **Chapters 3** and **4** concentrated on early upstream processes, aiming to elucidate the mechanisms of biomineralization and to identify physiological bottlenecks in MTB, while **Chapter 5** primarily examined the early stages of downstream processes, particularly the cell disruption step, utilizing biomass derived from scale-up fermentation experiments.

Despite addressing distinct topics, **Chapters 3** and **4** employed a similar experimental approach, with some variations in methodology. Both chapters involved altering environmental conditions (e.g. oxygen availability, iron concentration and H_2O_2 addition) and employed a combination of analytical techniques and correlative microscopy studies to assess the impact of these conditions on *Magnetospirillum gryphiswaldense* MSR-1 physiology and biomineralization. These findings provide critical insights that contribute to bioprocess development, specifically guiding fermentation experiments in more controlled environments, such as bioreactors.

The analysis of the physiological data obtained from all the tested conditions highlighted the critical role of oxygen availability in magnetosome biomineralization, as well as in other physiological parameters, such as cell growth and PHA production. Under aerobic regimes, higher biomass and PHA yields could be obtained but at the expense of reduced cell viability compared to microaerobic environments. Regarding the effects of different iron dosages in the media, the absence of iron was found to hinder cell growth, while increasing iron levels did not negatively impact cellular proliferation. MSR-1 demonstrated a higher iron tolerance under microaerobic conditions than initially presumed, maintaining stable cell viability without signs of toxicity even at elevated iron concentrations (up to 1 mM iron citrate), while in aerobic environments, cell viability declined more rapidly under high iron concentrations. Additionally, the addition of H_2O_2 affected bacterial growth, and consequently, cell viability. In H_2O_2-doped aerobic cultures, growth was completely inhibited, and cell viability was severely compromised, whereas in H_2O_2-doped microaerobic cultures, the growth was slowed but not ceased, and cell viability was less compromised than in aerobic cultures. Monitoring physiological

parameters during cell growth is crucial, as it provides insights into the metabolic state of the cells and helps identify potential stress conditions that may compromise their viability. A thorough understanding of these dynamics allows for the optimization of culture conditions, ultimately improving bioproduct yields by preventing unnecessary cellular stress.

In terms of magnetosome biomineralization, the increase of the extracellular iron concentration enhanced magnetosome production up to a saturation point at 300 µM iron citrate. Beyond this threshold, magnetosome production and the total intracellular iron content did not increase, even when additional iron was provided. This highlighted the efficiency and robustness of the iron regulation systems in MSR-1. A correlation was also elucidated between the intracellular labile Fe^{2+} concentration and magnetosome content, whereby cells with higher numbers of magnetosomes presented higher levels of labile Fe^{2+} compared to cells with fewer magnetosomes. Furthermore, even after biomineralization was completed, a substantial pool of intracellular labile Fe^{2+} remained unused, indicating the presence of distinct intracellular iron pools apart from magnetite. This observation aligned with iron uptake models suggesting that iron is first accumulated in the cytoplasm before being transported to the magnetosome vesicles. The presence of distinct intracellular iron pools, including the unused labile Fe^{2+}, further supports the idea that cytoplasmic iron accumulation plays a critical role in regulating magnetosome formation, rather than direct iron transport during membrane invagination.

This detailed single-cell analysis to study the relationship between magnetosome content and the intracellular iron pool was only possible through the use of correlative microscopy techniques, which also facilitated the exploration of relationships between ROS accumulation, intracellular labile Fe^{2+}, and magnetosome content. The results showed that cells with higher magnetosome content exhibited elevated levels of labile Fe^{2+} and lower intracellular ROS compared to cells with fewer magnetosomes, supporting the hypothesis that magnetosomes help mitigate ROS levels due to their peroxidase activity. These results stressed the crucial role of magnetosomes in reducing oxidative stress and highlighted the complex interaction between antioxidant mechanisms, iron regulation, and magnetosome biomineralization.

The oxidative stress induced by environmental changes had significant effects on magnetosome formation. Under aerobic conditions, cells exhibited increased length, with larger spacing between magnetite crystals and significantly smaller crystals compared to those grown under microaerobic conditions. The addition of H_2O_2 led to alterations in the magnetosome chain arrangement, disrupting the needle-like configuration and resulting in the formation of smaller magnetite crystals. Cells exposed to H_2O_2 under aerobic conditions experienced more substantial cellular damage, losing their

characteristic spirillum-like morphology, likely due to lipid peroxidation and a reduced magnetosome content. In contrast, increasing the extracellular iron concentration at mid-exponential growth phase did not induce any changes in cellular morphology, the arrangement of the magnetosome chain, or the size of the magnetite crystals, but the size of the PHA granules was reduced under microaerobic conditions. These observations emphasise the importance of closely monitoring physiological parameters, such as PHA granule formation, ROS levels and cell size, during bioprocessing. The presence of PHA granules can hamper magnetosome purification, while excessive ROS accumulation can compromise cell health, triggering oxidative stress modifications that may reduce product quality, and introduce variability in cell population (e.g. morphological and physiological variability), ultimately limiting magnetosome productivity. Therefore, an understanding of how cellular stress responses alter metabolic activity and behaviour is essential for maintaining bioprocess efficiency and robustness.

Preserving the integrity of the magnetosome chain is crucial for certain applications, yet it can be compromised by environmental factors, such as ROS-induced damage, as well as downstream processing steps like cell disruption. Cell lysis is inherently non-selective, targeting the cell membrane but also potentially damaging other cellular structures, including the magnetosome chain. Cell shape and size can also influence the efficiency of cell disruption methods in preserving key structures. In **Chapter 5**, three cell disruption techniques (enzymatic, sonication and high-pressure homogenization disruption) were evaluated to assess their impact on the magnetosome chain. Although all treatments showed high disruption efficiencies, EZ treatment caused the most significant cleavage of magnetosome chains, while HPH was the most effective in preserving chain length. nFCM was employed for the first time to characterize magnetosomes. The results revealed that this technique is more suitable for determining the concentration of magnetosome preparations and for characterizing single magnetosomes rather than long chains. Moreover, nFCM offers the unique advantage of accurately detecting fluorescent-labelled magnetosomes, positioning this technology as a promising rapid analytical tool for evaluating the quality of magnetosome preparations prior to their use in application studies.

While many aspects of magnetosome biomineralization still remain unknown, significant research efforts have been directed toward understanding this complex and unique process. In this thesis, contributions were made to the study of magnetosome biomineralization, with a focus on less-explored parameters, such as the impact of ROS on cell physiology and the effects of various cell disruption methods on the integrity of the magnetosome chain. These areas had been relatively underexplored, highlighting the importance of our findings in broadening the understanding of magnetosome production and standardization.

Overall, this thesis employed a diverse range of techniques, illustrating the value of an integrated multi-scale research approach. The complementary use of different techniques enabled the strengths of one method to compensate the limitations of another, allowing for a synergistic and more comprehensive examination of the research questions. This multi-dimensional strategy facilitated the investigation of various aspects at different scales, from population-level analysis to single-cell characterization, and down to elemental quantification. Such an approach provides a holistic understanding of the complex processes under study, yielding a more complete and detailed perspective on the topics addressed.

6.2. Future work

Given the inherent limitations of this work, further research opportunities remain open. Potential future directions include:

- Investigating iron toxicity thresholds in MSR-1: As demonstrated in **Chapter 3**, an iron toxicity threshold for MSR-1 could not be determined. Future studies could further explore this by scaling up experiments from flask-level to larger-scale bioreactors, where critical parameters such as pH and dO_2 can be precisely controlled. Understanding how iron toxicity affects at different scales could provide insights into optimizing growth conditions and magnetosome production.

- Applying the integrated methodology from **Chapter 3** to other phenomena in MTB: The correlative microscopy approach combining cryoSIM and cryoSXT could be extended to explore additional phenomena in MTB. Taking advantage of using different energies within the soft X-rays spectrum, other elements besides iron can be tracked. Additionally, this method would not only aid in characterizing MTB but also facilitate advances in biomedical applications of magnetosomes. As X-ray penetrate deeper than electrons, they enable direct imaging of whole cells, making it easier to study tissues treated with magnetosome-loaded agents or to observe interactions between MTB and cellular systems, compared to high-resolution electron microscopy.

- Modelling iron uptake in MSR-1: Developing a mathematical model to describe iron uptake dynamics from experimental data (**Chapter 3**) could provide a deeper understanding of how these bacteria manage and utilize iron. Such insights could reveal the mechanisms underpinning efficient biomineralization and develop strategies for enhancing magnetosome yield.

- Exploring PHA synthesis in MTB: Although in **Chapter 3** and **4** PHA content was monitored, PHA synthesis has received little attention in MTB, despite its potential relevance to the organism's stress responses and its relationship with magnetosome formation. Further studies could investigate how PHA synthesis is regulated, particularly under stress conditions, and how it may affect magnetosome production.

- Improving correlative microscopy techniques: In **Chapter 4**, combining cryoEM with cryo-fluorescence microscopy yielded valuable data, but the disparity in resolution between these techniques posed challenges for effective data correlation. Future work could focus on integrating cryoEM with higher-resolution fluorescence techniques to bridge this gap and enhance data quality.

- Studying ROS accumulation at a bioreactor scale: Given the more controlled environment that bioreactors provide, it would be valuable to study ROS accumulation and the corresponding behaviour of MSR-1 at this scale. This investigation was initially planned for **Chapter 4** but was hindered by persistent contamination issues in our bioreactors. Such research could clarify how MSR-1 responds to oxidative stress under industrially relevant conditions.

- Engineering MTB strains with fluorescent recombinant proteins on magnetosomes surface: Instead of using a fluorophore to stain magnetosome membranes, as done in **Chapter 5**, developing genetically modified strains of MTB that express fluorescent proteins on the magnetosome surface could be used as reporters and enable rapid characterization using nFCM. This would facilitate the identification of distinct magnetosome populations for various applications, including biomedical and environmental studies, as well as for basic research purposes.

- Metabolic characterization of MSR-1 during magnetosome formation: A detailed analysis of the metabolic pathways involved in magnetosome formation is crucial for identifying bottlenecks that limit biomass and magnetosome production. Metabolomic studies on high-density MSR-1 cultures, initially planned for this thesis, were not performed due to persistent contamination issues and time constraints. However, such studies could provide a comprehensive understanding of the regulatory mechanisms governing magnetosome synthesis.

By pursuing these future directions, researchers can build upon the findings of this thesis to further advance the understanding of magnetosome biomineralization and improve the efficiency of magnetosome production for various applications.

Finally, such an understanding of biomineralization in a simplified system, such as that of MTB, is crucial not only for enhancing magnetosome production processes, but also for offering broader insights that could have significant implications across multiple fields. By studying biomineralization in these microorganisms, we can gain a better understanding of the evolution and mechanisms of mineral formation in living organisms, including the processes underlying cell compartmentalization and mineral storage. This knowledge can guide material scientists in replicating these natural principles to design novel, biomimetic materials with unique properties. Furthermore, insights gained from MTB can help biogeologists unravel the role of these microorganisms in the biogeochemical cycling of metallic elements, particularly iron, influencing nutrient availability and environmental chemistry. Additionally, the study of magnetosome biomineralization sheds light onto magnetofossils, providing insights about the Earth's ancient magnetic fields and the role of microorganisms in shaping our planet's geological and environmental history.

List of References

[1] B. H. Kim, M. J. Hackett, J. Park, and T. Hyeon, "Synthesis, Characterization, and Application of Ultrasmall Nanoparticles," *Chem. Mater.*, vol. 26, no. 1, pp. 59–71, Jan. 2013, doi: 10.1021/CM402225Z.

[2] W. K, S. D, L. J, S. R, and W. JP, "Magnetic nanoparticles in nanomedicine: a review of recent advances," *Nanotechnology*, vol. 30, no. 50, Sep. 2019, doi: 10.1088/1361-6528/AB4241.

[3] T. Nanda, A. Rathore, and D. Sharma, "Biomineralized and chemically synthesized magnetic nanoparticles: A contrast," *Front. Mater. Sci.*, vol. 14, no. 4, pp. 387–401, 2020, doi: 10.1007/s11706-020-0531-7.

[4] D. A. Bazylinski and R. B. Frankel, "Magnetosome formation in prokaryotes," *Nature Reviews Microbiology*, vol. 2, no. 3. Nature Publishing Group, pp. 217–230, Mar. 2004, doi: 10.1038/nrmicro842.

[5] D. Faivre and D. Schüler, "Magnetotactic bacteria and magnetosomes," *Chem. Rev.*, vol. 108, no. 11, pp. 4875–4898, 2008, doi: 10.1021/cr078258w.

[6] J. He *et al.*, "Strong and oriented conjugation of nanobodies onto magnetosomes for the development of a rapid immunomagnetic assay for the environmental detection of tetrabromobisphenol-A," *Anal. Bioanal. Chem.*, vol. 410, no. 25, pp. 6633–6642, Oct. 2018, doi: 10.1007/S00216-018-1270-9/TABLES/1.

[7] M. Haripriyaa and K. Suthindhiran, "Investigation of pharmacokinetics and immunogenicity of magnetosomes," *Artif. Cells, Nanomedicine, Biotechnol.*, vol. 52, no. 1, pp. 69–83, Dec. 2024, doi: 10.1080/21691401.2023.2289367.

[8] J. B. Sun *et al.*, "High-yield growth and magnetosome formation by *Magnetospirillum gryphiswaldense* MSR-1 in an oxygen-controlled fermentor supplied solely with air," *Appl. Microbiol. Biotechnol.*, vol. 79, no. 3, pp. 389–397, 2008, doi: 10.1007/s00253-008-1453-y.

[9] Y. Zhang, X. Zhang, W. Jiang, Y. Li, and J. Li, "Semicontinuous culture of *Magnetospirillum gryphiswaldense* MSR-1 cells in an autofermentor by nutrient-balanced and isosmotic feeding strategies," *Appl. Environ. Microbiol.*, vol. 77, no. 17, pp. 5851–5856, 2011, doi: 10.1128/AEM.05962-11.

[10] C. Berny *et al.*, "A Method for Producing Highly Pure Magnetosomes in Large Quantity for Medical Applications Using *Magnetospirillum gryphiswaldense* MSR-1 Magnetotactic Bacteria Amplified in Minimal Growth Media," *Front. Bioeng. Biotechnol.*, vol. 8, no. 16, Feb. 2020, doi: 10.3389/fbioe.2020.00016.

[11] A. Fernández-Castané, H. Li, O. R. T. Thomas, and T. W. Overton, "Development of a simple intensified fermentation strategy for growth of *Magnetospirillum gryphiswaldense* MSR-1: Physiological responses to changing environmental conditions," *N. Biotechnol.*, vol. 46, no. 11, pp. 22–30, 2018, doi: 10.1016/j.nbt.2018.05.1201.

[12] C. T. Lefevre and D. A. Bazylinski, "Ecology, Diversity, and Evolution of Magnetotactic Bacteria," *Microbiol. Mol. Biol. Rev.*, vol. 77, no. 3, pp. 497–526, 2013, doi: 10.1128/mmbr.00021-13.

[13] O. Raschdorf, J. M. Plitzko, D. Schüler, and F. D. Müller, "A tailored galK counterselection system for efficient markerless gene deletion and chromosomal tagging in *Magnetospirillum gryphiswaldense*," *Appl. Environ. Microbiol.*, vol. 80, no. 14, pp. 4323–4330, 2014, doi: 10.1128/AEM.00588-14.

[14] M. V. Dziuba, F. D. Müller, M. Pósfai, and D. Schüler, “Exploring the host range for genetic transfer of magnetic organelle biosynthesis,” *Nat. Nanotechnol. 2023 191*, vol. 19, no. 1, pp. 115–123, Sep. 2023, doi: 10.1038/s41565-023-01500-5.

[15] A. Fernández-Castané *et al.*, “Nanoparticle tracking analysis as a process analytical tool for characterising magnetosome preparations,” *Food Bioprod. Process.*, vol. 127, pp. 426–434, 2021, doi: 10.1016/j.fbp.2021.03.013.

[16] A. Fernández-Castané, H. Li, M. Ebeler, M. Franzreb, T. W. Overton, and O. R. T. Thomas, “A scalable biomanufacturing platform for bacterial magnetosomes,” *Food Bioprod. Process.*, vol. 144, pp. 110–122, Mar. 2024, doi: 10.1016/j.fbp.2024.01.005.

[17] S. Abdelrazig *et al.*, “Metabolic characterisation of *Magnetospirillum gryphiswaldense* MSR-1 using LC-MS-based metabolite profiling,” *RSC Adv.*, vol. 10, no. 54, pp. 32548–32560, 2020, doi: 10.1039/d0ra05326k.

[18] A. Fernández-Castané, H. Li, O. R. T. Thomas, and T. W. Overton, “Flow cytometry as a rapid analytical tool to determine physiological responses to changing O_2 and iron concentration by *Magnetospirillum gryphiswaldense* strain MSR-1,” *Sci. Rep.*, vol. 7, no. 1, pp. 1–11, 2017, doi: 10.1038/s41598-017-13414-z.

[19] C. Hierro-Iglesias, M. Masó-Martínez, J. Dulai, K. J. Chong, P. H. Blanco-Sanchez, and A. Fernández-Castané, “Magnetotactic Bacteria-Based Biorefinery: Potential for Generating Multiple Products from a Single Fermentation,” *ACS Sustain. Chem. Eng.*, vol. 9, no. 31, pp. 10537–10546, Aug. 2021, doi: 10.1021/ACSSUSCHEMENG.1C02435.

[20] S. Bellini, “On a unique behavior of freshwater bacteria,” *Chinese J. Oceanol. Limnol.*, vol. 27, no. 1, pp. 3–5, 2009, doi: 10.1007/s00343-009-0003-5.

[21] R. Blakemore, “Magnetotactic bacteria,” *Science*, vol. 190, no. 4212. pp. 377–379, 1975.

[22] K. H. Schleifer *et al.*, “The Genus *Magnetospirillum* gen. nov. Description of *Magnetospirillum gryphiswaldense* sp. nov. and Transfer of *Aquaspirillum magnetotacticum* to *Magnetospirillum magnetotacticum* comb. nov.,” *Syst. Appl. Microbiol.*, vol. 14, no. 4, pp. 379–385, 1991, doi: 10.1016/S0723-2020(11)80313-9.

[23] J. Li, Y. Pan, G. Chen, Q. Liu, L. Tian, and W. Lin, “Magnetite magnetosome and fragmental chain formation of *Magnetospirillum magneticum* AMB-1: transmission electron microscopy and magnetic observations,” *Geophys. J. Int*, vol. 177, pp. 33–42, 2009, doi: 10.1111/j.1365-246X.2009.04043.x.

[24] F. C. Meldrum, S. Mann, B. R. Heywood, R. B. Frankel, and D. A. Bazylinski, “Electron microscopy study of magnetosomes in two cultured vibrioid magnetotactic bacteria,” *Proc. R. Soc. B Biol. Sci.*, vol. 251, no. 1332, pp. 237–242, 1993, doi: 10.1098/rspb.1993.0035.

[25] D. A. Bazylinski *et al.*, “*Magnetococcus marinus* gen. nov., sp. nov., a marine, magnetotactic bacterium that represents a novel lineage (*Magnetococcaceae* fam. nov., *Magnetococcales* ord. nov.) at the base of the *Alphaproteobacteria*,” *Int. J. Syst. Evol. Microbiol.*, vol. 63, no. PART3, pp. 801–808, 2013, doi: 10.1099/ijs.0.038927-0.

[26] T. Sakaguchi, A. Arakaki, and T. Matsunaga, “*Desulfovibrio magneticus* sp. nov., a novel sulfate-reducing bacterium that produces intracellular single-domain-sized magnetite particles,” *Int. J. Syst. Evol. Microbiol.*, vol. 52, no. 1, pp. 215–221, 2002, doi: 10.1099/00207713-52-1-215.

[27] C. Jogler *et al.*, “Cultivation-independent characterization of ‘*Candidatus Magnetobacterium bavaricum*’ via ultrastructural, geochemical, ecological and metagenomic methods,” *Environ. Microbiol.*, vol. 12, no. 9, pp. 2466–2478, 2010, doi: 10.1111/j.1462-2920.2010.02220.x.

[28] C. T. Lefèvre, A. Bernadac, K. Yu-Zhang, N. Pradel, and L. F. Wu, “Isolation and characterization of a magnetotactic bacterial culture from the Mediterranean Sea,” *Environ. Microbiol.*, vol. 11, no. 7, pp. 1646–1657, 2009, doi: 10.1111/j.1462-2920.2009.01887.x.

[29] W. Lin, D. A. Bazylinski, T. Xiao, L. F. Wu, and Y. Pan, “Life with compass: Diversity and biogeography of magnetotactic bacteria,” *Environ. Microbiol.*, vol. 16, no. 9, pp. 2646–2658, 2014, doi: 10.1111/1462-2920.12313.

[30] S. L. Simmons, D. A. Bazylinski, and K. J. Edwards, “South-seeking magnetotactic bacteria in the Northern Hemisphere,” *Science (80-.).*, vol. 311, no. 5759, pp. 371–374, 2006, doi: 10.1126/science.1122843.

[31] P. Leão *et al.*, “North-seeking magnetotactic gammaproteobacteria in the Southern Hemisphere,” *Appl. Environ. Microbiol.*, vol. 82, no. 18, pp. 5595–5602, 2016, doi: 10.1128/AEM.01545-16.

[32] C. B. Flies, H. M. Jonkers, D. De Beer, K. Bosselmann, M. E. Böttcher, and D. Schüler, “Diversity and vertical distribution of magnetotactic bacteria along chemical gradients in freshwater microcosms,” *FEMS Microbiol. Ecol.*, vol. 52, no. 2, pp. 185–195, 2005, doi: 10.1016/j.femsec.2004.11.006.

[33] U. Heyen and D. Schüler, “Growth and magnetosome formation by microaerophilic *Magnetospirillum* strains in an oxygen-controlled fermentor,” *Appl. Microbiol. Biotechnol.*, vol. 61, no. 5–6, pp. 536–544, 2003, doi: 10.1007/s00253-002-1219-x.

[34] D. Schultheiss and D. Schüler, “Development of a genetic system for *Magnetospirillum gryphiswaldense*,” *Arch. Microbiol.*, vol. 179, no. 2, pp. 89–94, 2003, doi: 10.1007/s00203-002-0498-z.

[35] A. Scheffel, A. Gärdes, K. Grünberg, G. Wanner, and D. Schüler, “The major magnetosome proteins MamGFDC are not essential for magnetite biomineralization in *Magnetospirillum gryphiswaldense* but regulate the size of magnetosome crystals,” *J. Bacteriol.*, vol. 190, no. 1, pp. 377–386, 2008, doi: 10.1128/JB.01371-07.

[36] D. Muñoz *et al.*, “Magnetosomes could be protective shields against metal stress in magnetotactic bacteria,” *Sci. Rep.*, vol. 10, no. 1, pp. 1–12, 2020, doi: 10.1038/s41598-020-68183-z.

[37] F. F. Guo, W. Yang, W. Jiang, S. Geng, T. Peng, and J. L. Li, “Magnetosomes eliminate intracellular reactive oxygen species in *Magnetospirillum gryphiswaldense* MSR-1,” *Environ. Microbiol.*, vol. 14, no. 7, pp. 1722–1729, 2012, doi: 10.1111/j.1462-2920.2012.02707.x.

[38] W. Niu *et al.*, “OxyR controls magnetosome formation by regulating magnetosome island (MAI) genes, iron metabolism, and redox state,” *Free Radic. Biol. Med.*, vol. 161, no. August, pp. 272–282, 2020, doi: 10.1016/j.freeradbiomed.2020.10.015.

[39] Y. Wang, W. Lin, J. Li, and Y. Pan, “Changes of cell growth and magnetosome biomineralization in *Magnetospirillum magneticum* AMB-1 after ultraviolet-B irradiation,” *Front. Microbiol.*, vol. 4, no. 397, 2013, doi: 10.3389/fmicb.2013.00397.

[40] K. Li, P. Wang, C. Chen, C. Chen, L. Li, and T. Song, “Light irradiation helps magnetotactic bacteria eliminate intracellular reactive oxygen species,” *Environ. Microbiol.*, vol. 19, no. 9, pp. 3638–3648, 2017, doi: 10.1111/1462-2920.13864.

[41] B. Devouard, M. Pósfai, X. Hua, D. A. Bazylinski, R. B. Frankel, and P. R. Buseck, “Magnetite from magnetotactic bacteria: Size distributions and twinning,” *Am. Mineral.*, vol. 83, pp. 1387–1398, 1998.

[42] Y. A. Gorby, T. J. Beveridge, and R. P. Blakemore, “Characterization of the bacterial magnetosome membrane.,” *J. Bacteriol.*, vol. 170, no. 2, pp. 834–841, 1988, doi: 10.1128/jb.170.2.834-841.1988.

[43] O. Raschdorf, Y. Forstner, I. Kolinko, R. Uebe, J. M. Plitzko, and D. Schüler, “Genetic and Ultrastructural Analysis Reveals the Key Players and Initial Steps of Bacterial Magnetosome Membrane Biogenesis,” *PLoS Genet.*, vol. 12, no. 6, pp. 1–23, 2016, doi: 10.1371/journal.pgen.1006101.

[44] K. Grünberg, C. Wawer, B. M. Tebo, and D. Schüler, “A Large Gene Cluster Encoding Several Magnetosome Proteins Is Conserved in Different Species of Magnetotactic Bacteria,” *Appl. Environ. Microbiol.*, vol. 67, no. 10, pp. 4573–4582, 2001, doi: 10.1128/AEM.67.10.4573-4582.2001.

[45] H. Nudelman and R. Zarivach, “Structure prediction of magnetosome-associated proteins,” *Front. Microbiol.*, vol. 5, no. 9, pp. 1–17, 2014, doi: 10.3389/fmicb.2014.00009.

[46] R. Uebe and D. Schüler, “Magnetosome biogenesis in magnetotactic bacteria,” *Nat. Rev. Microbiol.*, vol. 14, no. 10, pp. 621–637, 2016, doi: 10.1038/nrmicro.2016.99.

[47] J. R. C. Bergeron *et al.*, “Structure of the magnetosome-associated actin-like MamK filament at subnanometer resolution,” *Protein Sci.*, vol. 26, no. 1, pp. 93–102, 2017, doi: 10.1002/pro.2979.

[48] M. Richter *et al.*, “Comparative genome analysis of four magnetotactic bacteria reveals a complex set of group-specific genes implicated in magnetosome biomineralization and function,” *J. Bacteriol.*, vol. 189, no. 13, pp. 4899–4910, 2007, doi: 10.1128/JB.00119-07.

[49] K. Grünberg *et al.*, “Biochemical and Proteomic Analysis of the Magnetosome Membrane in *Magnetospirillum gryphiswaldense*,” *Appl. Environ. Microbiol.*, vol. 70, no. 2, pp. 1040–1050, 2004, doi: 10.1128/AEM.70.2.1040-1050.2004.

[50] U. Dobrindt, B. Hochhut, U. Hentschel, and J. Hacker, “Genomic islands in pathogenic and environmental microorganisms,” *Nature Reviews Microbiology*, vol. 2, no. 5. Nat Rev Microbiol, pp. 414–424, May 2004, doi: 10.1038/nrmicro884.

[51] S. Schübbe *et al.*, “Characterization of a spontaneous nonmagnetic mutant of *Magnetospirillum gryphiswaldense* reveals a large deletion comprising a putative magnetosome island,” *J. Bacteriol.*, vol. 185, no. 19, pp. 5779–5790, 2003, doi: 10.1128/JB.185.19.5779-5790.2003.

[52] S. Ullrich, M. Kube, S. Schübbe, R. Reinhardt, and D. Schüler, “A hypervariable 130-kilobase genomic region of *Magnetospirillum gryphiswaldense* comprises a magnetosome island which undergoes frequent rearrangements during stationary growth,” *J. Bacteriol.*, vol. 187, no. 21, pp. 7176–7184, 2005, doi: 10.1128/JB.187.21.7176-7184.2005.

[53] C. Jogler *et al.*, “Comparative analysis of magnetosome gene clusters in magnetotactic bacteria provides further evidence for horizontal gene transfer,” *Environ. Microbiol.*, vol. 11, no. 5, pp. 1267–1277, 2009, doi: 10.1111/j.1462-2920.2009.01854.x.

[54] D. Murat, A. Quinlan, H. Vali, and A. Komeili, “Comprehensive genetic dissection of the magnetosome gene island reveals the step-wise assembly of a prokaryotic organelle,” *Proc. Natl. Acad. Sci. U. S. A.*, vol. 107, no. 12, pp. 5593–5598, 2010, doi: 10.1073/pnas.0914439107.

[55] A. Lohße *et al.*, “Functional analysis of the magnetosome Island in *Magnetospirillum gryphiswaldense*: The mamAB operon is sufficient for magnetite biomineralization,” *PLoS One*, vol. 6, no. 10, 2011, doi: 10.1371/journal.pone.0025561.

[56] A. Komeili, Z. Li, D. K. Newman, and G. J. Jensen, “Magnetosomes are cell membrane imaginations organized by the actin-like protein MamK,” *Science (80-.).*, vol. 311, no. 5758, pp. 242–245, 2006, doi: 10.1126/science.1123231.

[57] A. Lohße *et al.*, “Genetic dissection of the mamAB and mms6 operons reveals a gene set essential for magnetosome biogenesis in *Magnetospirillum gryphiswaldense*,” *J. Bacteriol.*, vol. 196, no. 14, pp. 2658–2669, 2014, doi: 10.1128/JB.01716-14.

[58] M. Tanaka, A. Arakaki, and T. Matsunaga, “Identification and functional characterization of liposome tubulation protein from magnetotactic bacteria,” *Mol. Microbiol.*, vol. 76, no. 2, pp. 480–488, 2010, doi: 10.1111/j.1365-2958.2010.07117.x.

[59] N. Zeytuni *et al.*, “Self-recognition mechanism of mamA, a magnetosome-associated TPR-containing protein, promotes complex assembly,” *Proc. Natl. Acad. Sci. U. S. A.*, vol. 108, no. 33, 2011, doi: 10.1073/pnas.1103367108.

[60] A. Quinlan, D. Murat, H. Vali, and A. Komeili, “The HtrA/DegP family protease MamE is a bifunctional protein with roles in magnetosome protein localization and magnetite biomineralization,” *Mol. Microbiol.*, vol. 80, no. 4, pp. 1075–1087, May 2011, doi: 10.1111/j.1365-2958.2011.07631.x.

[61] R. Uebe *et al.*, “The cation diffusion facilitator proteins MamB and MamM of *Magnetospirillum gryphiswaldense* have distinct and complex functions, and are involved in magnetite biomineralization and magnetosome membrane assembly,” *Mol. Microbiol.*, vol. 82, no. 4, pp. 818–835, 2011, doi: 10.1111/j.1365-2958.2011.07863.x.

[62] O. Raschdorf, F. D. Müller, M. Pósfai, J. M. Plitzko, and D. Schüler, “The magnetosome proteins MamX, MamZ and MamH are involved in redox control of magnetite biomineralization in *Magnetospirillum gryphiswaldense*,” *Mol. Microbiol.*, vol. 89, no. 5, pp. 872–886, 2013, doi: 10.1111/mmi.12317.

[63] N. Zeytuni *et al.*, “Cation diffusion facilitators transport initiation and regulation is mediated by cation induced conformational changes of the cytoplasmic domain,” *PLoS One*, vol. 9, no. 3, 2014, doi: 10.1371/journal.pone.0092141.

[64] M. I. Siponen, G. Adryanczyk, N. Ginet, P. Arnoux, Pignol, and David, “Magnetochrome: a c-type cytochrome domain specific to magnetotatic bacteria,” *Biochem. Soc. Trans.*, vol. 40, no. 6, pp. 1319–1323, Dec. 2012, doi: 10.1042/BST20120104.

[65] W. Yang *et al.*, “MamO and mamE genes are essential for magnetosome crystal biomineralization in *Magnetospirillum gryphiswaldense* MSR-1,” *Res. Microbiol.*, vol. 161, no. 8, pp. 701–705, 2010, doi: 10.1016/j.resmic.2010.07.002.

[66] A. Arakaki, A. Yamagishi, A. Fukuyo, M. Tanaka, and T. Matsunaga, “Co-ordinated functions of Mms proteins define the surface structure of cubo-octahedral magnetite crystals in magnetotactic bacteria,” *Mol. Microbiol.*, vol. 93, no. 3, pp. 554–567, 2014, doi: 10.1111/mmi.12683.

[67] D. Murat *et al.*, “The magnetosome membrane protein, MmsF, is a major regulator of magnetite biomineralization in *Magnetospirillum magneticum* AMB-1,” *Mol. Microbiol.*, vol. 85, no. 4, p. 684, Aug. 2012, doi: 10.1111/J.1365-2958.2012.08132.X.

[68] M. Tanaka, E. Mazuyama, A. Arakaki, and T. Matsunaga, “MMS6 protein regulates crystal morphology during nano-sized magnetite biomineralization in vivo,” *J. Biol. Chem.*, vol. 286, no. 8, pp. 6386–6392, Feb. 2011, doi: 10.1074/JBC.M110.183434.

[69] E. Katzmann, A. Scheffel, M. Gruska, J. M. Plitzko, and D. Schüler, “Loss of the actin-like protein

MamK has pleiotropic effects on magnetosome formation and chain assembly in *Magnetospirillum gryphiswaldense*," *Mol. Microbiol.*, vol. 77, no. 1, pp. 208–224, Jul. 2010, doi: 10.1111/j.1365-2958.2010.07202.x.

[70] A. Scheffel, M. Gruska, D. Faivre, A. Linaroudis, J. M. Plitzko, and D. Schüler, "An acidic protein aligns magnetosomes along a filamentous structure in magnetotactic bacteria," *Nature*, vol. 440, no. 7080, pp. 110–114, 2006, doi: 10.1038/nature04382.

[71] C. Jogler *et al.*, "Conservation of proteobacterial magnetosome genes and structures in an uncultivated member of the deep-branching *Nitrospira* phylum," *Proc. Natl. Acad. Sci. U. S. A.*, vol. 108, no. 3, pp. 1134–1139, 2011, doi: 10.1073/pnas.1012694108.

[72] A. Komeili, H. Vali, T. J. Beveridge, and D. K. Newman, "Magnetosome vesicles are present before magnetite formation, and MamA is required for their activation," *Proc. Natl. Acad. Sci. U. S. A.*, vol. 101, no. 11, pp. 3839–3844, 2004, doi: 10.1073/pnas.0400391101.

[73] E. Cornejo, P. Subramanian, Z. Li, G. J. Jensen, and A. Komeili, "Dynamic remodeling of the magnetosome membrane is triggered by the initiation of biomineralization," *MBio*, vol. 7, no. 1, pp. 1–9, 2016, doi: 10.1128/mBio.01898-15.

[74] T. R. Graham and M. M. Kozlov, "Interplay of proteins and lipids in generating membrane curvature," *Curr. Opin. Cell Biol.*, vol. 22, no. 4, pp. 430–436, 2010, doi: 10.1016/j.ceb.2010.05.002.

[75] S. E. Greene and A. Komeili, "Biogenesis and subcellular organization of the magnetosome organelles of magnetotactic bacteria," *Current Opinion in Cell Biology*, vol. 24, no. 4. Elsevier Current Trends, pp. 490–495, Aug. 01, 2012, doi: 10.1016/j.ceb.2012.05.008.

[76] M. M. Kozlov, F. Campelo, N. Liska, L. V. Chernomordik, S. J. Marrink, and H. T. McMahon, "Mechanisms shaping cell membranes," *Curr. Opin. Cell Biol.*, vol. 29, no. 1, pp. 53–60, 2014, doi: 10.1016/j.ceb.2014.03.006.

[77] S. Borg, J. Hofmann, A. Pollithy, C. Lang, and D. Schüler, "New vectors for chromosomal integration enable high-level constitutive or inducible magnetosome expression of fusion proteins in *Magnetospirillum gryphiswaldense*," *Appl. Environ. Microbiol.*, vol. 80, no. 8, pp. 2609–2616, 2014, doi: 10.1128/AEM.00192-14.

[78] D. Faivre and P. Zuddas, "An integrated approach for determining the origin of magnetite nanoparticles," *Earth Planet. Sci. Lett.*, vol. 243, no. 1–2, pp. 53–60, 2006, doi: 10.1016/j.epsl.2006.01.012.

[79] K. W. Mandernack, D. A. Bazylinski, W. C. Shanks, and T. D. Bullen, "Oxygen and Iron Isotope Studies of Magnetite Produced by Magnetotactic Bacteria," *Science (80-.).*, vol. 285, no. 5435, pp. 1892–1896, Sep. 1999, doi: 10.1126/SCIENCE.285.5435.1892.

[80] D. Faivre and T. U. Godec, "From bacteria to mollusks: The principles underlying the biomineralization of iron oxide materials," *Angew. Chemie - Int. Ed.*, vol. 54, no. 16, pp. 4728–4747, 2015, doi: 10.1002/anie.201408900.

[81] R. B. Frankel and D. A. Bazylinski, "How magnetotactic bacteria make magnetosomes queue up," *Trends in Microbiology*, vol. 14, no. 8. Elsevier, pp. 329–331, Aug. 01, 2006, doi: 10.1016/j.tim.2006.06.004.

[82] V. Raguraman and K. Suthindhiran, "Preparation and characterisation of magnetosomes based drug conjugates for cancer therapy," *IET Nanobiotechnology*, vol. 14, no. 9, pp. 815–822, 2020, doi: 10.1049/iet-nbt.2020.0082.

[83] J. B. Sun *et al.*, "Preparation and anti-tumor efficiency evaluation of doxorubicin-loaded bacterial magnetosomes: Magnetic nanoparticles as drug carriers isolated from *Magnetospirillum gryphiswaldense*," *Biotechnol. Bioeng.*, vol. 101, no. 6, pp. 1313–1320, 2008, doi: 10.1002/bit.22011.

[84] Q. Deng *et al.*, "Construction of a Novel Magnetic Targeting Anti-Tumor Drug Delivery System: Cytosine Arabinoside-Loaded Bacterial Magnetosome," *Mater. (Basel, Switzerland)*, vol. 6, no. 9, pp. 3755–3763, 2013, doi: 10.3390/MA6093755.

[85] V. Raguraman, M. A. Jayasri, and K. Suthindhiran, "Magnetosome mediated oral Insulin delivery and its possible use in diabetes management," *J. Mater. Sci. Mater. Med.*, vol. 31, no. 8, 2020, doi: 10.1007/s10856-020-06417-2.

[86] X. Wang *et al.*, "An enhanced anti-tumor effect of apoptin-cecropin B on human hepatoma cells by using bacterial magnetic particle gene delivery system," *Biochem. Biophys. Res. Commun.*, vol. 496, no. 2, pp. 719–725, 2018, doi: 10.1016/j.bbrc.2018.01.108.

[87] Q. Dai *et al.*, "Bacterial magnetosomes as an efficient gene delivery platform for cancer theranostics," *Microb. Cell Factories 2017 161*, vol. 16, no. 1, pp. 1–9, Nov. 2017, doi: 10.1186/S12934-017-0830-6.

[88] O. Felfoul *et al.*, "Magneto-aerotactic bacteria deliver drug-containing nanoliposomes to tumour hypoxic regions," *Nat. Nanotechnol.*, vol. 11, no. 11, pp. 941–947, Aug. 2016, doi: 10.1038/nnano.2016.137.

[89] A. F. A, S. AP, and S. AS, "Effect of surface coating on the biocompatibility and in vivo MRI detection of iron oxide nanoparticles after intrapulmonary administration," *Nanotoxicology*, vol. 9, no. 7, pp. 825–834, Oct. 2015, doi: 10.3109/17435390.2014.980450.

[90] X. Nan, W. Lai, D. Li, J. Tian, Z. Hu, and Q. Fang, "Biocompatibility of Bacterial Magnetosomes as MRI Contrast Agent: A Long-Term In Vivo Follow-Up Study," 2021, doi: 10.3390/nano11051235.

[91] Y. Zhang *et al.*, "Smart Bacterial Magnetic Nanoparticles for Tumor-Targeting Magnetic Resonance Imaging of HER2-Positive Breast Cancers," *ACS Appl. Mater. Interfaces*, vol. 11, no. 4, pp. 3654–3665, 2019, doi: 10.1021/acsami.8b15838.

[92] M. Boucher *et al.*, "Genetically tailored magnetosomes used as MRI probe for molecular imaging of brain tumor," *Biomaterials*, vol. 121, pp. 167–178, 2017, doi: 10.1016/j.biomaterials.2016.12.013.

[93] Z. Xiang *et al.*, "Tumor detection using magnetosome nanoparticles functionalized with a newly screened EGFR/HER2 targeting peptide," *Biomaterials*, vol. 115, pp. 53–64, 2017, doi: 10.1016/j.biomaterials.2016.11.022.

[94] B. Ceyhan, P. Alhorn, C. Lang, D. Schüler, and C. M. Niemeyer, "Semisynthetic biogenic magnetosome nanoparticles for the detection of proteins and nucleic acids," *Small*, vol. 2, no. 11, pp. 1251–1255, Nov. 2006, doi: 10.1002/SMLL.200600282.

[95] R. Wacker, B. Ceyhan, P. Alhorn, D. Schueler, C. Lang, and C. M. Niemeyer, "Magneto Immuno-PCR: A novel immunoassay based on biogenic magnetosome nanoparticles," *Biochem. Biophys. Res. Commun.*, vol. 357, no. 2, pp. 391–396, Jun. 2007, doi: 10.1016/J.BBRC.2007.03.156.

[96] A. Li *et al.*, "Rapid separation and immunoassay for low levels of *Salmonella* in foods using magnetosome-antibody complex and real-time fluorescence quantitative PCR," *J. Sep. Sci.*, vol. 33, no. 21, pp. 3437–3443, Nov. 2010, doi: 10.1002/JSSC.201000441.

[97] L. Wu, B. Gao, F. Zhang, X. Sun, Y. Zhang, and Z. Li, "A novel electrochemical immunosensor based on magnetosomes for detection of *staphylococcal* enterotoxin B in milk," *Talanta*, vol. 106, pp. 360–366, Mar. 2013, doi: 10.1016/J.TALANTA.2012.12.053.

[98] J. Xu *et al.*, "Surface expression of protein A on magnetosomes and capture of pathogenic bacteria by magnetosome/antibody complexes," *Front. Microbiol.*, vol. 5, no. 136, Apr. 2014, doi: 10.3389/fmicb.2014.00136.

[99] K. Wu, D. Su, J. Liu, R. Saha, and J.-P. Wang, "Magnetic nanoparticles in nanomedicine: a review of recent advances," *Nanotechnology*, vol. 30, no. 50, p. 502003, Sep. 2019, doi: 10.1088/1361-6528/AB4241.

[100] E. Alphandéry, S. Faure, O. Seksek, F. Guyot, and I. Chebbi, "Chains of magnetosomes extracted from AMB-1 magnetotactic bacteria for application in alternative magnetic field cancer therapy," *ACS Nano*, vol. 5, no. 8, pp. 6279–6296, 2011, doi: 10.1021/nn201290k.

[101] S. Mannucci *et al.*, "Magnetosomes Extracted from *Magnetospirillum gryphiswaldense* as Theranostic Agents in an Experimental Model of Glioblastoma," *Contrast Media Mol. Imaging*, vol. 2018, pp. 1–12, Jul. 2018, doi: 10.1155/2018/2198703.

[102] R. Le Fèvre *et al.*, "Enhanced antitumor efficacy of biocompatible magnetosomes for the magnetic hyperthermia treatment of glioblastoma," *Theranostics*, vol. 7, no. 18, pp. 4618–4631, 2017, doi: 10.7150/thno.18927.

[103] E. Alphandéry *et al.*, "Development of non-pyrogenic magnetosome minerals coated with poly-l-lysine leading to full disappearance of intracranial U87-Luc glioblastoma in 100% of treated mice using magnetic hyperthermia," *Biomaterials*, vol. 141, pp. 210–222, 2017, doi: 10.1016/j.biomaterials.2017.06.026.

[104] I. Ali, C. Peng, Z. M. Khan, I. Naz, and M. Sultan, "An overview of heavy metal removal from wastewater using magnetotactic bacteria," *J. Chem. Technol. Biotechnol.*, vol. 93, no. 10, pp. 2817–2832, 2018, doi: 10.1002/jctb.5648.

[105] M. Tanaka *et al.*, "Biomagnetic recovery and bioaccumulation of selenium granules in magnetotactic bacteria," *Appl. Environ. Microbiol.*, vol. 82, no. 13, pp. 3886–3891, 2016, doi: 10.1128/AEM.00508-16.

[106] Masayoshi Tanaka, Rosemary Brown, Nicole Hondow, Atsushi Arakaki, Tadashi Matsunaga, and Sarah Staniland, "Highest levels of Cu, Mn and Co doped into nanomagnetic magnetosomes through optimized biomineralisation," *J. Mater. Chem.*, vol. 22, no. 24, pp. 11919–11921, May 2012, doi: 10.1039/C2JM31520C.

[107] S. Staniland, W. Williams, N. Telling, G. Van Der Laan, A. Harrison, and B. Ward, "Controlled cobalt doping of magnetosomes in vivo," *Nat. Nanotechnol. 2008 33*, vol. 3, no. 3, pp. 158–162, Mar. 2008, doi: 10.1038/nnano.2008.35.

[108] S. Sannigrahi and K. Suthindhiran, "Metal recovery from printed circuit boards by magnetotactic bacteria," *Hydrometallurgy*, vol. 187, no. 8, pp. 113–124, Aug. 2019, doi: 10.1016/j.hydromet.2019.05.007.

[109] R. Crichton, "The Essential Role of Iron in Biology," *Iron Metab.*, pp. 22–70, 2016, doi: 10.1002/9781118925645.ch2.

[110] P. A. Frey and G. H. Reed, "The Ubiquity of Iron," 2012.

[111] L. Rahn-lee and A. Komeili, "The magnetosome model : insights into the mechanisms of bacterial biomineralization," vol. 4, no. November, pp. 1–8, 2013, doi:

10.3389/fmicb.2013.00352.

[112] D. Faivre, L. H. Böttger, B. F. Matzanke, and D. Schüler, “Intracellular magnetite biomineralization in bacteria proceeds by a distinct pathway involving membrane-bound ferritin and an iron(II) species,” *Angew. Chemie - Int. Ed.*, vol. 46, no. 44, pp. 8495–8499, 2007, doi: 10.1002/anie.200700927.

[113] S. Barber-Zucker and R. Zarivach, “A Look into the Biochemistry of Magnetosome Biosynthesis in Magnetotactic Bacteria,” 2016, doi: 10.1021/acschembio.6b01000.

[114] R. J. Calugay, H. Miyashita, Y. Okamura, and T. Matsunaga, “Siderophore production by the magnetic bacterium *Magnetospirillum magneticum* AMB-1,” *FEMS Microbiol. Lett.*, vol. 218, no. 2, pp. 371–375, 2003, doi: 10.1016/S0378-1097(02)01188-6.

[115] B. L. Dubbels, A. A. DiSpirito, J. D. Morton, J. D. Semrau, J. N. E. Neto, and D. A. Bazylinski, “Evidence for a copper-dependent iron transport system in the marine, magnetotactic bacterium strain MV-1,” *Microbiology*, vol. 150, no. 9, pp. 2931–2945, 2004, doi: 10.1099/mic.0.27233-0.

[116] L. C. Paoletti and R. P. Blakemore, “Hydroxamate production of *Aquaspirillum magnetotacticum*,” *J. Bacteriol.*, vol. 167, no. 1, pp. 73–76, 1986, doi: 10.1128/jb.167.1.73-76.1986.

[117] C. Rong, Y. Huang, W. Zhang, W. Jiang, Y. Li, and J. Li, “Ferrous iron transport protein B gene (feoB1) plays an accessory role in magnetosome formation in *Magnetospirillum gryphiswaldense* strain MSR-1,” *Res. Microbiol.*, vol. 159, no. 7–8, pp. 530–536, 2008, doi: 10.1016/j.resmic.2008.06.005.

[118] C. Berny *et al.*, “A Method for Producing Highly Pure Magnetosomes in Large Quantity for Medical Applications Using *Magnetospirillum gryphiswaldense* MSR-1 Magnetotactic Bacteria Amplified in Minimal Growth Media,” *Front. Bioeng. Biotechnol.*, vol. 8, p. 16, Feb. 2020, doi: 10.3389/fbioe.2020.00016.

[119] M. Amor *et al.*, “Magnetotactic Bacteria Accumulate a Large Pool of Iron Distinct from Their Magnetite Crystals,” *Appl. Environ. Microbiol.*, vol. 86, no. 22, pp. 1–20, 2020, doi: 10.1128/AEM.01278-20.

[120] R. Uebe *et al.*, “Deletion of a fur-like gene affects iron homeostasis and magnetosome formation in *Magnetospirillum gryphiswaldense*,” *J. Bacteriol.*, vol. 192, no. 16, pp. 4192–4204, 2010, doi: 10.1128/JB.00319-10.

[121] R. Uebe *et al.*, “Bacterioferritin of *Magnetospirillum gryphiswaldense* is a heterotetraeicosameric complex composed of functionally distinct subunits but is not involved in magnetite biomineralization,” *MBio*, vol. 10, no. 3, pp. 1–13, 2019, doi: 10.1128/mBio.02795-18.

[122] T. Egli and M. Zinn, “The concept of multiple-nutrient-limited growth of microorganisms and its application in biotechnological processes,” *Biotechnol. Adv.*, vol. 22, no. 1–2, pp. 35–43, Dec. 2003, doi: 10.1016/J.BIOTECHADV.2003.08.006.

[123] Y. Li, E. Katzmann, S. Borg, and D. Schüler, “The periplasmic nitrate reductase nap is required for anaerobic growth and involved in redox control of magnetite biomineralization in *Magnetospirillum gryphiswaldense*,” *J. Bacteriol.*, vol. 194, no. 18, pp. 4847–4856, 2012, doi: 10.1128/JB.00903-12.

[124] M. J. Merrick and R. A. Edwards, “Nitrogen control in bacteria,” *Microbiol. Rev.*, vol. 59, no. 4, pp. 604–622, Dec. 1995, doi: 10.1128/MR.59.4.604-622.1995.

[125] D. Schuler and E. Baeuerlein, “Dynamics of iron uptake and Fe_3O_4 biomineralization during aerobic and microaerobic growth of Magnetospirillum gryphiswaldense,” *J. Bacteriol.*, vol. 180, no. 1, pp. 159–162, 1998, doi: 10.1128/jb.180.1.159-162.1998.

[126] D. Schüler and E. Baeuerlein, “Iron-limited growth and kinetics of iron uptake in *Magnetospirillum gryphiswaldense*,” *Arch. Microbiol.*, vol. 166, no. 5, pp. 301–307, 1996, doi: 10.1007/s002030050387.

[127] L. H. G. Jajan, S. N. Hosseini, M. Ghorbani, S. F. Mousavi, B. Ghareyazie, and M. Abolhassani, “Effects of Environmental Conditions on High-Yield Magnetosome Production by *Magnetospirillum gryphiswaldense* MSR-1,” *Iran. Biomed. J.*, vol. 23, no. 3, p. 209, May 2019, doi: 10.29252/.23.3.209.

[128] Q. Wang *et al.*, “Physiological characteristics of *Magnetospirillum gryphiswaldense* MSR-1 that control cell growth under high-iron and low-oxygen conditions,” *Sci. Rep.*, vol. 7, no. 1, pp. 1–11, 2017, doi: 10.1038/s41598-017-03012-4.

[129] X. Wang *et al.*, “Transcriptome analysis reveals physiological characteristics required for magnetosome formation in *Magnetospirillum gryphiswaldense* MSR-1,” *Environ. Microbiol. Rep.*, vol. 8, no. 3, pp. 371–381, 2016, doi: 10.1111/1758-2229.12395.

[130] B. Pang, H. Zheng, S. Ma, J. Tian, and Y. Wen, “Nitric oxide sensor NsrR is the key direct regulator of magnetosome formation and nitrogen metabolism in *Magnetospirillum*,” *Nucleic Acids Res.*, vol. 52, no. 6, pp. 2924–2941, 2024, doi: 10.1093/nar/gkad1230.

[131] Y. Li, M. Sabaty, S. Borg, K. T. Silva, D. Pignol, and D. Schüler, “The oxygen sensor MgFnr controls magnetite biomineralization by regulation of denitrification in *Magnetospirillum gryphiswaldense*,” *BMC Microbiol.*, vol. 14, no. 1, pp. 1–12, 2014, doi: 10.1186/1471-2180-14-153.

[132] C. Moisescu, I. I. Ardelean, and L. G. Benning, “The effect and role of environmental conditions on magnetosome synthesis,” *Front. Microbiol.*, vol. 5, no. 49, pp. 1–12, 2014, doi: 10.3389/fmicb.2014.00049.

[133] O. N. Oktyabrskii and G. V. Smirnova, “Redox potential changes in bacterial cultures under stress conditions,” *Microbiology*, vol. 81, no. 2, pp. 131–142, 2012, doi: 10.1134/S0026261712020099.

[134] A. Olszewska-Widdrat, G. Schiro, V. E. Reichel, and D. Faivre, “Reducing Conditions Favor Magnetosome Production in *Magnetospirillum magneticum* AMB-1,” *Front. Microbiol.*, vol. 10, no. 582, pp. 1–10, Mar. 2019, doi: 10.3389/fmicb.2019.00582.

[135] X. Wang *et al.*, “Novel protein Mg2046 regulates magnetosome synthesis in *Magnetospirillum gryphiswaldense* MSR-1 by modulating a proper redox status,” *Front. Microbiol.*, vol. 10, no. JUN, pp. 1–12, 2019, doi: 10.3389/fmicb.2019.01478.

[136] Y. Li, O. Raschdorf, K. T. Silva, and D. Schüler, “The terminal oxidase cbb3 functions in redox control of magnetite biomineralization in *Magnetospirillum gryphiswaldense*,” *J. Bacteriol.*, vol. 196, no. 14, pp. 2552–2562, 2014, doi: 10.1128/JB.01652-14.

[137] P. Wojtaszek, “Oxidative burst: an early plant response to pathogen infection.,” *Biochem. J.*, vol. 322, no. Pt 3, p. 681, Mar. 1997, doi: 10.1042/BJ3220681.

[138] M. S. Munna, I. Nur, T. Rahman, and R. Noor, “Influence of Exogenous Oxidative Stress on *Escherichia coli* Cell Growth, Viability and Morphology,” *Am. J. Biosci.*, vol. 1, no. 4, pp. 59–62, 2013, doi: 10.11648/j.ajbio.20130104.12.

[139] B. Halliwell and J. M. C. Gutteridge, “Oxygen toxicity, oxygen radicals, transition metals and disease,” *Biochem. J.*, vol. 219, no. 1, pp. 1–14, 1984, doi: 10.1042/bj2190001.

[140] Y. Zhang *et al.*, “The disruption of an OxyR-like protein impairs intracellular magnetite biomineralization in *Magnetospirillum gryphiswaldense* MSR-1,” *Front. Microbiol.*, vol. 8, no. FEB, p. 241628, Feb. 2017, doi: 10.3389/FMICB.2017.00208/BIBTEX.

[141] S. Bresan, A. Sznajder, W. Hauf, K. Forchhammer, D. Pfeiffer, and D. Jendrossek, “Polyhydroxyalkanoate (PHA) granules have no phospholipids,” *Sci. Rep.*, vol. 6, no. March, pp. 1–13, 2016, doi: 10.1038/srep26612.

[142] S. Obruca *et al.*, “Novel unexpected functions of PHA granules,” *Appl. Microbiol. Biotechnol.*, vol. 104, no. 11, pp. 4795–4810, 2020, doi: 10.1007/s00253-020-10568-1.

[143] L. Montano-Herrera, B. Laycock, A. Werker, and S. Pratt, “The evolution of polymer composition during PHA accumulation: The significance of reducing equivalents,” *Bioengineering*, vol. 4, no. 1, 2017, doi: 10.3390/bioengineering4010020.

[144] Q. Su, D. A. Bazylinski, and M. M. Jensen, “Effect of oxic and anoxic conditions on intracellular storage of polyhydroxyalkanoate and polyphosphate in *Magnetospirillum magneticum* strain AMB-1,” *Front. Microbiol.*, vol. 14, no. June, pp. 1–12, 2023, doi: 10.3389/fmicb.2023.1203805.

[145] J. Liu, Y. Ding, W. Jiang, J. Tian, Y. Li, and J. Li, “A mutation upstream of an ATPase gene significantly increases magnetosome production in *Magnetospirillum gryphiswaldense*,” *Appl. Microbiol. Biotechnol.*, vol. 81, no. 3, pp. 551–558, 2008, doi: 10.1007/s00253-008-1665-1.

[146] Y. Liu, G. R. Li, F. F. Guo, W. Jiang, Y. Li, and L. J. Li, “Large-scale production of magnetosomes by chemostat culture of *Magnetospirillum gryphiswaldense* at high cell density,” *Microb. Cell Fact.*, vol. 9, pp. 1–8, 2010, doi: 10.1186/1475-2859-9-99.

[147] K. T. Silva *et al.*, “Optimization of Magnetosome Production and Growth by the Magnetotactic Vibrio *Magnetovibrio blakemorei* Strain MV-1 through a Statistics-Based Experimental Design,” *Appl. Environ. Microbiol.*, vol. 79, no. 8, pp. 2823–2827, Apr. 2013, doi: 10.1128/AEM.03740-12.

[148] T. A. Gomes, C. M. Zanette, and M. R. Spier, “An overview of cell disruption methods for intracellular biomolecules recovery,” vol. 50, no. 7, pp. 635–654, Aug. 2020, doi: 10.1080/10826068.2020.1728696.

[149] T. Wu, X. Yu, A. Hu, L. Zhang, Y. Jin, and M. Abid, “Ultrasonic disruption of yeast cells: Underlying mechanism and effects of processing parameters,” *Innov. Food Sci. Emerg. Technol.*, vol. 28, pp. 59–65, 2015, doi: 10.1016/j.ifset.2015.01.005.

[150] A. Kobayashi *et al.*, “Experimental observation of magnetosome chain collapse in magnetotactic bacteria: Sedimentological, paleomagnetic, and evolutionary implications,” *Earth Planet. Sci. Lett.*, vol. 245, no. 3–4, pp. 538–550, 2006, doi: 10.1016/j.epsl.2006.03.041.

[151] E. Alphandéry and I. Chebbi, “Preparation of chains of magnetosomes , isolated from *Magnetospirillum magneticum* strain AMB-1 magnetotactic bacteria , yielding efficient treatment of tumors using magnetic hyperthermia,” vol. 434, pp. 444–452, 2012, doi: 10.1016/j.ijpharm.2012.06.015.

[152] P. R. Jaschke, I. Drake, and J. T. Beatty, “Modification of a French pressure cell to improve microbial cell disruption,” *Photosynth. Res.*, vol. 102, no. 1, pp. 95–97, Oct. 2009, doi: 10.1007/S11120-009-9493-4/FIGURES/1.

[153] L. Xiang, J. Wei, S. Jianbo, W. Guili, G. Feng, and L. Ying, “Purified and sterilized magnetosomes

from *Magnetospirillum gryphiswaldense* MSR-1 were not toxic to mouse fibroblasts in vitro," *Lett. Appl. Microbiol.*, vol. 45, no. 1, pp. 75–81, 2007, doi: 10.1111/j.1472-765X.2007.02143.x.

[154] J. Marqués-Marchán *et al.*, "Magnetic imaging of individual magnetosome chains in magnetotactic bacteria," *Biomater. Adv.*, vol. 163, p. 213969, Oct. 2024, doi: 10.1016/J.BIOADV.2024.213969.

[155] T. Yoshino, A. Shimojo, Y. Maeda, and T. Matsunaga, "Inducible expression of transmembrane proteins on bacterial magnetic particles in *Magnetospirillum magneticum* AMB-1," *Appl. Environ. Microbiol.*, vol. 76, no. 4, pp. 1152–1157, Feb. 2010, doi: 10.1128/AEM.01755-09

[156] J. Floury, J. Bellettre, J. Legrand, and A. Desrumaux, "Analysis of a new type of high pressure homogeniser. A study of the flow pattern," *Chem. Eng. Sci.*, vol. 59, no. 4, pp. 843–853, Feb. 2004, doi: 10.1016/J.CES.2003.11.017.

[157] F. Guo *et al.*, "A novel rapid and continuous procedure for large-scale purification of magnetosomes from *Magnetospirillum gryphiswaldense*," *Appl. Microbiol. Biotechnol.*, vol. 90, no. 4, pp. 1277–1283, 2011, doi: 10.1007/s00253-011-3189-3.

[158] T. Tang, L. Zhang, R. Gao, and Y. Dai, "Fluorescence imaging and targeted distribution of bacterial magnetic particles in nude mice," pp. 495–503, 2012, doi: 10.1007/s00253-012-3981-8.

[159] A. Fernández-Castané *et al.*, "Nanoparticle Tracking Analysis: A robust tool for characterizing magnetosomes preparations," *Food Bioprod. Process.*, no. Accepted, 2021.

[160] Y. Noguchi, T. Fujiwara, K. Yoshimatsu, and Y. Fukumori, "Iron reductase for magnetite synthesis in the magnetotactic bacterium *Magnetospirillum magnetotacticum*," *J. Bacteriol.*, vol. 181, no. 7, pp. 2142–2147, 1999, doi: 10.1128/jb.181.7.2142-2147.1999.

[161] T. Suzuki, Y. Okamura, A. Arakaki, H. Takeyama, and T. Matsunaga, "Cytoplasmic ATPase involved in ferrous ion uptake from magnetotactic bacterium *Magnetospirillum magneticum* AMB-1," *FEBS Lett.*, vol. 581, no. 18, pp. 3443–3448, 2007, doi: 10.1016/j.febslet.2007.06.047.

[162] N. Nakamura, K. Hashimoto, and T. Matsunaga, "Immunoassay Method for the Determination of Immunoglobulin G Using Bacterial Magnetic Particles," *Anal. Chem.*, vol. 63, no. 3, pp. 268–272, 1991, doi: 10.1021/ac00003a015.

[163] S. Rismani Yazdi *et al.*, "Magnetotaxis Enables Magnetotactic Bacteria to Navigate in Flow," 2017, doi: 10.1002/smll.201702982.

[164] C. T. Lefèvre, T. Song, J.-P. Yonnet, and L.-F. Wu, "Characterization of Bacterial Magnetotactic Behaviors by Using a Magnetospectrophotometry Assay," *Appl. Environ. Microbiol.*, vol. 75, no. 12, p. 3835, Jun. 2009, doi: 10.1128/AEM.00165-09.

[165] L. Zhao, D. Wu, L. F. Wu, and T. Song, "A simple and accurate method for quantification of magnetosomes in magnetotactic bacteria by common spectrophotometer," *J. Biochem. Biophys. Methods*, vol. 70, no. 3, pp. 377–383, Apr. 2007, doi: 10.1016/j.jbbm.2006.08.010.

[166] D. Schüler, R. Uhl, and E. Bäuerlein, "A simple light scattering method to assay magnetism in *Magnetospirillum gryphiswaldense*," *FEMS Microbiol. Lett.*, vol. 132, no. 1–2, pp. 139–145, Oct. 1995, doi: 10.1111/J.1574-6968.1995.TB07823.X.

[167] M. Amor, M. Tharaud, A. Gélabert, and A. Komeili, "Single-cell determination of iron content in magnetotactic bacteria: implications for the iron biogeochemical cycle," *Environ. Microbiol.*, vol. 22, no. 3, pp. 823–831, Mar. 2020, doi: 10.1111/1462-2920.14708.

[168] H. Lian, S. He, C. Chen, and X. Yan, "Flow Cytometric Analysis of Nanoscale Biological Particles

and Organelles," vol. 12, pp. 389–409, Jun. 2019, doi: 10.1146/ANNUREV-ANCHEM-061318-115042.

[169] E. Firlar *et al.*, "Investigation of the magnetosome biomineralization in magnetotactic bacteria using graphene liquid cell-transmission electron microscopy," *Nanoscale*, vol. 11, no. 2, pp. 698–705, 2019, doi: 10.1039/c8nr08647h.

[170] A. B. Ward, A. Sali, and I. A. Wilson, "Integrative Structural Biology," *Science (80-.).*, vol. 339, no. 6122, pp. 913–915, 2013, doi: 10.1126/science.1228565.

[171] L. Cerofolini, M. Fragai, E. Ravera, C. A. Diebolder, L. Renault, and V. Calderone, "Integrative Approaches in Structural Biology: A More Complete Picture from the Combination of Individual Techniques," *Biomol. 2019, Vol. 9, Page 370*, Aug. 2019, doi: 10.3390/BIOM9080370.

[172] D. M. van Elsland *et al.*, "Ultrastructural Imaging of *Salmonella*–Host Interactions Using Super-resolution Correlative Light-Electron Microscopy of Bioorthogonal Pathogens," *ChemBioChem*, vol. 19, no. 16, pp. 1766–1770, 2018, doi: 10.1002/cbic.201800230.

[173] X. Hao *et al.*, "From microscopy to nanoscopy via visible light," *Light Sci. Appl. 2013 210*, vol. 2, no. 10, pp. e108–e108, Oct. 2013, doi: 10.1038/lsa.2013.64.

[174] G. J. Brakenhoff, E. A. Van Spronsen, H. T. M. Van Der Voort, and N. Nanninga, "Chapter 14 Three-Dimensional Confocal Fluorescence Microscopy," *Methods Cell Biol.*, vol. 30, no. C, pp. 379–398, Jan. 1989, doi: 10.1016/S0091-679X(08)60987-5.

[175] M. G. L. Gustafsson *et al.*, "Three-Dimensional Resolution Doubling in Wide-Field Fluorescence Microscopy by Structured Illumination," *Biophys. J.*, vol. 94, no. 12, pp. 4957–4970, Jun. 2008, doi: 10.1529/BIOPHYSJ.107.120345.

[176] J. Groen, J. J. Conesa, R. Valcárcel, and E. Pereiro, "The cellular landscape by cryo soft X-ray tomography," *Biophys. Rev.*, vol. 11, no. 4, pp. 611–619, 2019, doi: 10.1007/s12551-019-00567-6.

[177] R. F. Thompson, M. Walker, C. A. Siebert, S. P. Muench, and N. A. Ranson, "An introduction to sample preparation and imaging by cryo-electron microscopy for structural biology," *Methods*, vol. 100, pp. 3–15, 2016, doi: 10.1016/j.ymeth.2016.02.017.

[178] R. Fernandez-Leiro and S. H. W. Scheres, "Unravelling biological macromolecules with cryo-electron microscopy," *Nat. 2016 5377620*, vol. 537, no. 7620, pp. 339–346, Sep. 2016, doi: 10.1038/nature19948.

[179] D. Wrapp *et al.*, "Cryo-EM structure of the 2019-nCoV spike in the prefusion conformation," *Science (80-.).*, vol. 367, no. 6483, pp. 1260–1263, Mar. 2020, doi: 10.1126/SCIENCE.ABB2507.

[180] D. Bollschweiler, M. Schaffer, C. M. Lawrence, and H. Engelhardt, "Cryo-electron microscopy of an extremely halophilic microbe: technical aspects," *Extremophiles*, vol. 21, no. 2, pp. 393–398, 2017, doi: 10.1007/s00792-016-0912-0.

[181] A. Neuhaus *et al.*, "Cryo-electron microscopy reveals two distinct type IV pili assembled by the same bacterium," *Nat. Commun. 2020 111*, vol. 11, no. 1, pp. 1–13, May 2020, doi: 10.1038/s41467-020-15650-w.

[182] A. Briegel *et al.*, "Location and architecture of the *Caulobacter crescentus* chemoreceptor array," *Mol. Microbiol.*, vol. 69, no. 1, pp. 30–41, Jul. 2008, doi: 10.1111/J.1365-2958.2008.06219.X.

[183] M. Tanaka, R. Brown, N. Hondow, A. Arakaki, T. Matsunaga, and S. Staniland, "Highest levels of Cu, Mn and Co doped into nanomagnetic magnetosomes through optimized

biomineralisation," *J. Mater. Chem.*, vol. 22, no. 24, pp. 11919–11921, May 2012, doi: 10.1039/C2JM31520C.

[184] M. N. Li J, Zhang H, Liu P and P. Y. Roberts AP, Chen H, Wang Y, "Phylogenetic and Structural Identification of a Novel Magnetotactic Deltaproteobacteria Strain, WYHR-1, from a Freshwater Lake," vol. 85, no. 14, pp. 1–11, 2019.

[185] V. Raguraman and K. Suthindhiran, "Comparative ecotoxicity assessment of magnetosomes and magnetite nanoparticles," *Int. J. Environ. Health Res.*, vol. 30, no. 1, pp. 13–25, Jan. 2020, doi: 10.1080/09603123.2019.1570489.

[186] K. Zhou, H. Pan, S. Zhang, H. Yue, T. Xiao, and L. Wu, "Occurrence and microscopic analyses of multicellular magnetotactic prokaryotes from coastal sediments in the Yellow Sea," *Chinese J. Oceanol. Limnol.*, vol. 29, no. 2, pp. 246–251, Mar. 2011, doi: 10.1007/s00343-011-0032-8.

[187] A. Körnig, M. Winklhofer, J. Baumgartner, T. P. Gonzalez, P. Fratzl, and D. Faivre, "Magnetite Crystal Orientation in Magnetosome Chains," *Adv. Funct. Mater.*, vol. 24, no. 25, pp. 3926–3932, Jul. 2014, doi: 10.1002/ADFM.201303737.

[188] A. Fischer, M. Schmitz, B. Aichmayer, P. Fratzl, and D. Faivre, "Structural purity of magnetite nanoparticles in magnetotactic bacteria," *J. R. Soc. Interface*, vol. 8, no. 60, pp. 1011–1018, Jul. 2011, doi: 10.1098/RSIF.2010.0576.

[189] D. Schultheiss, R. Handrick, D. Jendrossek, M. Hanzlik, and D. Schüler, "The presumptive magnetosome protein Mms16 is a poly(3-hydroxybutyrate) granule-bound protein (phasin) in *Magnetospirillum gryphiswaldense*," *J. Bacteriol.*, vol. 187, no. 7, pp. 2416–2425, 2005, doi: 10.1128/JB.187.7.2416-2425.2005.

[190] B. L. Cox *et al.*, "Organization and Elemental Analysis of P-, S-, and Fe-rich Inclusions in a Population of Freshwater Magnetococci," *Geomicrobiol. J.*, vol. 19, no. 4, pp. 387–406, 2002, doi: 10.1080/01490450290098504.

[191] C. T. Lefèvre, M. Bennet, S. Klumpp, and D. Faivre, "Positioning the flagellum at the center of a dividing cell to combine bacterial division with magnetic polarity," *MBio*, vol. 6, no. 2, pp. 1–7, 2015, doi: 10.1128/mBio.02286-14.

[192] S. Rehbein, S. Heim, P. Guttmann, S. Werner, and G. Schneider, "Ultrahigh-Resolution Soft-X-Ray Microscopy with Zone Plates in High Orders of Diffraction," *Phys. Rev. Lett.*, vol. 103, no. 11, p. 110801, Sep. 2009, doi: 10.1103/PhysRevLett.103.110801.

[193] M. A. Le Gros, G. McDermott, and C. A. Larabell, "X-ray tomography of whole cells," *Curr. Opin. Struct. Biol.*, vol. 15, no. 5, pp. 593–600, Oct. 2005, doi: 10.1016/J.SBI.2005.08.008.

[194] G. McDermott *et al.*, "Visualizing and quantifying cell phenotype using soft X-ray tomography," *BioEssays*, vol. 34, no. 4, pp. 320–327, Apr. 2012, doi: 10.1002/BIES.201100125.

[195] M. Uchida *et al.*, "Quantitative analysis of yeast internal architecture using soft X-ray tomography," *Yeast*, vol. 28, no. 3, pp. 227–236, Mar. 2011, doi: 10.1002/YEA.1834.

[196] E. Hummel *et al.*, "3D Ultrastructural Organization of Whole *Chlamydomonas reinhardtii* Cells Studied by Nanoscale Soft X-Ray Tomography," *PLoS One*, vol. 7, no. 12, p. e53293, Dec. 2012, doi: 10.1371/JOURNAL.PONE.0053293.

[197] A. J. Pérez-Berná *et al.*, "Structural Changes in Cells Imaged by Soft X-ray Cryo-Tomography during Hepatitis C Virus Infection," *ACS Nano*, vol. 10, no. 7, pp. 6597–6611, 2016, doi: 10.1021/acsnano.6b01374.

[198] C. Moscheni *et al.*, "3D quantitative and ultrastructural analysis of mitochondria in a model of

doxorubicin sensitive and resistant human colon carcinoma cells," *Cancers (Basel).*, vol. 11, no. 9, 2019, doi: 10.3390/cancers11091254.

[199] D. Attwood and A. Sakdinawat, "X-Rays and Extreme Ultraviolet Radiation : Principles and Applications."

[200] J. Guo and C. A. Larabell, "Soft X-ray tomography: virtual sculptures from cell cultures," *Curr. Opin. Struct. Biol.*, vol. 58, pp. 324–332, 2019, doi: 10.1016/j.sbi.2019.06.012.

[201] M. Harkiolaki, M. C. Darrow, M. C. Spink, E. Kosior, K. Dent, and E. Duke, "Cryo-soft X-ray tomography: Using soft X-rays to explore the ultrastructure of whole cells," *Emerg. Top. Life Sci.*, vol. 2, no. 1, pp. 81–92, 2018, doi: 10.1042/ETLS20170086.

[202] P. O. Bayguinov, M. R. Fisher, and J. A. J. Fitzpatrick, "Assaying three-dimensional cellular architecture using X-ray tomographic and correlated imaging approaches," *J. Biol. Chem.*, vol. 295, no. 46, pp. 15782–15793, Nov. 2020, doi: 10.1074/JBC.REV120.009633.

[203] L. Le Nagard *et al.*, "Magnetite magnetosome biomineralization in *Magnetospirillum magneticum* strain AMB-1: A time course study," *Chem. Geol.*, vol. 530, no. October, p. 119348, 2019, doi: 10.1016/j.chemgeo.2019.119348.

[204] X. Zhu *et al.*, "Measuring spectroscopy and magnetism of extracted and intracellular magnetosomes using soft X-ray ptychography," *Proc. Natl. Acad. Sci. U. S. A.*, vol. 113, no. 51, pp. E8219–E8227, 2016, doi: 10.1073/pnas.1610260114.

[205] D. M. Chevrier *et al.*, "Collective magnetotaxis of microbial holobionts is optimized by the three-dimensional organization and magnetic properties of ectosymbionts," *Proc. Natl. Acad. Sci. U. S. A.*, vol. 120, no. 10, p. e2216975120, Mar. 2023, doi: 10.1073/PNAS.2216975120/SUPPL_FILE/PNAS.2216975120.SM02.MP4.

[206] S. C. Howes, R. I. Koning, and A. J. Koster, "Correlative microscopy for structural microbiology," *Curr. Opin. Microbiol.*, vol. 43, no. Lm, pp. 132–138, 2018, doi: 10.1016/j.mib.2018.01.009.

[207] V. Magidson and A. Khodjakov, "Circumventing Photodamage in Live-Cell Microscopy," *Methods Cell Biol.*, vol. 114, pp. 545–560, Jan. 2013, doi: 10.1016/B978-0-12-407761-4.00023-3.

[208] M. W. Tuijtel, A. J. Koster, S. Jakobs, F. G. A. Faas, and T. H. Sharp, "Correlative cryo super-resolution light and electron microscopy on mammalian cells using fluorescent proteins," *Sci. Reports 2019 91*, vol. 9, no. 1, pp. 1–11, Feb. 2019, doi: 10.1038/s41598-018-37728-8.

[209] R. I. Koning, K. Celler, J. Willemse, E. Bos, G. P. van Wezel, and A. J. Koster, "Correlative cryo-fluorescence light microscopy and cryo-electron tomography of Streptomyces," 1st ed., vol. 124. Elsevier Inc., 2014.

[210] L. G. MA, M. G, U. M, K. CG, and L. CA, "High-aperture cryogenic light microscopy," *J. Microsc.*, vol. 235, no. 1, pp. 1–8, Jul. 2009, doi: 10.1111/J.1365-2818.2009.03184.X.

[211] M. G, L. G. MA, K. CG, U. M, and L. CA, "Soft X-ray tomography and cryogenic light microscopy: the cool combination in cellular imaging," *Trends Cell Biol.*, vol. 19, no. 11, pp. 587–595, Nov. 2009, doi: 10.1016/J.TCB.2009.08.005.

[212] I. Kounatidis *et al.*, "3D Correlative Cryo-Structured Illumination Fluorescence and Soft X-ray Microscopy Elucidates Reovirus Intracellular Release Pathway," *Cell*, vol. 182, no. 2, pp. 515-530.e17, 2020, doi: 10.1016/j.cell.2020.05.051.

[213] K. D. Elgass, E. A. Smith, M. A. LeGros, C. A. Larabell, and M. T. Ryan, "Analysis of ER-mitochondria contacts using correlative fluorescence microscopy and soft X-ray tomography

of mammalian cells," *J. Cell Sci.*, vol. 128, no. 15, pp. 2795–2804, 2015, doi: 10.1242/jcs.169136.

[214] E. Günther, A. Klauß, M. Toro-Nahuelpan, D. Schüler, C. Hille, and D. Faivre, "The in vivo mechanics of the magnetotactic backbone as revealed by correlative FLIM-FRET and STED microscopy," *Sci. Rep.*, vol. 9, no. 1, pp. 1–9, 2019, doi: 10.1038/s41598-019-55804-5.

[215] T. J. Woehl *et al.*, "Correlative electron and fluorescence microscopy of magnetotactic bacteria in liquid: Toward in vivo imaging," *Sci. Rep.*, vol. 4, pp. 22–29, 2014, doi: 10.1038/srep06854.

[216] J. Li *et al.*, "Identification of sulfate-reducing magnetotactic bacteria via a group-specific 16S rDNA primer and correlative fluorescence and electron microscopy: Strategy for culture-independent study," *Environ. Microbiol.*, vol. 24, no. 11, pp. 5019–5038, Nov. 2022, doi: 10.1111/1462-2920.16109.

[217] J. Li *et al.*, "Single-cell resolution of uncultured magnetotactic bacteria via fluorescence-coupled electron microscopy," *Appl. Environ. Microbiol.*, vol. 83, no. 12, pp. 1–16, 2017, doi: 10.1128/AEM.00409-17.

[218] G. Vargas, J. Cypriano, T. Correa, P. Leão, D. A. Bazylinski, and F. Abreu, "Applications of magnetotactic bacteria, magnetosomes and magnetosome crystals in biotechnology and nanotechnology: mini-review," *Molecules*, vol. 23, no. 10, Sep. 2018, doi: 10.3390/MOLECULES23102438.

[219] C. N. Riese *et al.*, "An automated oxystat fermentation regime for microoxic cultivation of *Magnetospirillum gryphiswaldense*," *Microb. Cell Fact.*, vol. 19, no. 1, pp. 1–15, 2020, doi: 10.1186/s12934-020-01469-z.

[220] C. Rong *et al.*, "FeoB2 functions in magnetosome formation and oxidative stress protection in *Magnetospirillum gryphiswaldense* strain MSR-1," *J. Bacteriol.*, vol. 194, no. 15, pp. 3972–3976, 2012, doi: 10.1128/JB.00382-12.

[221] M. Xia, J. Wei, Y. Lei, and L. Ying, "A novel ferric reductase purified from *Magnetospirillum gryphiswaldense* MSR-1," *Curr. Microbiol.*, vol. 55, no. 1, pp. 71–75, 2007, doi: 10.1007/s00284-007-0023-3.

[222] C. Zhang *et al.*, "Two bifunctional enzymes with ferric reduction ability play complementary roles during magnetosome synthesis in *Magnetospirillum gryphiswaldense* MSR-1," *J. Bacteriol.*, vol. 195, no. 4, pp. 876–885, 2013, doi: 10.1128/JB.01750-12.

[223] J. Baumgartner *et al.*, "Magnetotactic bacteria form magnetite from a phosphate-rich ferric hydroxide via nanometric ferric (oxyhydr)oxide intermediates," *Proc. Natl. Acad. Sci. U. S. A.*, vol. 110, no. 37, pp. 14883–14888, 2013, doi: 10.1073/pnas.1307119110.

[224] M. L. Fdez-Gubieda *et al.*, "Magnetite biomineralization in *Magnetospirillum gryphiswaldense*: Time-resolved magnetic and structural studies," *ACS Nano*, vol. 7, no. 4, pp. 3297–3305, 2013, doi: 10.1021/nn3059983.

[225] S. Staniland, B. Ward, A. Harrison, G. Van Der Laan, and N. Telling, "Rapid magnetosome formation shown by real-time x-ray magnetic circular dichroism," *Proc. Natl. Acad. Sci. U. S. A.*, vol. 104, no. 49, pp. 19524–19528, 2007, doi: 10.1073/pnas.0704879104.

[226] D. M. Chevrier *et al.*, "Synchrotron-Based Nano-X-Ray Absorption Near-Edge Structure Revealing Intracellular Heterogeneity of Iron Species in Magnetotactic Bacteria," *Small Sci.*, p. 2100089, Dec. 2021, doi: 10.1002/SMSC.202100089.

[227] M. Amor *et al.*, "Iron uptake and magnetite biomineralization in the magnetotactic bacterium *Magnetospirillum magneticum* strain AMB-1: An iron isotope study," *Geochim. Cosmochim.*

Acta, vol. 232, pp. 225–243, 2018, doi: 10.1016/j.gca.2018.04.020.

[228] A. Fernández-Castané and C. Clarke-Bland, "Unveiling magnetosome biomineralization in magnetotactic bacteria," *Biochem. (Lond).*, vol. 41, no. 4, pp. 58–59, 2019, doi: 10.1042/bio04104058.

[229] V. Ambriz-Aviña, J. A. Contreras-Garduño, and M. Pedraza-Reyes, "Applications of Flow Cytometry to Characterize Bacterial Physiological Responses," *Biomed Res. Int.*, vol. 2014, 2014, doi: 10.1155/2014/461941.

[230] M. Masó-Martínez *et al.*, "Evaluation of cell disruption technologies on magnetosome chain length and aggregation behaviour from *Magnetospirillum gryphiswaldense* MSR-1," *Front. Bioeng. Biotechnol.*, vol. 11, no. May, pp. 1–13, 2023, doi: 10.3389/fbioe.2023.1172457.

[231] J. P. McCaffrey, M. W. Phaneuf, and L. D. Madsen, "Surface damage formation during ion-beam thinning of samples for transmission electron microscopy," *Ultramicroscopy*, vol. 87, no. 3, pp. 97–104, 2001, doi: 10.1016/S0304-3991(00)00096-6.

[232] J. R. Kremer, D. N. Mastronarde, and J. R. McIntosh, "Computer visualization of three-dimensional image data using IMOD," *J. Struct. Biol.*, vol. 116, no. 1, pp. 71–76, 1996, doi: 10.1006/jsbi.1996.0013.

[233] P. Paul-Gilloteaux *et al.*, "eC-CLEM: flexible multidimensional registration software for correlative microscopies," *Nat. Methods 2017 142*, vol. 14, no. 2, pp. 102–103, Jan. 2017, doi: 10.1038/nmeth.4170.

[234] N. Vyas, S. Kunne, T. M. Fish, I. M. Dobbie, M. Harkiolaki, and P. Paul-Gilloteaux, "Protocol for image registration of correlative soft X-ray tomography and super-resolution structured illumination microscopy images," *STAR Protoc.*, vol. 2, no. 2, p. 100529, 2021, doi: 10.1016/j.xpro.2021.100529.

[235] A. Pennington *et al.*, "SuRVoS 2: Accelerating Annotation and Segmentation for Large Volumetric Bioimage Workflows Across Modalities and Scales," *Front. Cell Dev. Biol.*, vol. 10, p. 842342, Apr. 2022, doi: 10.3389/FCELL.2022.842342/BIBTEX.

[236] E. F. Pettersen *et al.*, "UCSF ChimeraX: Structure visualization for researchers, educators, and developers," *Protein Sci.*, vol. 30, no. 1, pp. 70–82, Jan. 2021, doi: 10.1002/PRO.3943.

[237] E. Katzmann *et al.*, "Magnetosome chains are recruited to cellular division sites and split by asymmetric septation," *Mol. Microbiol.*, vol. 82, no. 6, pp. 1316–1329, 2011, doi: 10.1111/j.1365-2958.2011.07874.x.

[238] F. Petrat, H. De Groot, and U. Rauen, "Determination of the chelatable iron pool of single intact cells by laser scanning microscopy," *Arch. Biochem. Biophys.*, vol. 376, no. 1, pp. 74–81, 2000, doi: 10.1006/abbi.2000.1711.

[239] G. Grass *et al.*, "FieF (YiiP) from *Escherichia coli* mediates decreased cellular accumulation of iron and relieves iron stress," *Arch. Microbiol.*, vol. 183, no. 1, pp. 9–18, 2005, doi: 10.1007/s00203-004-0739-4.

[240] C. K. Y. Lau, K. D. Krewulak, and H. J. Vogel, "Bacterial ferrous iron transport: the Feo system," *FEMS Microbiol. Rev.*, vol. 40, no. 2, pp. 273–298, Mar. 2016, doi: 10.1093/FEMSRE/FUV049.

[241] Q. Wang, J. X. Liu, W. J. Zhang, T. W. Zhang, J. Yang, and Y. Li, "Expression patterns of key iron and oxygen metabolism genes during magnetosome formation in *Magnetospirillum gryphiswaldense* MSR-1," *FEMS Microbiol. Lett.*, vol. 347, no. 2, pp. 163–172, 2013, doi: 10.1111/1574-6968.12234.

[242] A. Sorrentino *et al.*, "MISTRAL: A transmission soft X-ray microscopy beamline for cryo nano-tomography of biological samples and magnetic domains imaging," *J. Synchrotron Radiat.*, vol. 22, pp. 1112–1117, 2015, doi: 10.1107/S1600577515008632.

[243] S. R. Jones *et al.*, "Genetic and biochemical investigations of the role of MamP in redox control of iron biomineralization in *Magnetospirillum magneticum*," *Proc. Natl. Acad. Sci. U. S. A.*, vol. 112, no. 13, p. 3904, Mar. 2015, doi: 10.1073/PNAS.1417614112.

[244] L. Qi *et al.*, "Fur in *Magnetospirillum gryphiswaldense* influences magnetosomes formation and directly regulates the genes involved in iron and oxygen metabolism," *PLoS One*, vol. 7, no. 1, pp. 1–9, 2012, doi: 10.1371/journal.pone.0029572.

[245] J. Kacmar, R. Carlson, S. J. Balogh, and F. Srienc, "Staining and quantification of poly-3-hydroxybutyrate in *Saccharomyces cerevisiae* and *Cupriavidus necator* cell populations using automated flow cytometry," *Cytom. Part A*, vol. 69, no. 1, pp. 27–35, 2006, doi: 10.1002/cyto.a.20197.

[246] S. Karmann, S. Panke, and M. Zinn, "The bistable behaviour of *Pseudomonas putida* kt2440 during PHA depolymerization under carbon limitation," *Bioengineering*, vol. 4, no. 2, pp. 1–12, 2017, doi: 10.3390/bioengineering4020058.

[247] I. Vizcaino-Caston, C. A. Kelly, A. V. L. Fitzgerald, G. A. Leeke, M. Jenkins, and T. W. Overton, "Development of a rapid method to isolate polyhydroxyalkanoates from bacteria for screening studies," *J. Biosci. Bioeng.*, vol. 121, no. 1, pp. 101–104, 2016, doi: 10.1016/j.jbiosc.2015.04.021.

[248] F. Delvigne and P. Goffin, "Microbial heterogeneity affects bioprocess robustness: Dynamic single-cell analysis contributes to understanding of microbial populations," *Biotechnol. J.*, vol. 9, no. 1, pp. 61–72, Jan. 2014, doi: 10.1002/BIOT.201300119.

[249] A. Sen and J. A. Imlay, "How Microbes Defend Themselves From Incoming Hydrogen Peroxide," *Front. Immunol.*, vol. 12, no. April, pp. 1–19, 2021, doi: 10.3389/fimmu.2021.667343.

[250] I. Belevich, M. Joensuu, D. Kumar, H. Vihinen, and E. Jokitalo, "Microscopy Image Browser: A Platform for Segmentation and Analysis of Multidimensional Datasets," *PLOS Biol.*, vol. 14, no. 1, p. e1002340, Jan. 2016, doi: 10.1371/JOURNAL.PBIO.1002340.

[251] Y. Ma, F. Guo, Y. Zhang, X. Sun, T. Wen, and W. Jiang, "OxyR-Like Improves Cell Hydrogen Peroxide Tolerance by Participating in Monocyte Chemotaxis and Oxidative Phosphorylation Regulation in *Magnetospirillum gryphiswaldense* MSR-1," *J. Biomed. Nanotechnol.*, vol. 17, no. 12, pp. 2466–2476, 2021, doi: 10.1166/jbn.2021.3205.

[252] P. C. Maness, S. Smolinski, D. M. Blake, Z. Huang, E. J. Wolfrum, and W. A. Jacoby, "Bactericidal Activity of Photocatalytic TiO_2 Reaction: toward an Understanding of Its Killing Mechanism," *Appl. Environ. Microbiol.*, vol. 65, no. 9, p. 4094, 1999, doi: 10.1128/AEM.65.9.4094-4098.1999.

[253] Y. Hong, J. Zeng, X. Wang, K. Drlica, and X. Zhao, "Post-stress bacterial cell death mediated by reactive oxygen species," *Proc. Natl. Acad. Sci. U. S. A.*, vol. 116, no. 20, pp. 10064–10071, May 2019, doi: 10.1073/PNAS.1901730116/-/DCSUPPLEMENTAL.

[254] S. B. Farr, D. Touati, and T. Kogoma, "Effects of oxygen stress on membrane functions in *Escherichia coli*: role of HPI catalase.," *J. Bacteriol.*, vol. 170, no. 4, p. 1837, 1988, doi: 10.1128/JB.170.4.1837-1842.1988.

[255] W. Niu *et al.*, "OxyR controls magnetosome formation by regulating magnetosome island (MAI) genes, iron metabolism, and redox state," *Free Radic. Biol. Med.*, vol. 161, no. October, pp. 272–282, 2020, doi: 10.1016/j.freeradbiomed.2020.10.015.

[256] Y. Xie, Y. He, P. L. Irwin, T. Jin, and X. Shi, "Antibacterial Activity and Mechanism of Action of Zinc Oxide Nanoparticles against *Campylobacter jejuni*," *Appl. Environ. Microbiol.*, vol. 77, no. 7, p. 2325, Apr. 2011, doi: 10.1128/AEM.02149-10.

[257] S. G. Joshi *et al.*, "Nonthermal Dielectric-Barrier Discharge Plasma-Induced Inactivation Involves Oxidative DNA Damage and Membrane Lipid Peroxidation in *Escherichia coli*," *Antimicrob. Agents Chemother.*, vol. 55, no. 3, p. 1053, Mar. 2011, doi: 10.1128/AAC.01002-10.

[258] B. Citterio, A. Casaroli, L. Pierfelici, M. Battistelli, E. Falcieri, and W. Baffone, "Morphological changes and outer membrane protein patterns in *Helicobacter pylori* during conversion from bacillary to coccoid form," *New Microbiol.*, vol. 27, no. 4, pp. 353–360, Oct. 2004.

[259] K. T. Silva, F. Abreu, C. N. Keim, M. Farina, and U. Lins, "Ultrastructure and cytochemistry of lipid granules in the many-celled magnetotactic prokaryote, '*Candidatus Magnetoglobus multicellularis*,'" *Micron*, vol. 39, no. 8, pp. 1387–1392, Dec. 2008, doi: 10.1016/J.MICRON.2008.05.009.

[260] A. Malik, M. Nath, S. Mohiyuddin, and G. Packirisamy, "Multifunctional CdSNPs@ZIF-8: Potential Antibacterial Agent against GFP-Expressing *Escherichia coli* and *Staphylococcus aureus* and Efficient Photocatalyst for Degradation of Methylene Blue," *ACS Omega*, vol. 3, no. 7, pp. 8288–8308, 2018, doi: 10.1021/acsomega.8b00664.

[261] D. Manoil, "Oxidative Stress in Bacteria Measured by Flow Cytometry," *Adv. Biotechnol. Microbiol.*, vol. 8, no. 1, 2018, doi: 10.19080/aibm.2018.08.555726.

[262] P. Cornelis, Q. Wei, S. C. Andrews, and T. Vinckx, "Iron homeostasis and management of oxidative stress response in bacteria," *Metallomics*, vol. 3, no. 6, pp. 540–549, 2011, doi: 10.1039/c1mt00022e.

[263] D. Faivre, N. Menguy, M. Pósfai, and D. Schüler, "Environmental parameters affect the physical properties of fast-growing magnetosomes," *Am. Mineral.*, vol. 93, no. 2–3, pp. 463–469, 2008, doi: 10.2138/am.2008.2678.

[264] F. C. Meldrum, S. Mann, B. R. Heywood, R. B. Frankel, and D. A. Bazylinski, "Electron microscopy study of magnetosomes in a cultured coccoid magnetotactic bacterium," *Proc. R. Soc. London. Ser. B Biol. Sci.*, vol. 251, no. 1332, pp. 231–236, Mar. 1993, doi: 10.1098/RSPB.1993.0034.

[265] M. Masó-Martínez *et al.*, "An Integrated Approach to Elucidate the Interplay between Iron Uptake Dynamics and Magnetosome Formation at the Single-Cell Level in *Magnetospirillum gryphiswaldense*," *ACS Appl. Mater. Interfaces*, 2024, doi: 10.1021/acsami.4c15975.

[266] Q. Wang *et al.*, "Iron response regulator protein IrrB in *Magnetospirillum gryphiswaldense* MSR-1 helps control the iron/oxygen balance, oxidative stress tolerance, and magnetosome formation," *Appl. Environ. Microbiol.*, vol. 81, no. 23, pp. 8044–8053, 2015, doi: 10.1128/AEM.02585-15.

[267] S. Altuvia, M. Almiron, G. Huisman, R. Kolter, and G. Storz, "The dps promoter is activated by OxyR during growth and by IHF and σs in stationary phase," *Mol. Microbiol.*, vol. 13, no. 2, pp. 265–272, Jul. 1994, doi: 10.1111/J.1365-2958.1994.TB00421.X.

[268] L. Escolar, J. Pérez-Martín, and V. De Lorenzo, "Binding of the Fur (ferric uptake regulator) repressor of *Escherichia coli* to arrays of the GATAAT sequence," *J. Mol. Biol.*, vol. 283, no. 3, pp. 537–547, Oct. 1998, doi: 10.1006/JMBI.1998.2119.

[269] F. Petrat, U. Rauen, and H. De Groot, "Determination of the chelatable iron pool of isolated rat hepatocytes by digital fluorescence microscopy using the fluorescent probe, phen green SK,"

Hepatology, vol. 29, no. 4, pp. 1171–1179, 1999, doi: 10.1002/hep.510290435.

[270] J. Yang *et al.*, "A key time point for cell growth and magnetosome synthesis of *Magnetospirillum gryphiswaldense* based on real-time analysis of physiological factors," *Front. Microbiol.*, vol. 4, no. JUL, pp. 1–7, 2013, doi: 10.3389/fmicb.2013.00210.

[271] E. Alphandéry, I. Chebbi, F. Guyot, and M. Durand-Dubief, "Use of bacterial magnetosomes in the magnetic hyperthermia treatment of tumours: A review," *Int. J. Hyperth.*, vol. 29, no. 8, pp. 801–809, 2013, doi: 10.3109/02656736.2013.821527.

[272] A. V. Makela, M. A. Schott, C. S. Madsen, E. M. Greeson, and C. H. Contag, "Magnetic Particle Imaging of Magnetotactic Bacteria as Living Contrast Agents Is Improved by Altering Magnetosome Arrangement," *Nano Lett.*, vol. 22, no. 12, pp. 4630–4639, 2022, doi: 10.1021/acs.nanolett.1c05042.

[273] H. Li, "New bioprocess technologies underpinning future manufacture of magnetosome products," no. October, 2018.

[274] Y. Hamdous *et al.*, "Biocompatible coated magnetosome minerals with various organization and cellular interaction properties induce cytotoxicity towards RG - 2 and GL - 261 glioma cells in the presence of an alternating magnetic field," pp. 1–18, 2017, doi: 10.1186/s12951-017-0293-2.

[275] S. Falke and C. Betzel, "Dynamic Light Scattering (DLS)," in *Radiation in Bioanalysis*, Springer, Cham, 2019, pp. 173–193.

[276] T. P. Shentu *et al.*, "Thy-1 dependent uptake of mesenchymal stem cell-derived extracellular vesicles blocks myofibroblastic differentiation," *Sci. Reports 2017 71*, vol. 7, no. 1, pp. 1–11, Dec. 2017, doi: 10.1038/s41598-017-18288-9.

[277] B. Bortot *et al.*, "Platelet Activation in Ovarian Cancer Ascites: Assessment of GPIIb/IIIa and PF4 in Small Extracellular Vesicles by Nano-Flow Cytometry Analysis | Enhanced Reader," *Cancers (Basel).*, vol. 14, no. 4100, 2022.

[278] A. R. Kleinig and A. P. J. Middelberg, "On the mechanism of microbial cell disruption in high-pressure homogenisation," *Chem. Eng. Sci.*, vol. 53, no. 5, pp. 891–898, 1998, doi: 10.1016/S0009-2509(97)00414-4.

[279] A. Curcio *et al.*, "Transformation Cycle of Magnetosomes in Human Stem Cells: From Degradation to Biosynthesis of Magnetic Nanoparticles Anew," *ACS Nano*, vol. 14, no. 2, pp. 1406–1417, 2020, doi: 10.1021/acsnano.9b08061.

[280] M. Amor, V. Busigny, M. Durand-dubief, M. Tharaud, and G. Ona-nguema, "Chemical signature of magnetotactic bacteria," no. 22, pp. 0–4, 2014, doi: 10.1073/pnas.1414112112.

[281] K. Ujfalusi-Pozsonyi, H. Gabor, G.́ Pal, G.-T. Zsuzsanna, B. Zsolt, and N. Miklos, "The Effects of Detergents on the PolymerizationProperties of Actin," *Cytom. part A*, vol. 77A, no. 5, pp. 447–456, 2010.

[282] J. A. Reynoldst and C. Tanfordt, "Binding of Dodecyl Sulfate to Proteins at High Binding Ratios. Possible Implications for the State of Proteins in Biological Membranes*," *Proc. Natl. Acad. Sci.*, vol. 66, no. 3, pp. 1002–1003, 1970.

[283] R. Szatanek, M. Baj-Krzyworzeka, J. Zimoch, M. Lekka, M. Siedlar, and J. Baran, "The Methods of Choice for Extracellular Vesicles (EVs) Characterization," *Int. J. Mol. Sci.*, vol. 18, no. 6, Jun. 2017, doi: 10.3390/IJMS18061153.

[284] T. G. F. Souza, V. S. T. Ciminelli, and N. D. S. Mohallem, "A comparison of TEM and DLS methods

to characterize size distribution of ceramic nanoparticles," *J. Phys. Conf. Ser.*, vol. 733, p. 012039, Jul. 2016, doi: 10.1088/1742-6596/733/1/012039.

[285] H. Gojzewski, M. Makowski, A. Hashim, P. Kopcansky, Z. Tomori, and M. Timko, "Magnetosomes on surface: An imaging study approach," *Scanning*, vol. 34, no. 3, pp. 159–169, 2012, doi: 10.1002/sca.20292.

[286] S. Mannucci *et al.*, "Magnetic nanoparticles from *Magnetospirillum gryphiswaldense* increase the efficacy of thermotherapy in a model of Colon Carcinoma," *PLoS One*, vol. 9, no. 10, 2014, doi: 10.1371/journal.pone.0108959.

[287] T. Yoshino, H. Hirabe, M. Takahashi, M. Kuhara, H. Takeyama, and T. Matsunaga, "Magnetic cell separation using nano-sized bacterial magnetic particles with reconstructed magnetosome membrane," *Biotechnol. Bioeng.*, vol. 101, no. 3, pp. 470–477, 2008, doi: 10.1002/bit.21912.

[288] T. M. M. Bernaerts, L. Gheysen, I. Foubert, M. E. Hendrickx, and A. M. Van Loey, "Evaluating microalgal cell disruption upon ultra high pressure homogenization," *Algal Res.*, vol. 42, p. 101616, Sep. 2019, doi: 10.1016/J.ALGAL.2019.101616.

[289] Ö. Üstün-Aytekin, S. Arisoy, A. Ö. Aytekin, and E. Yildiz, "Statistical optimization of cell disruption techniques for releasing intracellular X-prolyl dipeptidyl aminopeptidase from *Lactococcus lactis* spp. lactis," *Ultrason. Sonochem.*, vol. 29, pp. 163–171, Mar. 2016, doi: 10.1016/J.ULTSONCH.2015.09.010.

[290] J. Tangtua, "Evaluation and comparison of microbial cells disruption methods for extraction of pyruvate decarboxylase." *International Food Research Journal*, 21. 1331-1336, 2014

[291] H. Vaghari *et al.*, "Application of magnetic nanoparticles in smart enzyme immobilization," *Biotechnol. Lett. 2015 382*, vol. 38, no. 2, pp. 223–233, Oct. 2015, doi: 10.1007/S10529-015-1977-Z.

[292] N. Aaltonen *et al.*, "MCF10CA Breast Cancer Cells Utilize Hyaluronan-Coated EV-Rich Trails for Coordinated Migration," *Front. Oncol.*, vol. 12, no. April, pp. 1–13, 2022, doi: 10.3389/fonc.2022.869417.

[293] K. Visscher, G. J. Brakenhoff, and T. D. Visser, "Fluorescence saturation in confocal microscopy," *Journal of Microscopy*, vol. 175, no. 2. pp. 162–165, 1994, doi: 10.1111/j.1365-2818.1994.tb03479.x.

[294] E. Alphandéry, D. Abi Haidar, O. Seksek, F. Guyot, and I. Chebbi, "Fluorescent magnetosomes for controlled and repetitive drug release under the application of an alternating magnetic field under conditions of limited temperature increase (<2.5 °C)," *Nanoscale*, vol. 10, no. 23, pp. 10918–10933, Jun. 2018, doi: 10.1039/C8NR02164C.

[295] Z. Oestreicher *et al.*, "Localization of Native Mms13 to the Magnetosome Chain of *Magnetospirillum magneticum* AMB-1 Using Immunogold Electron Microscopy, Immunofluorescence Microscopy and Biochemical Analysis," *Cryst. 2021, Vol. 11, Page 874*, vol. 11, no. 8, p. 874, Jul. 2021, doi: 10.3390/CRYST11080874.

[296] F. Mickoleit and D. Schüler, "Generation of Multifunctional Magnetic Nanoparticles with Amplified Catalytic Activities by Genetic Expression of Enzyme Arrays on Bacterial Magnetosomes," *Adv. Biosyst.*, vol. 2, no. 1, p. 1700109, Jan. 2018, doi: 10.1002/ADBI.201700109.

Appendices

Appendix A

Supporting information for Chapter 3

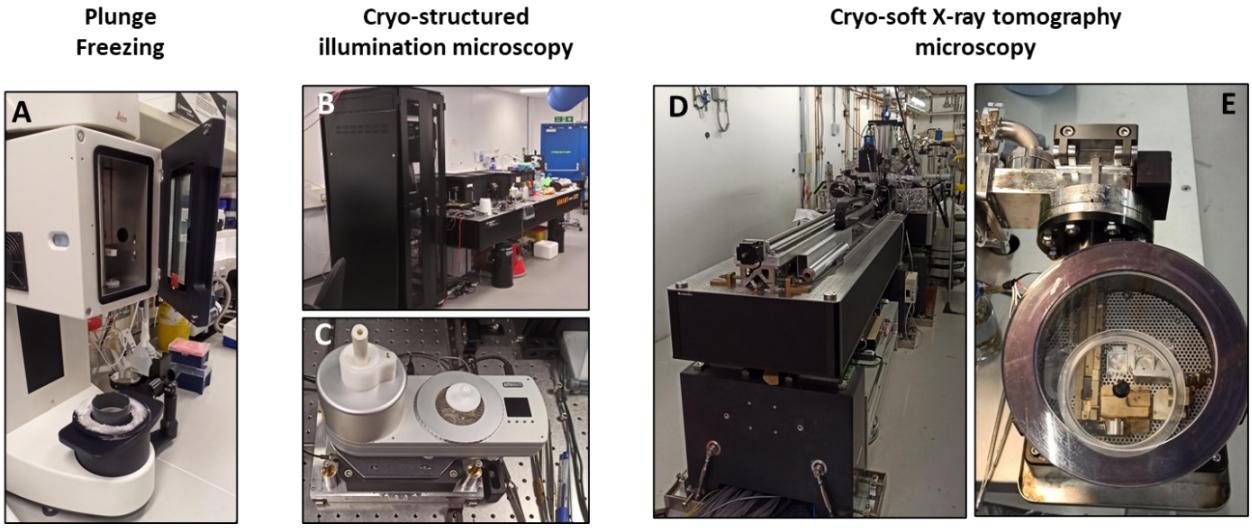

Figure A1. Correlative light and X-rays microscopy instruments of beamline B24 at Diamond Light Source UK's synchrotron. (A) Plunge Freezer; (B) Cryo-Structured Illumination Microscopy (CryoSIM); (C) Cryo-correlative stage that maintains vitrified samples under cryogenic temperatures during cryoSIM collection. (D) Soft X-ray microscope; (E) SXT sampling mounting cryo-stage.

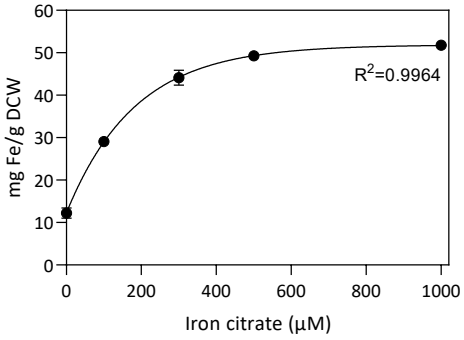

Figure A2. Total intracellular iron concentrations results of MSR-1 iron tolerance test. MSR-1 cells were grown under microaerobic conditions and different iron dosages (0-100-300-500-1000 µM iron citrate). Error bars are standard deviation (n=3).

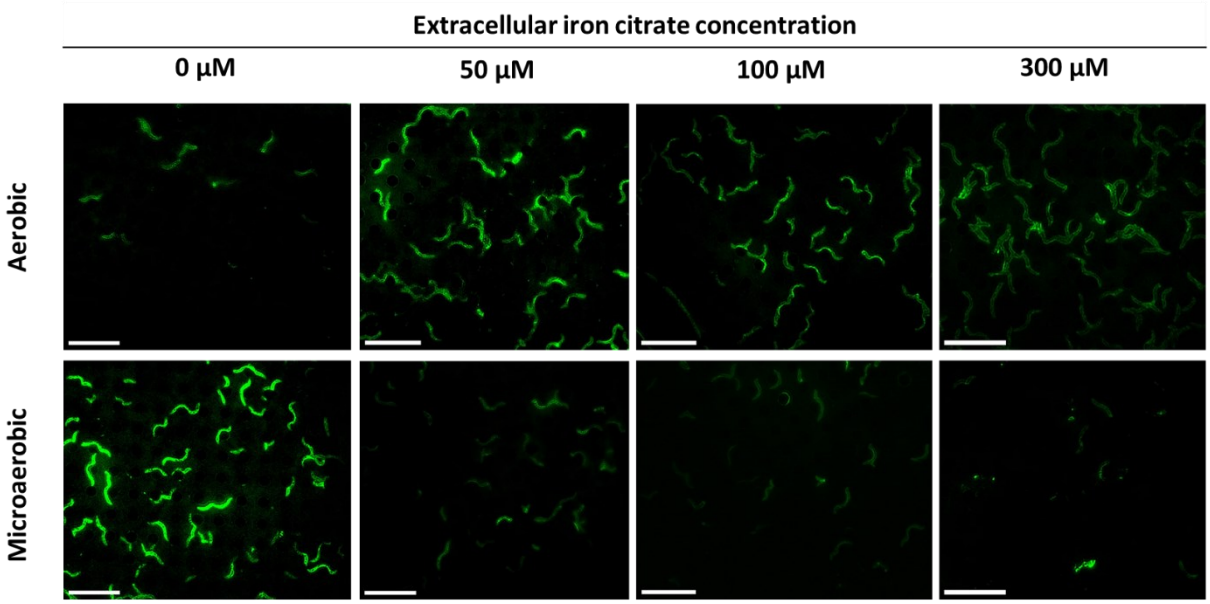

Figure A3. CryoSIM images of *Magnetospirillum gryphiswaldense* MSR-1 cells stained with PG-SK grown under different iron (0 – 50 – 100 – 300 µM iron citrate) and oxygen (aerobic or microaerobic conditions) concentrations. Scale bar = 10 µm.

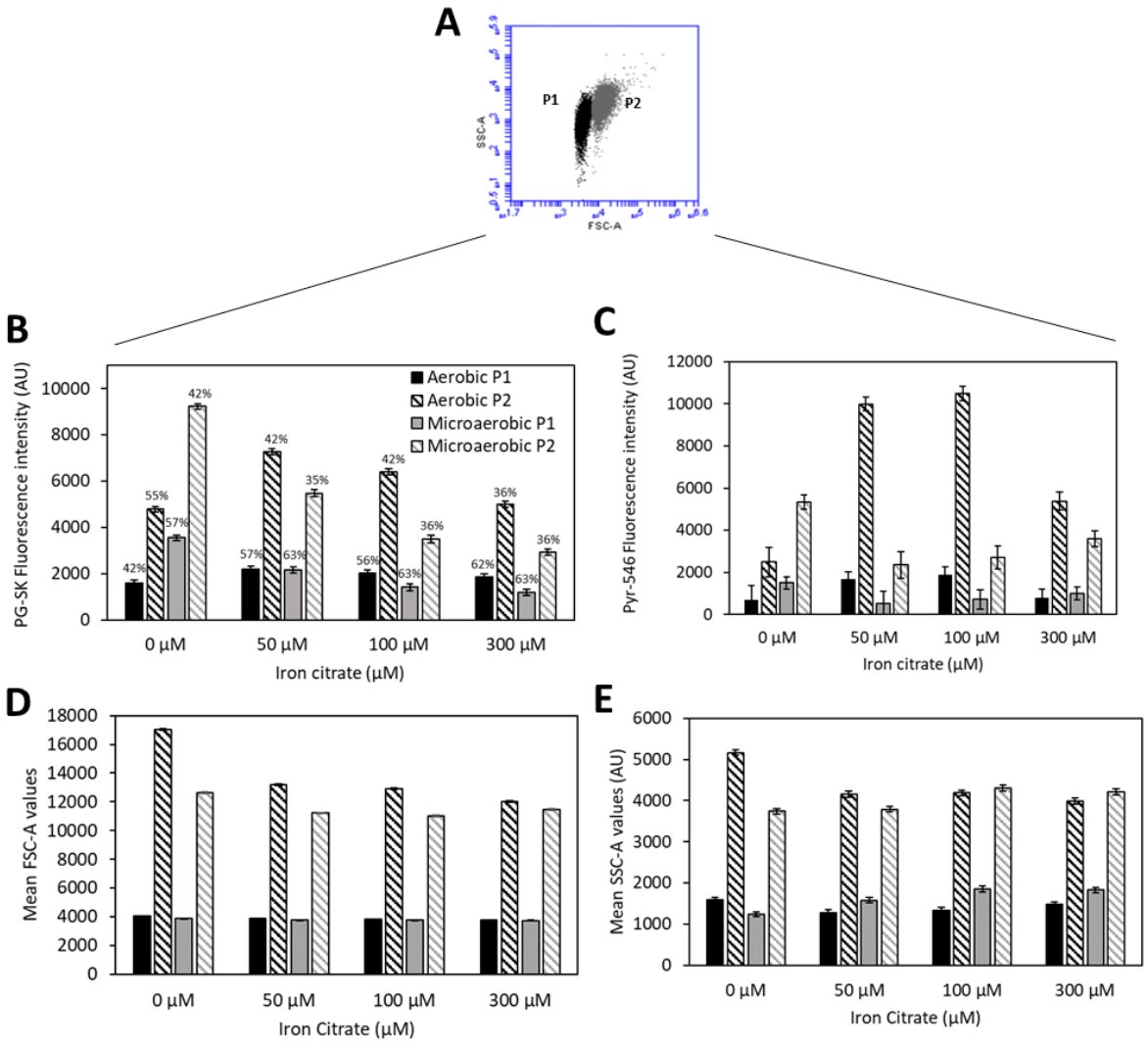

Figure A4. FCM population analysis of MSR-1 cells grown under different iron concentrations (0-50-100-300 µM iron citrate) at microaerobic or aerobic conditions. (A) Representative forward scatter (FSC-A) vs side scatter (SSC-A) dot plot in which two distinct populations (P1 and P2) can be distinguished. For all conditions these two populations could be observed. (B) PG-SK mean fluorescence intensity values. Percentage values represent the size of each population. (C) Pyr-546 mean fluorescence intensity values. (D) Mean FSC-A values. (E) Mean SSC-A values. Error bars are covariance. 25 000 events were analysed per sample by FCM. AU= arbitrary units; P1 = Population 1; P2 =Population P2.

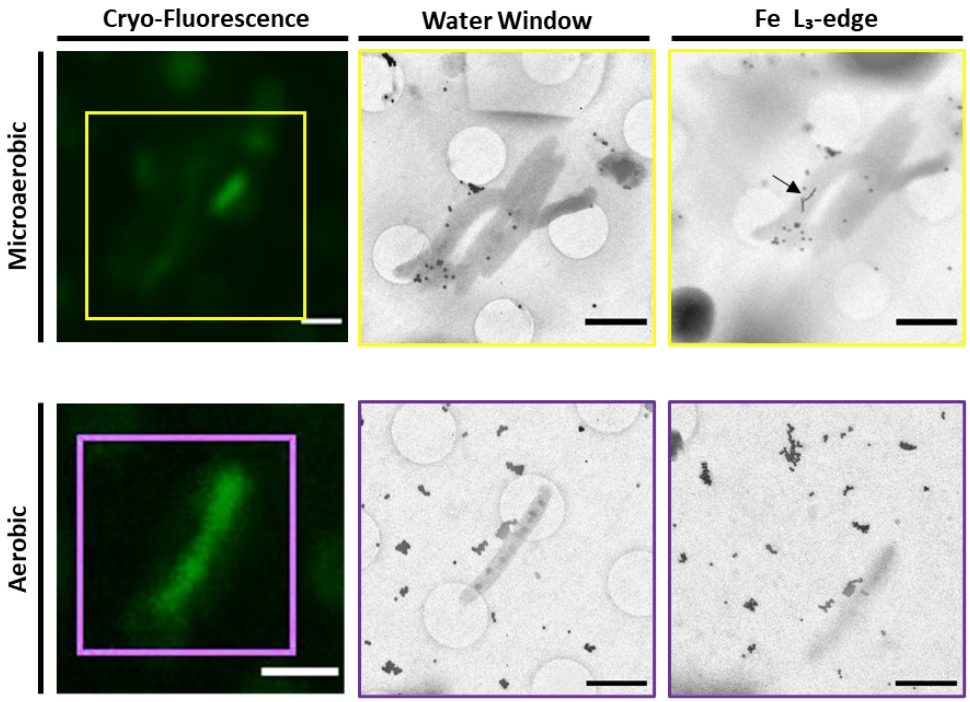

Figure A5. Correlative microscopy images taken at MISTRAL beamline at ALBA synchrotron of *Magnetospirillum gryphiswaldense* MSR-1 cells stained with PhenGreen SK grown under microaerobic and aerobic conditions. Imaging techniques: cryo-fluorescence microscopy and soft X-rays microscopy (cryoSXT). Two different photonic energies were employed for cryoSXT acquisition: 520 eV (Water Window) and 708 eV (Fe L_3-edge). Arrow indicates the presence of magnetosome chains. Scale bar = 2 µm.

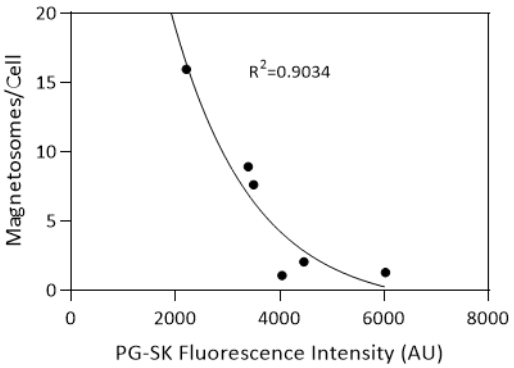

Figure A6. Correlation between mean PG-SK fluorescence values obtained by FCM and the mean number of magnetosome crystals per cell of microaerobic and aerobic MSR-1 cells grown under different iron concentrations (0-50-100-300 µM iron citrate). AU= arbitrary units.

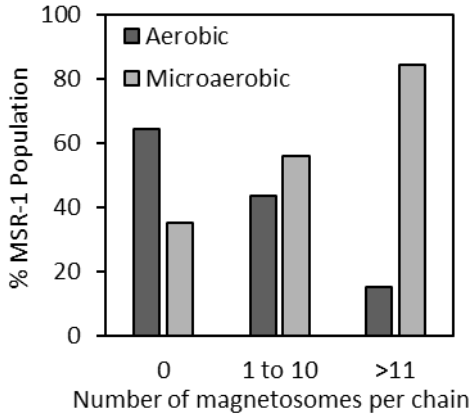

Figure A7. Classification of aerobic and microaerobic MSR-1 cells containing different magnetosome content (long, short or no chain) from Figure 3C (n=104).

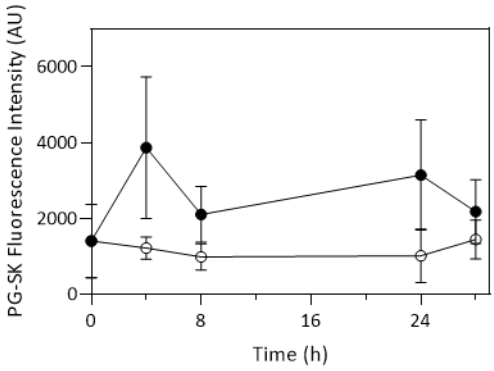

Figure A8. PG-SK mean fluorescence intensity values obtained by measuring fluorescence intensity from cryoSIM data of MSR-1 cells grown under 100 µM iron citrate under microaerobic (white) or aerobic (black) conditions over a period of 28h. AU= arbitrary units.

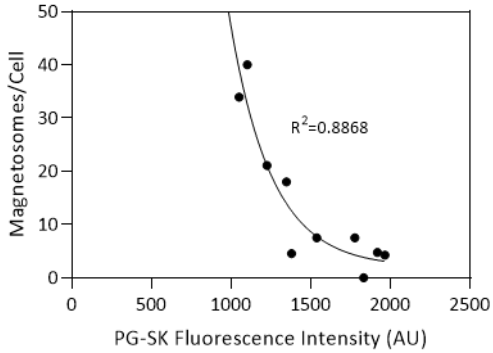

Figure A9. Correlation between mean PG-SK fluorescence values obtained by FCM and the mean number of magnetosome crystals per cell of time-course experiment in which MSR-1 cells were grown under microaerobic or aerobic conditions at a 100 µM iron citrate concentration. AU= arbitrary units.

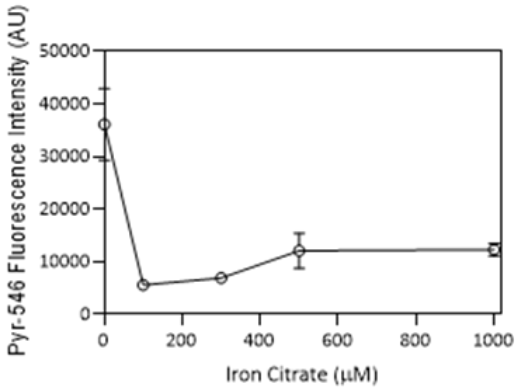

Figure A10. MSR-1 iron tolerance test analysis of PHA content. MSR-1 cells were grown under microaerobic conditions and different iron dosages (0-100-300-500-1000 µM iron citrate) and stained with Pyr-546 to be analysed by FCM. Error bars are standard deviation (n=3). AU= arbitrary units.

Supporting Movies descriptions

Movie 3.1. Example of a cryoSXT tomogram of a MSR-1 cell containing a long magnetosome chain acquired at 500 eV. Scale bar 2 µm.

Movie 3.2. CryoSXT tomogram (500 eV) correlated with 3D cryoSIM data of a MSR-1 magnetosome-producing cell. PG-SK was the iron fluorescent probe used. A 3D volumetric representation of this cell is included in which magnetosomes are coloured in pink, PHA granules in blue and the cell membrane in purple.

Movie 3.3. Example of a cryoSXT tomogram of MSR-1 cells containing a short magnetosome chains acquired at 500 eV. Scale bar 2 µm.

Movie 3.4. Example of a cryoSXT tomogram of MSR-1 cells containing a short magnetosome chains acquired at 710 eV. Scale bar 2 µm.

Appendix B

Supporting information for Chapter 4

Appendix B1: MSR-1 CellROX Deep Red Staining Optimization

Methodology:

Before any experimental procedures were conducted, the health of MSR-1 cells was verified using PI/BOX staining by flow cytometry (FCM) to ensure that only healthy cells were employed. To induce oxidative stress, MSR-1 samples were incubated with 60 µM hydrogen peroxide (H_2O_2) for 15 minutes at room temperature. Following this, the samples were incubated with varying concentrations of CellROX Deep Red (CRDR) fluorophore (0, 0.5, 1, 2, 4, 5, 8, and 10 µM). These samples were then analysed using flow cytometry at different incubation times (0, 2, 5, 10, 20, and 30 minutes). Experiments were conducted at three different temperatures: room temperature (~25°C), 30°C, and 37°C to determine the optimal fluorophore incubation temperature for MSR-1 cells.

Results:

To determine the optimal CRDR staining conditions for MSR-1, various incubation times, temperatures, and dye concentrations were tested. **Figure B1** shows the CRDR fluorescence intensity values for all the conditions tested.

Figure B1 presents the CRDR fluorescence intensity values for all conditions examined. It is evident from **Figure B1** that incubation temperature significantly influenced fluorescence intensity. The lowest fluorescence intensity values were observed at room temperature. In contrast, MSR-1 cells incubated at 30°C and 37°C exhibited higher fluorescence values, with 30°C appearing to be the optimal

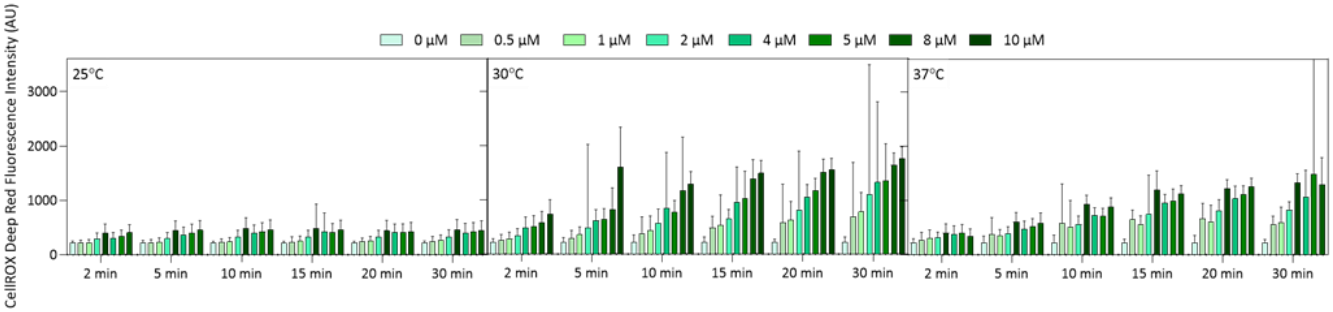

Figure B1. Magnetic MSR-1 cells incubated with CellROX Deep Red under varying dye concentrations, temperatures, and incubation times. Prior to staining, cells were exposed to 60 µM H_2O_2. Error bars are covariance.

temperature. To confirm this, further testing was conducted using aerobic cells at both temperatures (**Figure B3**).

Incubation time was also a crucial parameter, as fluorescence intensity increased with longer incubation periods. An incubation time of 30 minutes was identified as optimal, aligning with the manufacturer's recommendation.

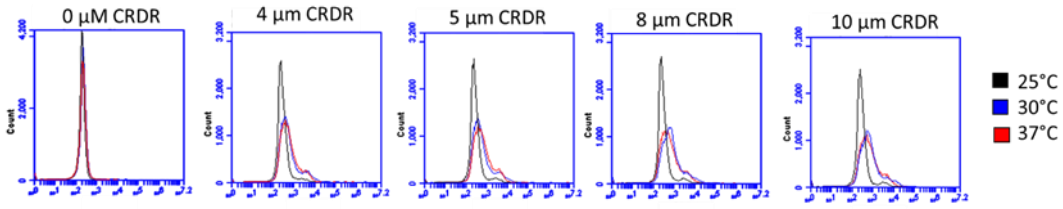

Figure B2. CellROX Deep Red (CRDR) fluorescence histogram distributions of MSR-1 cells stained with different CRDR concentrations and different incubation temperatures for 30 min.

Regarding CRDR concentrations, significant differences in fluorescence patterns were observed when comparing room temperature with higher temperatures. However, the fluorescence distributions at 30°C and 37°C were very similar (**Figure B2**), and this similarity persisted regardless of dye concentration. Based on these observations, additional tests were conducted using the more significant dye concentrations (0, 4, 5, 8, and 10 µM) at 30°C and 37°C with aerobic MSR-1 cells (Figure B3). At 30°C, no significant differences were observed between the 4 and 8 µM concentrations, with 10 µM showing the highest fluorescence intensity (Figure B3). At 37°C, no significant differences were found between the 4, 5, and 10 µM concentrations, with 8 µM resulting in the highest fluorescence intensity.

From Figure B3, it was concluded that 30°C is the optimal CRDR incubation temperature for MSR-1, as no significant differences were observed between incubating at 30°C or 37°C. Since the optimal growth temperature for MSR-1 is 30°C, using this temperature would likely cause less stress to the cells,

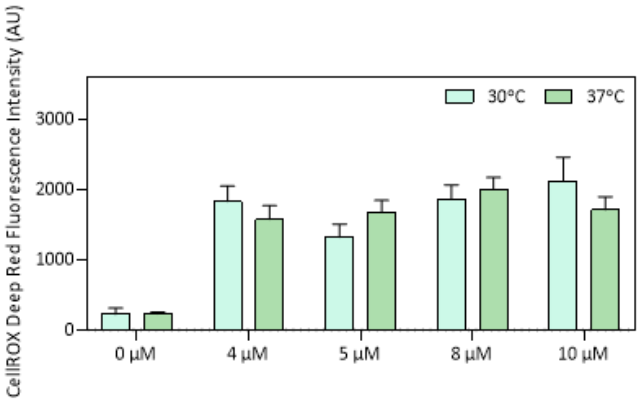

Figure B3. Comparison between CellROX Deep Red fluorescence intensities of aerobic MSR-1 cells incubated for 30 min with CRDR dye at different concentrations and incubation temperatures.

potentially leading to more accurate ROS staining levels, as incubating the cells at 37°C might impose additional stress. Regarding the optimal fluorophore concentration, the manufacturer's recommended concentration of 5 µM was chosen, as no significant differences were observed between the 4-10 µM CRDR concentrations.

In conclusion, the optimal conditions for accurate and effective staining were identified as a 30-min incubation at 30°C, with a CRDR concentration of 5 µM.

Appendix B2: Supporting Figures

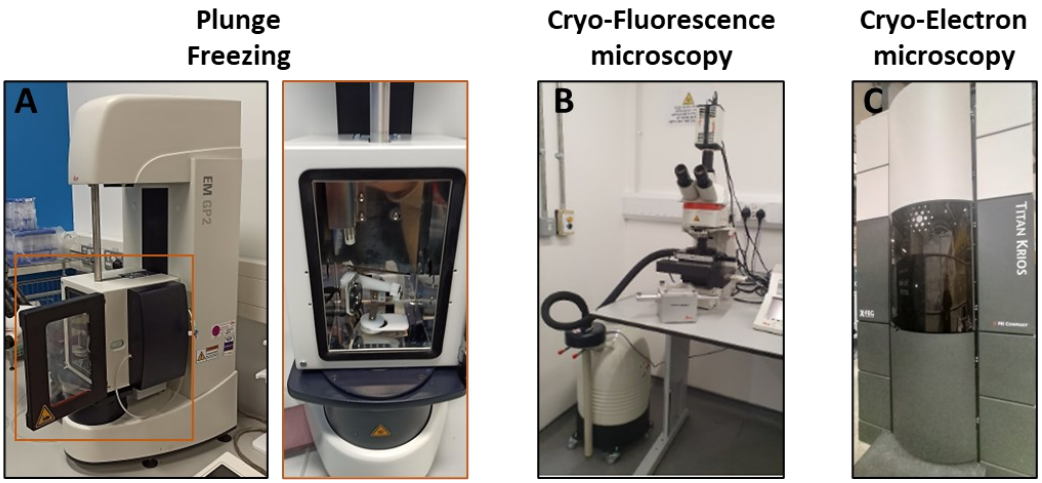

Figure B4. Correlative light and electron microscopy instruments of the Electron Bio-Imaging Centre (eBIC) located at Diamond Light Source UK's synchrotron. (A) Plunge Freezer; (B) Leica EM cryoCLEM microscope used to acquire cryo-fluorescence data; (C) Titan Krios cryo-electron microscope.

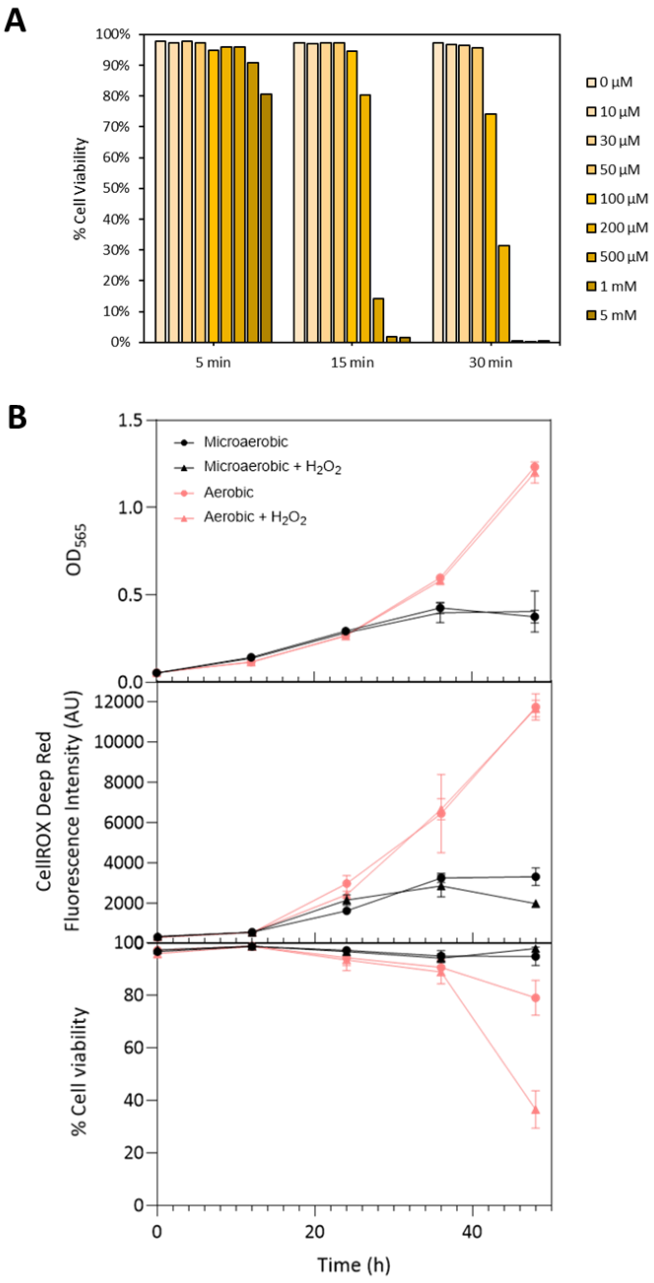

Figure B5. (A) MSR-1 H_2O_2 tolerance test results. MSR-1 cells were grown under aerobic conditions and exposed to different H_2O_2 concentrations (0-5 mM) and incubated at room temperature for 5, 15 and 30 min. (B) Effects of 60 µM H_2O_2 on cellular growth, ROS accumulation and cell viability of MSR-1 cells grown under microaerobic and aerobic conditions with or without 60 µM H_2O_2 for 48 h. Cell viability and ROS accumulation were determined using flow cytometry (FCM). 25 000 events were analysed per sample by FCM.

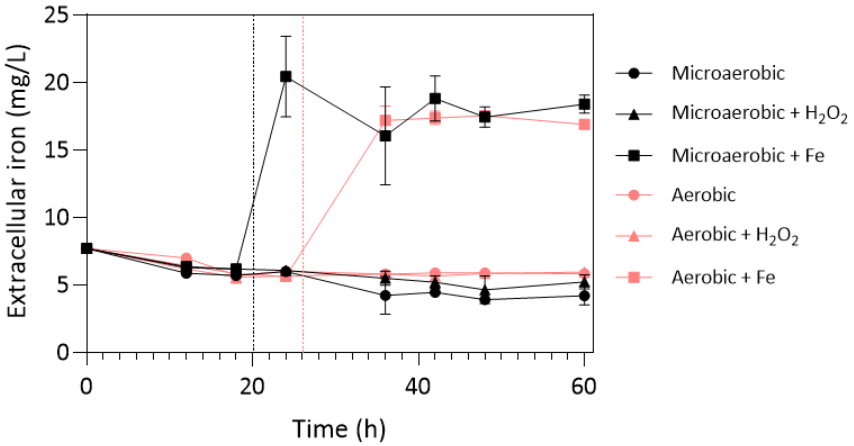

Figure B6. Extracellular iron citrate concentrations present in FSM media during a period of 60 h in which MSR-1 was grown under different stress conditions. Error bars are standard deviation (n=3).

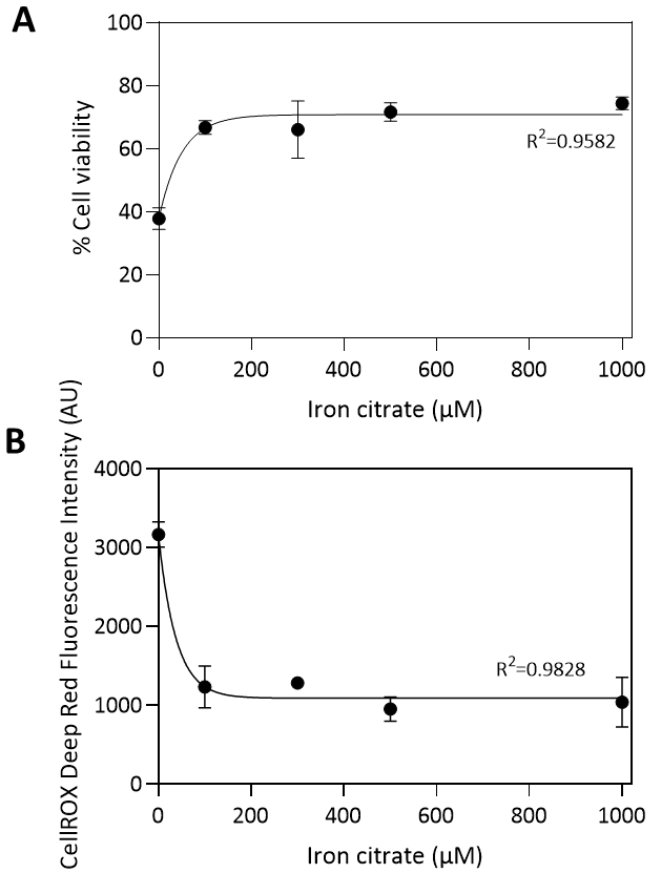

Figure B7. (A) Cell viability and (B) ROS accumulation FCM analysis of MSR-1 cells grown at various iron dosages (0-100-300-500-1000 µM iron citrate) under microaerobic conditions. Error bars are standard deviation (n=3). AU= arbitrary units.

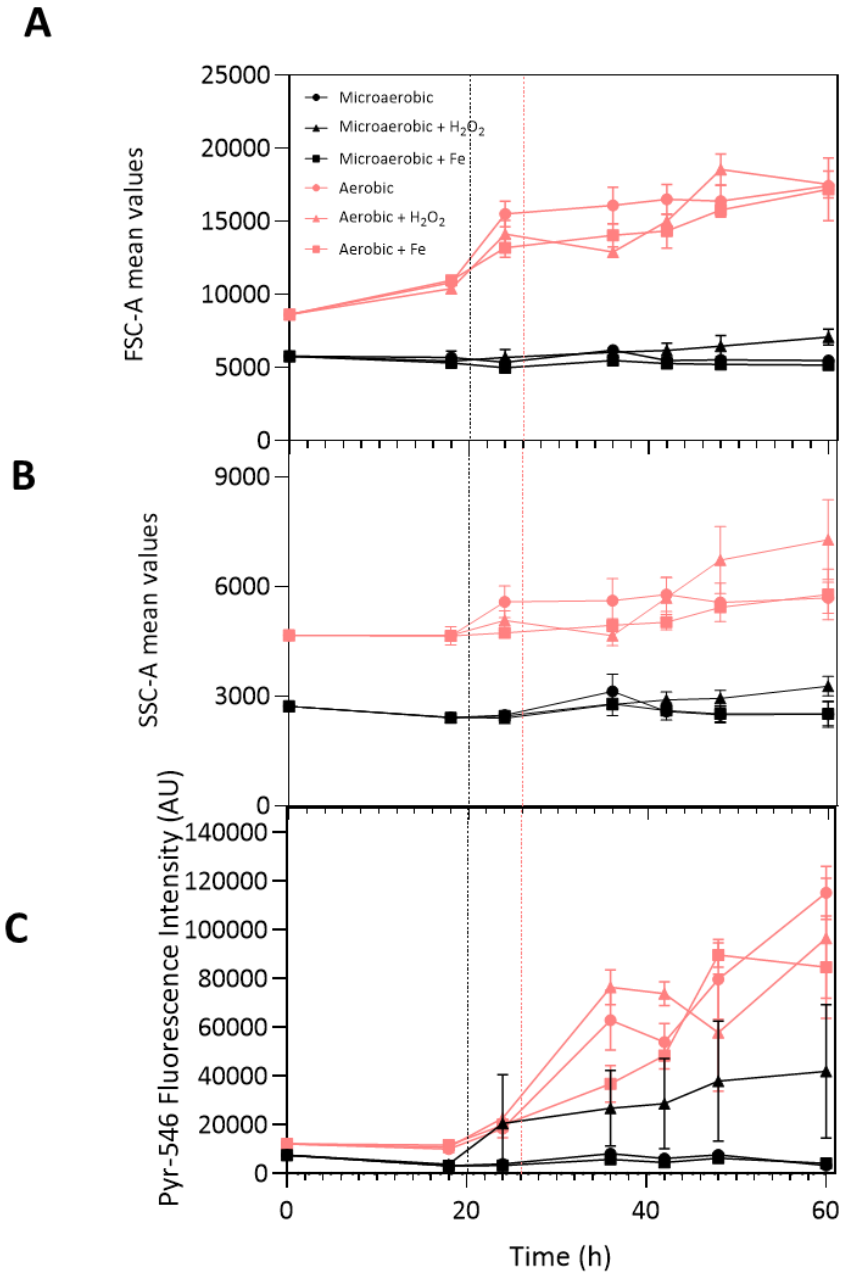

Figure B8. Flow cytometry analysis of scatter and PHA content of MSR-1 cells exposed to a sudden iron citrate or H_2O_2 pulse mid-growth. (A) Forward scatter (FSC-A), (B) side scatter (SSC-A), and (C) Pyr-546 fluorescence intensity values over time. Vertical lines in graph indicate the addition of iron and H_2O_2 pulses. AU = arbitrary units.

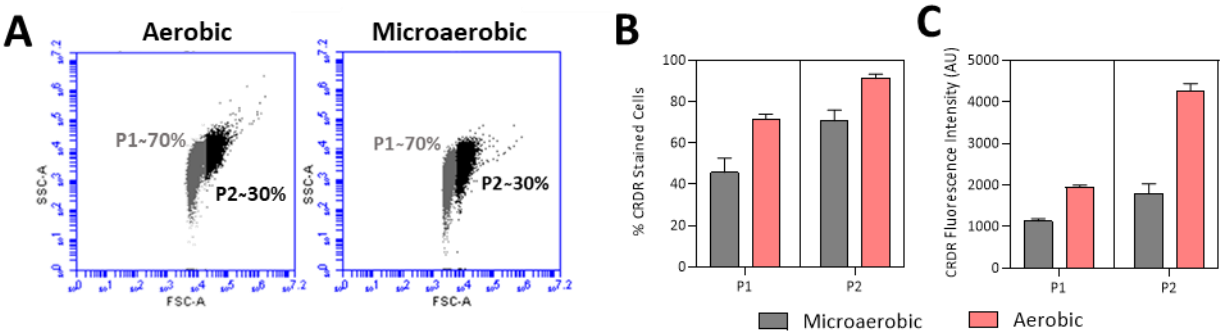

Figure B9. (A) Representative forward scatter (FSC-A) *vs* side scatter (SSC-A) dot plot of aerobic and microaerobic MSR-1 cells, in which two distinct populations (P1 and P2) can be distinguished. Comparison between aerobic and microaerobic MSR-1 cells of (B) the percentage of CRDR-stained cells and (C) the fluorescence intensity values of the CRDR-stained cells only of P1 and P2. CRDR = CellROX Deep Red; AU = arbitrary units; P1= population 1; P2 = population 2.

Supporting Movies descriptions

Movie 4.1. MSR-1 cryo-electron tomography showing the damaging effects of H_2O_2-exposition. Scale bar = 1 µm.

Movie 4.2. Representative cryo-electron tomography of MSR-1 cells grown aerobically presenting low magnetosome content. Scale bar = 1 µm.

Movie 4.3. Representative cryo-electron tomography of an MSR-1 cell grown under microaerobic conditions presenting high magnetosome content. Scale bar = 1 µm.

Movie 4.4. Representative cryo-electron tomography and its 3D volumetric segmentation of an MSR-1 cell grown under microaerobic conditions presenting high magnetosome content. Magnetosomes are coloured in blue, PHA granules in green, outer membrane in orange and inner membrane in light orange. Scale bar 1 µm.

Appendix C

Supporting information for Chapter 5

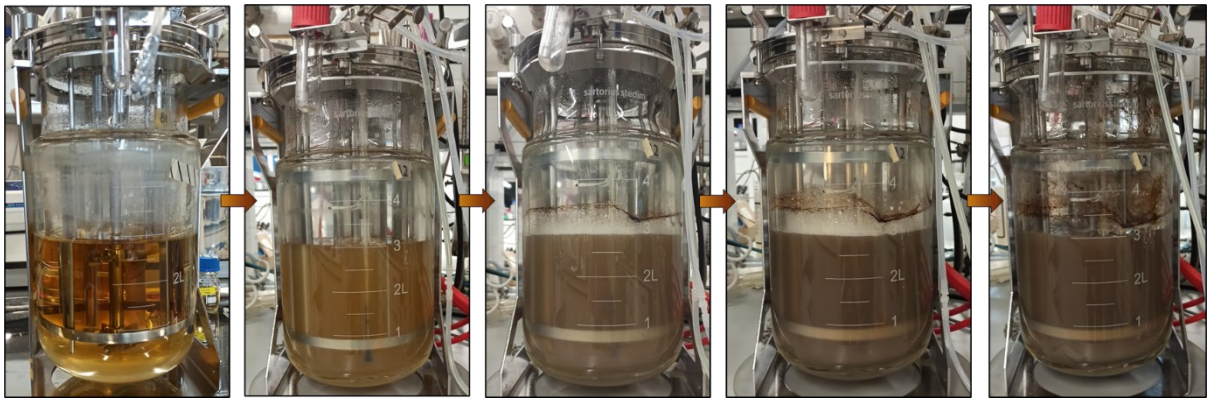

Figure C1. Evolution of broth colour of MSR-1 grown in a 5-liter bioreactor using a pH-stat growth strategy over time. The progressive darkening of the broth indicates increased magnetosome production.

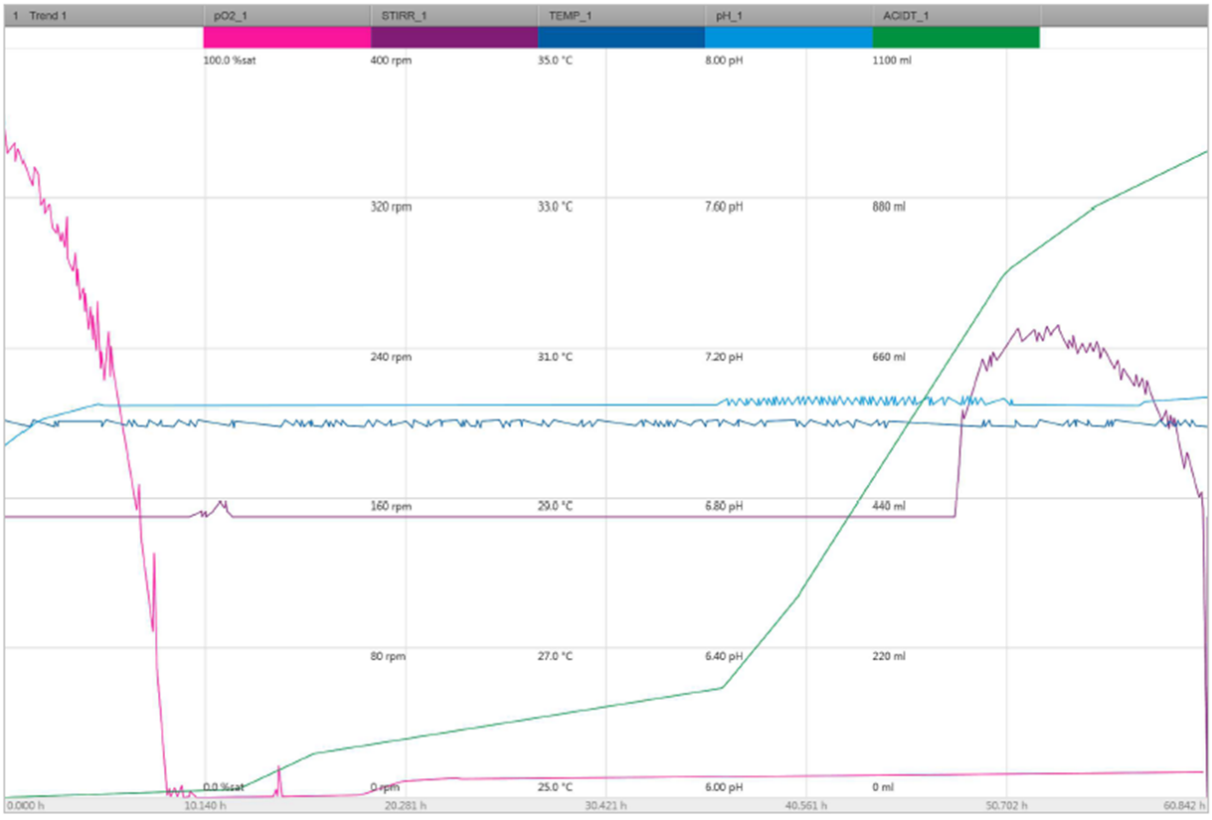

Figure C2. Evolution of the MSR-1 pH-stat fermentation parameters. pO_2 (pink); stirring (purple); temperature (dark blue); pH (light blue); feeding solution added (green).

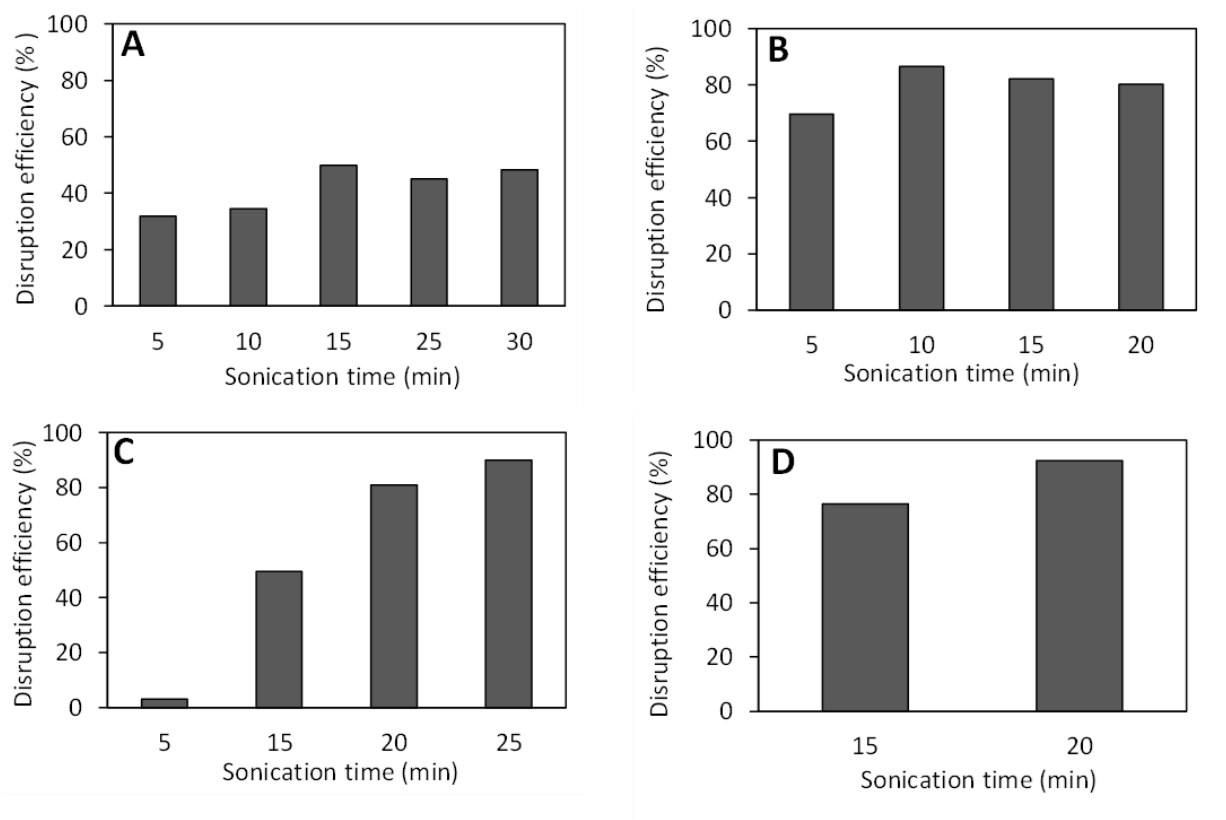

Figure C3. Optimization of MSR-1 cell disruption using probe sonication. Different biomass concentrations (10% or 20% (w/v)), sonication pulse settings (1-5 second ON/ 1-5 second OFF), working volumes (1 mL or 20 mL) and sonication times were tested. Disruption efficiency of: (A) 1 mL of 10% WCW biomass with a pulse setting of 5 second ON / 5 second OFF pulse; (B) 1 mL of 10% WCW biomass with a pulse setting of 1 second ON / 1 second OFF pulse; (C) 1 mL of 20% WCW biomass with a pulse setting of 1 second ON / 1 second OFF pulse; (D) 20 mL of 20% WCW biomass with a pulse setting of 1 second ON / 1 second OFF pulse.

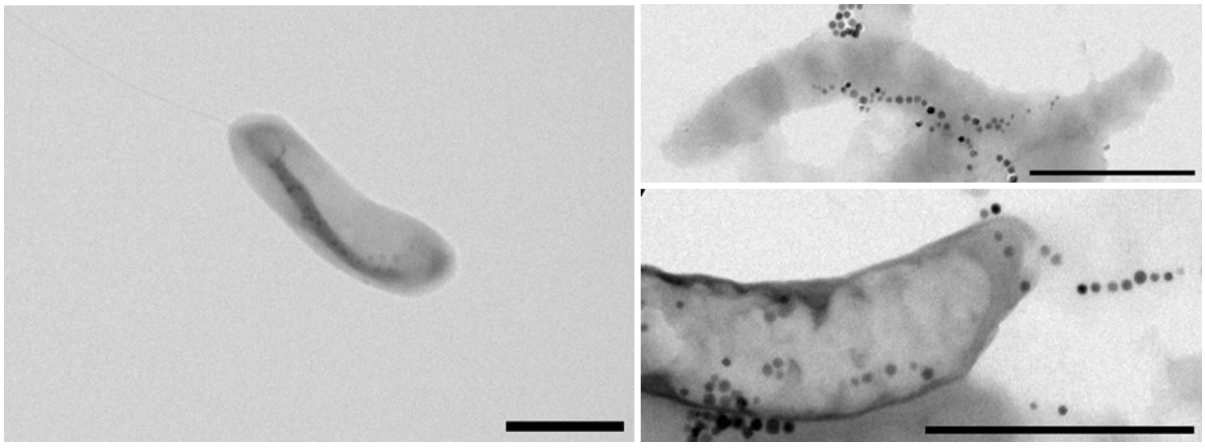

Figure C4. Transmission electron microscopy images of undisrupted *M. gryphiswaldense* MSR-1 cells after enzymatic cell disruption treatment and magnetosome purification. Scale = 1 µm.